Challenge Journal of STRUCTURAL MECHANICS

Vol.11 No.3 (2025)

auxetic buckling load building codes compressive strength dynamic analysis earthquake finite element method girder bridge Jaya algorithm metaheuristic algorithms modal analysis optimization prestresing pushover analysis reinforced concrete seismic design shallow foundations smart concrete stability static analysis steel structures structural dynamics temperature effects thick plate



EDITOR-IN-CHIEF

Prof. Dr. Fatih Mehmet ÖZKAL Atatürk University, Türkiye

CO-EDITOR-IN-CHIEF

Prof. Dr. Serdar ÇARBAŞ Karamanoğlu Mehmetbey University, Türkiye

EDITORIAL BOARD

Prof. Dr. Farid ABED Prof. Dr. Naida ADEMOVIĆ

Prof. Dr. Panagiotis G. ASTERIS

Prof. Dr. M. Asghar BHATTI

Prof. Dr. Alper BÜYÜKKARAGÖZ

Prof. Dr. Stefano DAL PONT

Prof. Dr. Adem DOĞANGÜN

Prof. Dr. Oğuz Akın DÜZGÜN Prof. Dr. Gilbert Rainer GILLICH

Prof. Dr. Taha IBRAHIM

Troi. Dr. Tuna ibianini

Prof. Dr. Reza KIANOUSH

Prof. Dr. Long-Yuan LI

Prof. Dr. Paulo B. LOURENÇO

Prof. Dr. Fabio MAZZA

Prof. Dr. Željana NIKOLIĆ

Prof. Dr. Togay ÖZBAKKALOĞLU

Prof. Dr. Mehmet ÖZYAZICIOĞLU

Prof. Dr. Filiz PİROĞLU

Prof. Dr. Mohammad REZAIEE-PAJAND

Prof. Dr. Bing QU

Prof. Dr. A. Ghani RAZAQPUR

Prof. Dr. Anna SAETTA

Prof. Dr. Mattheos SANTAMOURIS

Prof. Dr. Hélio Luiz SIMONETTI

American University of Sharjah, United Arab Emirates

University of Sarajevo, Bosnia and Herzegovina

School of Pedagogical & Technological Education, Greece

University of Iowa, United States

Gazi University, Türkiye

Université Grenoble Alpes, France

Uludağ University, Türkiye

Atatürk University, Türkiye

Eftimie Murgu University of Resita, Romania

Benha University, Egypt

Ryerson University, Canada

University of Plymouth, United Kingdom

University of Minho, Portugal

University of Calabria, Italy

University of Split, Croatia

Texas State University, United States

Atatürk University, Türkiye

İstanbul Technical University, Türkiye

Ferdowsi University of Mashhad, Iran

California Polytechnic State University, United States

McMaster University, Canada

IUAV University of Venice, Italy

University of New South Wales, Australia

Federal Institute of Minas Gerais, Brazil

Prof. Dr. Y. Cengiz TOKLU

Prof. Dr. Habib UYSAL

Prof. Dr. Wael ZATAR

Assoc. Prof. Dr. Alberto Maria AVOSSA

Assoc. Prof. Dr. Sandro CARBONARI

Assoc. Prof. Dr. Panatchai CHETCHOTISAK

Assoc, Prof. Dr. Burak Kaan CIRPICI

Assoc. Prof. Dr. Dobromir DINEV

Assoc. Prof. Dr. Javier DOMINGUEZ

Assoc. Prof. Dr. Amin GHANNADIASL

Assoc. Prof. Dr. Luca LANDI

Assoc. Prof. Dr. Süleyman Nazif ORHAN

Assoc. Prof. Dr. Hong SHEN

Assoc, Prof. Dr. Nunziante VALOROSO

Assoc. Prof. Dr. Teng WU

Dr. Rayeh Nasr AL-DALA'IEN

Dr. Pierfrancesco CACCIOLA

Dr. Chien-Kuo CHIU

Dr. Hamid GADOURI

Dr. Ehsan HARIRCHIAN

Dr. Anas ISSA

Dr. Parisa KAMRANIMOGHADDAM

Dr. Zühal ÖZDEMİR

Dr. Chitaranjan PANY

Dr. Abbasali SADEGHI

Dr. José SANTOS

Dr. Syahril TAUFIK

Dr. Casim YAZICI

Beykent University, Türkiye

Atatürk University, Türkiye

Marshall University, United States

Second University of Naples, Italy

Marche Polytechnic University, Italy

Rajamangala University of Technology Isan, Thailand

Erzurum Technical University, Türkiye

University of Architecture, Civil Engineering and Geodesy, Bulgaria

National Center for Nuclear Research, Poland

University of Mohaghegh Ardabili, Iran

University of Bologna, Italy

Erzurum Technical University, Türkiye

Shanghai Jiao Tong University, China

Parthenope University of Naples, Italy

University at Buffalo, United States

Al-Balqa Applied University, Jordan

University of Brighton, United Kingdom

National Taiwan University of Science and Technology, Taiwan

Khemis Miliana University, Algeria

Bauhaus-Universität Weimar, Germany

United Arab Emirates University, United Arab Emirates

University of Applied Science and Technology, Iran

The University of Sheffield, United Kingdom

Vikram Sarabhai Space Centre, India

Islamic Azad University, Iran

University of Madeira, Portugal

Lambung Mangkurat University, Indonesia

Ağrı İbrahim Çeçen University, Türkiye

E-mail: cjsmec@challengejournal.com

Web page: cjsmec.challengejournal.com

Tulpar Academic Publishing *www.tulparpublishing.com*





CONTENTS

Research Articles	
Long-term durability of red mud-modified cement mortars: Effects of high temperature and freeze-thaw cycles Emrah Turan, Ibrahim A. Alameri, Meral Oltulu	116–127
Emran Turan, Ibranim A. Alameri, Merai Oitala	
Impact of screw arm angle, material property, and applied force on the behavior of maxillary expander	128-136
Salim Çam, Nurver Karslı, Hojjat Ghahramanzadeh Asl	
Influence of damage state threshold variability on the seismic vulnerability analysis of masonry aqueducts Ali Yesilyurt	137–148
Seismic performance assessment of timber-framed (hımış) structures with different infill materials	149–159
Muhammed Alperen Ozdemir	
Nonlinear in-plane response of 3D-printed concrete walls with varied infill patterns: Experimental mix design and numerical structural assessment İsmail Hakkı Tarhan, Yeşim Tarhan	160-173





Research Article

Long-term durability of red mud-modified cement mortars: Effects of high temperature and freeze-thaw cycles

Emrah Turan ^a , Ibrahim A. Alameri ^{b,c,*} , Meral Oltulu ^a

ABSTRACT

The use of industrial by-products such as red mud in cementitious materials addresses sustainability by reducing environmental impact and improving performance. As a hazardous waste from aluminium production, red mud offers a promising solution for waste management and improves the mechanical and durability properties of mortar when used as a partial cement replacement. This study investigates the long-term mechanical and durability properties of cement mortars modified with red mud, a by-product of alumina production. Red mud was incorporated at substitution percentages of 5%, 10%, 15%, 20%, 25%, 30% and 35% by weight of cement. The mortars were subjected to harsh environmental conditions such as high temperatures (200°C to 600°C), freeze-thaw cycles (50 and 100 cycles), and normal curing conditions at 365 days of age. The study showed that partial replacement of cement with red mud significantly affected the mechanical and durability properties of the mortars. The optimum red mud replacement level of 10% showed that microstructural compactness and hardness were improved by increasing the ultrasonic pulse velocity, dynamic modulus of elasticity and flexural strength. Durability tests showed improved thermal resistance at moderate levels of red mud content, while higher levels adversely affected freeze-thaw performance. These findings confirm that a 10% red mud substitution offers the best balance between strength, durability, and sustainability.

ARTICLE INFO

Article history:

Received – January 10, 2025 Revision requested – February 10, 2025 Revision received – March 6, 2025 Accepted – March 20, 2025

Keywords:

Red mud

Waste materials

Physico-mechanical properties

High temperature

Freeze-thaw

SEM-EDX



This is an open access article distributed under the CC BY licence.

© 2025 by the Authors.

Citation: Turan E, Alameri IA, Oltulu M (2025). Long-term durability of red mud-modified cement mortars: Effects of high temperature and freeze-thaw cycles. Challenge Journal of Structural Mechanics, 11(3), 116–127.

1. Introduction

Cement has been increasingly consumed worldwide every year since 1970 (Vedaiyan and Govindarajalu 2023; Verma et al. 2023). Especially in recent years, it has been emphasized that some limitations should be brought in the amount of production and use of cement in terms of both environmental and energy consumption (Alameri and Oltulu 2020; Oltulu and Alameri 2019).

Optimum use of industrial by-products in the concrete (Bergonzoni et al. 2023; Neves et al. 2023), brick (Kostrzewa-Demczuk et al. 2023; Sruthi and Gayathri

2023), tile manufacturing (Pei et al. 2023) and ceramic industries (Liang et al. 2023) reduces the environmental impact of these materials by minimizing the damage from the disposal of residues as well as conserving available resources (Venkatesh et al. 2019, 2020).

Growing social and environmental concerns have driven the increased use of recycled waste materials as partial replacements for natural resources in construction applications (Yavuz 2024; Aboalella and Elmalky 2023). Red mud is a popular industrial waste, which is an alkaline residue (pH value 10–13.5) formed during alumina production. One ton of alumina production usu-

^a Department of Civil Engineering, Atatürk University, Erzurum 25240, Türkiye

^b Department of Civil Engineering, Sana'a University, 13341 Sana'a, Yemen

^c Department of Civil Engineering, Emirates International University, 16881 Sana'a, Yemen

ally yields 0.8 to 1.8 tons of red mud (Hou et al. 2021; Tang et al. 2019). The main recycling method for red clay is landfilling, which pollutes the surrounding soil and groundwater, posing serious threats to human health, food safety and ecosystem sustainability (Hou et al. 2021; Wang et al. 2020).

Red mud is usually discharged as a slurry with a solids content of 15-40% (Yuan et al. 2020). Its chemical and mineralogical composition depends on the source and processing method of bauxite ores, with the main oxides in typical red mud are CaO, SiO₂, Al₂O₃, Fe₂O₃, TiO₂ and Na₂O (Gao et al. 2023; Yuan et al. 2020). Red mud exhibits the properties of porous materials and offers advantages such as high specific surface area, significant reactivity, cost-effectiveness, and significant solid waste utilization potential. Consequently, it can be used as a partial replacement in the production of cement-based materials (Liu et al. 2019).

In the last decade, red mud has been used as a partial substitute of cement and fine aggregates in concrete (Gou et al. 2023; Zhu et al. 2023). The fine particle size of red mud contributes to the densification of the concrete matrix, reducing microcrack formation and increasing durability. Its inclusion reduces workability while increasing both flexural and compressive strength, especially in the later stages of curing. The higher content of red mud-based concretes resulted in a reduction in strength but a lower rate of corrosion (Venkatesh et al. 2019, 2020). Most studies have limited the incorporation of red mud in cement composites to a maximum of 30% (Anirudh et al. 2021; Díaz et al. 2015; Kang and Kwon 2017; Liu et al. 2019; Nikbin et al. 2018; Ortega et al. 2019; Ribeiro et al. 2013; Venkatesh et al. 2019), However, a few researchers have investigated higher replacement levels, exceeding 50% (Krivenko et al. 2017; Tang et al. 2018, 2019; Yuan et al. 2020).

Venkatesh et al. (2019) and Ortega et al. (2019) found that a denser microstructure formation was observed with the red mud substitution and the chloride-ion passage decreased as the red mud substitution increased. Díaz et al. (2015) concluded that additions of red mud delayed both chloride diffusion and carbonation of cement paste samples. Hou et al. (2021) found that the addition of red mud to ultra-high performance concrete reduces workability and mechanical properties while increasing early age (7d) durability due to the accelerated hydration process.

In addition, research has shown that red mud enhances the mechanical properties and durability of cement-based materials. Tang et al. (2019) reported that replacing fly ash with red mud in self-compacting concrete improves strength and corrosion resistance. Yuan et al. (2020) highlighted its micro-filler effect, reducing harmful pores in binary binders. Hyeok-Jung et al. (2018) found it suitable for pavement applications at replacement rates up to 10%, while Li et al. (2019) noted its role in minimizing surface cracks. Tang et al. (2018) observed slight improvements in the interfacial transition zone of red clay concrete.

In contrast to the above studies that emphasized the mechanical performance, durability, and microstructural improvements of red mud in cement-based materi-

als, Nikbin et al. (2018) investigated its environmental impacts. Their research evaluated the sustainability benefits of red mud in concrete, showing that adding 25% red mud to lightweight concrete can significantly reduce environmental impacts, including cumulative energy demand, global warming potential, and emissions of key air pollutants such as CO, NOx, Pb, and SO₂.

Although previous studies have investigated the use of red mud in cement composites, the focus has largely been on its effect on strength and a limited range of durability properties. However, there is a significant gap in understanding its long-term performance, especially under critical environmental conditions. The present study aims to comprehensively investigate the long-term physico-mechanical properties of red mud cement mortars and their durability under freeze-thaw cycles and high-temperature exposure. Moreover, this research provides valuable insights into the applicability of red mud as a sustainable alternative in cement-based materials

2. Materials and Method

2.1. Materials and sample preparation

In this study, ordinary portland cement (CEM II 42.5 R) was used in accordance with TS EN 196-1 (2016) and TS EN 197-1 (2016) standards. Additionally, red mud, characterized by its specific chemical composition and index properties specified in Table 1, was included as a filler material.

Table 1. Chemical composition and index properties of red mud (RM) and portland cement (PC).

Tou man (m.) and portional comone (r. o).				
Chemical composition (%)	RM	PC		
SiO_2	18.95	17.6		
Al_2O_3	25.65	4.45		
Fe_2O_3	36.94	3.08		
CaO	3.30	60.02		
MgO	-	2.29		
SO_3	-	2.67		
Loss on ignition	17.75	8.49		
Na ₂ O	7.04	0.22		
K ₂ O	-	0.63		
Na ₂ O+0.658K ₂ O	-	0.63		
Cl	-	0.0144		
Unmeasured	-	0.54		
Free CaO	-	0.69		
Total additives	-	19.9		
TiO ₂	5.62	-		
Others	2.51	-		
index properties				
Specific gravity	3.05	3.01		
Specific surface (cm ² /g)	-	4403		
Compressive strength (MPa)	-	51.03		
рН	12-13	-		

The mortar mix design was made according to the TS EN 206 (2014) standard and a water/binder ratio of 0.32 was used. A total of 288 cube specimens (50×50×50 mm) and 32 prism specimens (40×40×160 mm) were prepared, divided into eight groups of cement mortars incorporating red mud at replacement levels of 0%, 5%,

10%, 15%, 20%, 25%, 30%, and 35% by weight of cement. To assess the workability of the fresh concrete, a flow table test was conducted to determine the spreading diameter. Following casting, all samples were cured in water at 25 \pm 2°C for 28 days. Mortar mix proportions are detailed in Table 2.

Table 2. Mortar mix proportions.

Materials used	Cement (%)	Red mud (%)	SPZ (%)	w/b	Spread diameter (cm)
RM0	100	-	0.3	0.32	17.5
RM05	95	5	0.3	0.32	19.5
RM10	90	10	0.3	0.32	17.0
RM15	85	15	0.3	0.32	17.5
RM20	80	20	0.3	0.32	18.0
RM25	75	25	0.3	0.32	17.0
RM30	70	30	0.3	0.32	17.0
RM35	65	35	0.3	0.32	17.0

RM: Red mud, along with its corresponding addition percentage.

SPZ: Superplasticizer.

2.2. Experiments

The impact of reducing cement content through the partial replacement of red mud waste was examined by evaluating the long-term physico-mechanical and durability properties of the specimens. Physico-mechanical properties were assessed based on density, ultrasonic pulse velocity (UPV), dynamic modulus of elasticity (E_d), and compressive strength at 30, 90, and 365 days, as well as flexural strength and modulus of elasticity. Durability performance was analysed by measuring the residual compressive strength after exposure to high temperatures and freeze-thaw cycles.

2.2.1. Density

In this study, the samples were removed from the water pool after 28 days of curing and dried at room conditions (25 °C) for two days. The density of the samples was then calculated by dividing the mass of each sample to the measured volume. The mean value of three samples was calculated for each group to increase the accuracy of the test results.

2.2.2. Ultrasound pulse velocity (UPV)

This test was conducted to evaluate the *UPV* in cement mortar specimens with and without red mud. A digital ultrasonic testing machine operating at 54 kHz was used. Wave propagation time through the mortar samples was determined following the ASTM E494 (2017) standard, and wave velocity was then calculated by dividing the sample length by the recorded time.

The obtained *UPV* was then used to determine the dynamic modulus of elasticity (E_d) using Eq. (1), where ρ represents density, V_{long} denotes longitudinal wave velocity, and ν is Poisson's ratio. In this study, the Poisson's ratio for cement mortars was assumed to be 0.2.

$$E_d = \frac{V_{\text{long}}^2 \cdot \rho \cdot (1+\nu) \cdot (1-2\nu)}{1-\nu} \tag{1}$$

2.2.3. Evaluation of compressive and flexural strength: Testing methods

The compressive and flexural tensile strength tests were carried out following TS EN 12390-3 (2019) and TS EN 12390-6 (2010) standards, respectively, which align with European standards. A 3000 kN capacity testing machine with a position sensor providing 0.001 mm accuracy was used. The load was applied at a constant speed of 0.4 MPa/s for the compressive strength test and 0.04 MPa/s for the flexural tensile strength test. To evaluate the short- and long-term effects of red mud on cement mortar, compression tests were conducted at 30, 90, and 365 days, while flexural strength tests were performed at 365 days. In addition, the modulus of elasticity was determined using the stress-strain curves obtained from 365-day compression tests in accordance with the TS 12390-2 (2019) standard.

2.2.4. High temperature resistance

This study investigated the residual compressive strength of the mortar after exposure to high temperatures. The samples were stored at 25 °C under laboratory conditions and the test was carried out on the 365th day. To prevent explosive spalling caused by steam formation, the samples were pre-dried at 100 °C for 24 h before exposure to high temperatures (Alameri and Oltulu 2020). Heating was carried out in an electric furnace with a maximum capacity of 1000°C following the heating and cooling protocol shown in Fig. 1. The samples were exposed to temperatures of 200 °C, 400 °C, and 600 °C, with a dwell time of 2 hours at each temperature.

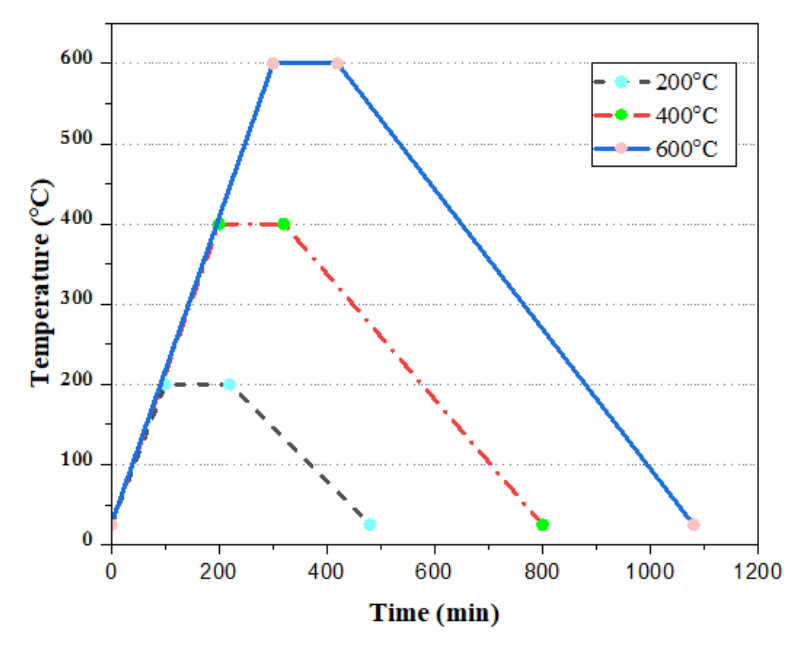


Fig. 1. Heating and cooling regime.

2.2.5. Freeze-thaw resistance

In cold climates such as Erzurum Province, where this experimental study was conducted, cement mortars exposed to freeze-thaw cycles inevitably undergo a certain degree of damage. In this study, 365-day-old cement mortars with and without red mud were subjected to freeze-thaw testing following ASTM C666/C666M (2015) (Procedure A). The samples were subjected to 50 and 100 freeze-thaw cycles, each covering a temperature range of -18 °C to +4 °C for 240 min. After completion of the cycles, the samples were visually inspected and their residual compressive strength was evaluated.

3. Results and Discussion

3.1. Physico-mechanical properties

3.1.1. Density

Density results are summarized in Table 3 and shown in Fig. 2. The density of the mortar mixes showed signif-

icant differences depending on the red mud (RM) content, ranging from 1.96 g/cm³ (RM05) to 2.28 g/cm³ (RM10). Compared to the control mix (RM0) with a density of 1.98 g/cm³, RM10 showed the highest increase, reflecting an increase of 15.15%. This improvement can be attributed to the filler effect of red mud, where the fine particles increased the packing density and contributed to a more compact microstructure. The increased density in RM10 suggests that moderate replacement of cement with red mud increased the overall matrix cohesion, leading to better densification. However, beyond this optimum level, the density showed a downward trend, indicating a decline in structural compactness.

The decrease in density at higher substitution levels, particularly for RM30 ($2.04~g/cm^3$) and RM35 ($2.19~g/cm^3$), indicate an increase in porosity. Excessive red mud content can lead to insufficient cementitious bonding and void formation, which collectively reduces the overall compactness of the mortars.

Table 3.	Physico-mec	hanical	properties.

Group	Density (g/cm³)	UPV (m/s)	E _d (GPa)	30-day compressive strength (MPa)	90-day compressive strength (MPa)	365-day compressive strength (MPa)	Flexural strength (MPa)	E (GPa)
RM0	1.98	3361	20.13	71.01	84.60	87.90	4.93	9.4
RM05	1.96	3252	18.66	76.75	79.10	86.30	5.26	8.6
RM10	2.28	3333	22.80	71.21	75.73	78.70	5.87	8.5
RM15	2.04	3175	18.50	62.31	67.79	72.20	5.76	8.1
RM20	1.98	3200	18.25	58.49	63.40	63.40	5.26	7.5
RM25	2.25	3175	20.41	57.62	60.64	60.70	5.00	7.5
RM30	2.04	3101	17.65	50.85	54.17	61.00	4.73	6.4
RM35	2.19	3175	19.86	46.16	48.75	60.80	4.23	6.5

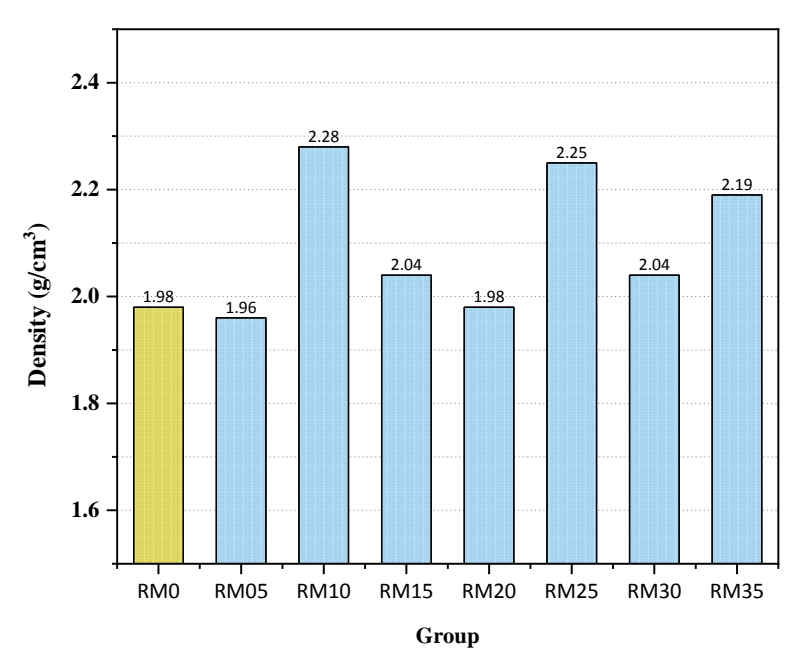


Fig. 2. Density results of the tested groups.

3.1.2. Ultrasonic pulse velocity (UPV)

The UPV results are summarized in Table 3 and shown in Fig. 3. The control group (RM0) showed the highest *UPV* value of 3361 m/s. Among the groups containing red mud, RM10 achieved a *UPV* of 3333 m/s, which was only a 0.83% decrease compared to the control, indicating that up to 10% red mud content did not significantly compromise the density or homogeneity of

the mortar. A consistent decrease in *UPV* was observed with the increase in red mud content, and RM30 showed the lowest speed of 3101 m/s (-7.73%). The observed decrease in *UPV* at higher red clay ratios can be attributed to increased porosity and potential microcrack formation, which hinders wave propagation, as confirmed by other studies linking high additive content to lower pulse speeds due to poor bonding and incomplete hydration (Qureshi et al. 2022).

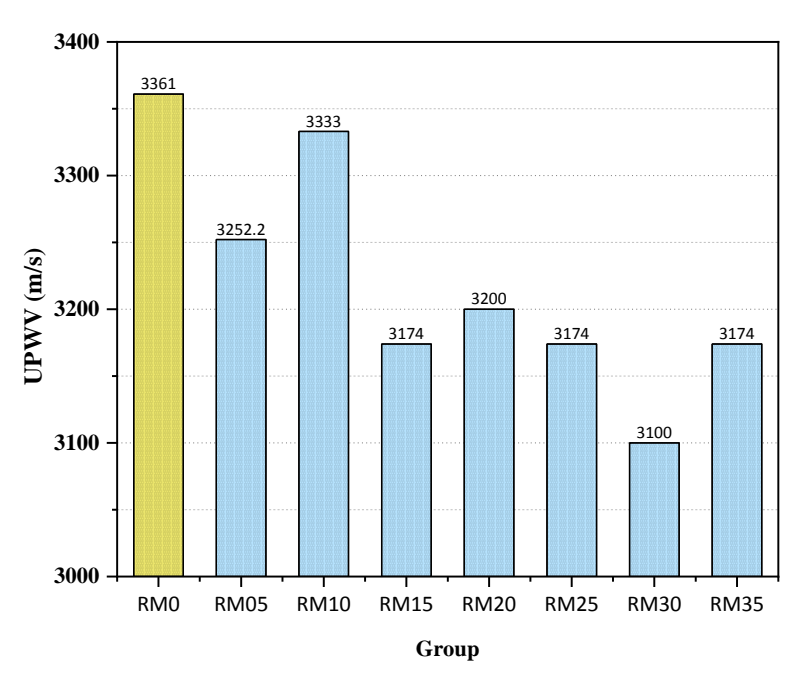


Fig. 3. UPV results of the tested groups.

3.1.3. Dynamic modulus of elasticity (E_d)

The average dynamic modulus of elasticity values of mortars are summarized in Table 3 and shown in Fig. 4.

The dynamic modulus of elasticity (E_d) results showed a strong correlation with both density and ultrasound pulse wave (UPV) velocity, reflecting the stiffness and internal compactness of the mortars. The RM10 group

showed the highest E_d value of 22.80 GPa, representing a 13.2% increase compared to the control group (RM0). RM05 and RM15 showed E_d values of 18.66 GPa and 18.50 GPa, respectively, indicating decreases of approximately 7.3% and 8.0%. Further increases in RM content led to varying effects; RM20 experienced a slight decrease in E_d to 18.25 GPa (-9.5%), while RM25 increased to 20.41 GPa (+1.4%). However, higher RM contents, such as RM30 and RM35, resulted in a decrease in E_d val-

ues of 17.65 GPa (-12.2%) and 19.86 GPa (1.3%), respectively. The variations in E_d values can be attributed to the interplay between UPV and density, both of which affect the E_d . The RM10 group exhibited the highest UPV, which, together with its optimal density, contributed to its superior E_d value. Adding red mud up to a 10% replacement ratio appears to optimize these properties, increasing the stiffness and structural performance of the material.

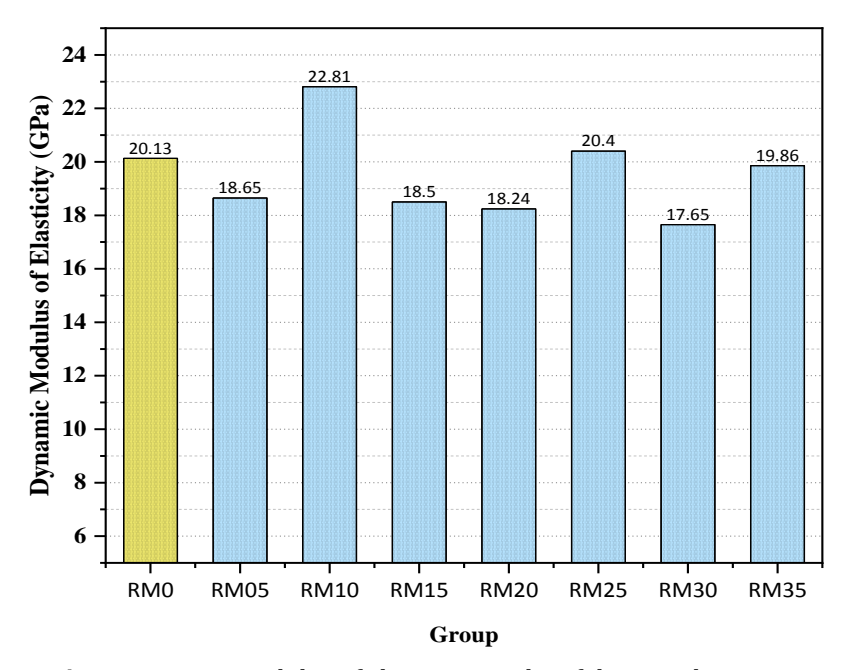


Fig. 4. Dynamic modulus of elasticity results of the tested groups.

3.1.4. Compressive strength

The compressive strength results at different ages showed significant variations depending on the red mud (RM) content (Table 3 and Fig. 5). At 30 days, the RM05 group achieved the highest compressive strength of 76.75 MPa, surpassing the control group (RM0) by approximately 8.1%. This improvement is primarily attributed to the filler effect of the red mud particles, which occupy voids within the cement matrix, leading to a denser microstructure and improved early-age strength. Additionally, the pozzolanic activity of the red mud contributes to the formation of calcium silicate hydrate (C-S-H) gel, further increasing the strength. However, a gradual decrease in compressive strength was observed as the red mud content increased beyond 5%. The RM15 group showed a decrease to 62.31 MPa (-12.3%). This decrease can be attributed to several factors, including that excessive RM can reduce strength by increasing total porosity. Replacing cement with RM reduces the overall amount of cementitious material, potentially weakening the bond strength between the cement paste and the aggregates (Ai et al. 2021; Wang and Zhen 2024).

At 90 days, the control group (RM0) showed the largest increase in compressive strength, increasing by approximately 19.1%, from 71.01 MPa at 28 days to 84.60 MPa at 90 days. This improvement is due to the continuous hydration of the cement particles, which allows the

matrix to gain strength over time. In contrast, groups with red mud content showed more modest increases in strength or relatively smaller changes. Compared to 30day strength, the RM05 group increased (+3.0%), RM10 (+6.3%), RM15 (+8.8%), RM20 (+8.5%), RM25 (+5.2%), RM30 (+6.3%), and RM35 (+5.5%). These results suggest that the incorporation of red mud (up to 20%) leads to an increase in compressive strength at 90 days compared to the 28-day strength. However, when the red mud content exceeds 20%, the strength gain begins to decrease. Adding up to 20% red mud to cementitious materials increases compressive strength gain over time, which is attributed to its pozzolanic activity that contributes to cement hydration and forms additional C-S-H gel, improving the microstructure and strength of the mortar. Beyond this threshold, the introduction of impurities such as sodium, iron, and other alkaline compounds can interfere with the hydration process, inhibiting C-S-H gel formation and weakening the bond between cement particles and aggregates. In addition, higher red mud content can increase porosity, resulting in a less dense microstructure and reduced strength.

At 365 days, the control group (RM0) exhibits a strength increase of approximately 3.9%, rising from 84.60 MPa at 90 days to 87.90 MPa at 365 days. Similarly, the RM10 group shows a 3.92% increase, with strengths increasing from 75.73 MPa at 90 days to 78.70 MPa at 365 days. In contrast, the RM35 group experiences a

more substantial gain of 24.72%, with compressive strength increasing from 48.75 MPa at 90 days to 60.80 MPa at 365 days. These observations suggest that higher

red mud content may contribute to long-term strength development, potentially due to ongoing pozzolanic reactions and microstructural improvements over time.

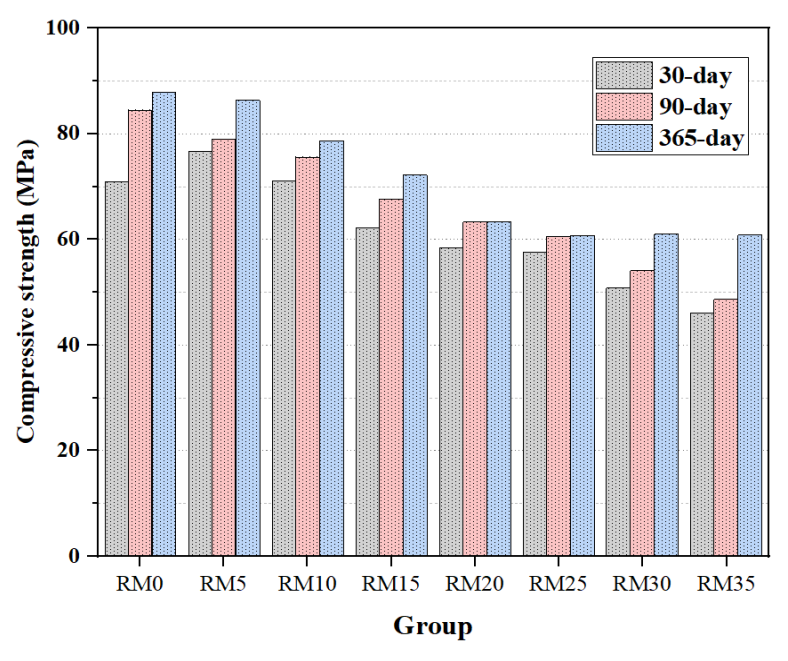


Fig. 5. 30-day, 90-day and 365-day compressive strength results.

As shown in the stress-strain curve (Fig. 6), the stress-strain response in red mud-containing mortars remained more stable beyond the ultimate strength, while the reference group (RM0) showed a sharp decrease.

This behaviour may be due to the densification effect of red mud at optimal levels, which enhances post-peak structural integrity by improving the pore structure and load redistribution mechanisms.

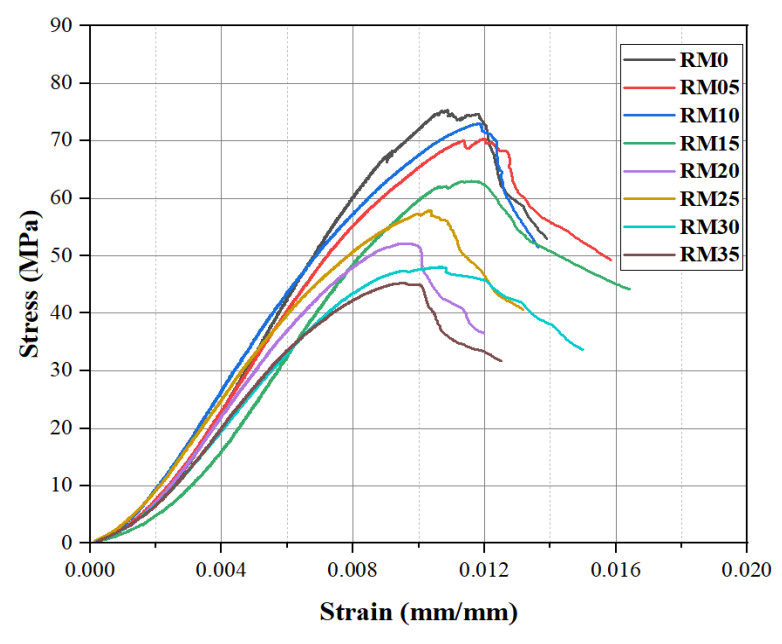


Fig. 6. 28-day stress-strain curves.

3.1.5. Modulus of elasticity

The modulus of elasticity (*E*) results are summarized in Table 3 and shown in Fig. 7. The results showed a clear dependence on the red mud (RM) content, reflecting the changes in stiffness and material deformation

behaviour. The RM0 (control) group exhibits the highest *E* at 9.4 GPa. The RM05 group shows a decrease of approximately 8.51% compared to the control. The modulus of elasticity continues to decrease as the red mud content increases, with the RM30 group experiencing a significant decrease of approximately 31.91%. The

RM35 group also shows a significant decrease in E of approximately 30.85% compared to the control. The decrease in E can be attributed to the deterioration of the

uniformity and compactness of the microstructure, resulting in a less rigid network and hence a lower modulus

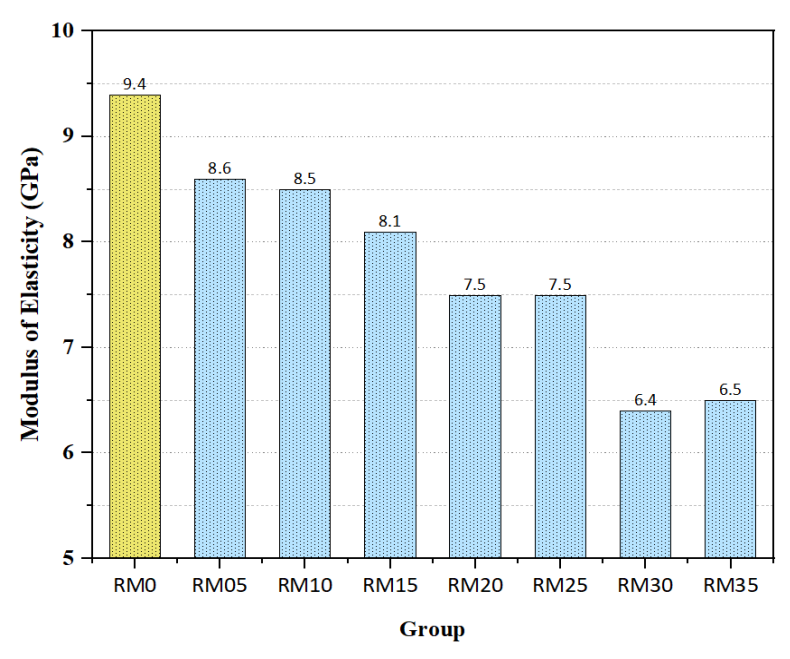


Fig. 7. Modulus of elasticity results of the tested groups.

3.1.6. Flexural tensile strength

In this study, the long term (365-day) flexural tensile strength was examined and the results are summarized in Table 3 and shown in Fig. 8. This improvement in flexural strength continues up to the 10% replacement level, after which strength begins to decrease. The RM10 group exhibits the highest flexural strength at 5.87 MPa, an increase of approximately 19.1% compared to the control group. The RM15 group exhibits a slight decrease to 5.76 MPa (approximately 16.8% higher than the control group), and the RM35 group exhibits the low-

est flexural strength at 4.23 MPa, a decrease of approximately 14.2% compared to the control group. A similar trend was observed for compressive strength, where excessive red mud resulted in reduced strength due to increased porosity and weaker cementitious bonding. This correlation indicates that beyond 10% red mud content, red mud impairs matrix integrity, adversely affecting both tensile and compressive performance. These findings confirm that moderate red mud inclusion enhances strength, while excessive amounts negatively affect the mechanical properties, highlighting the importance of optimized replacement levels for structural reliability.

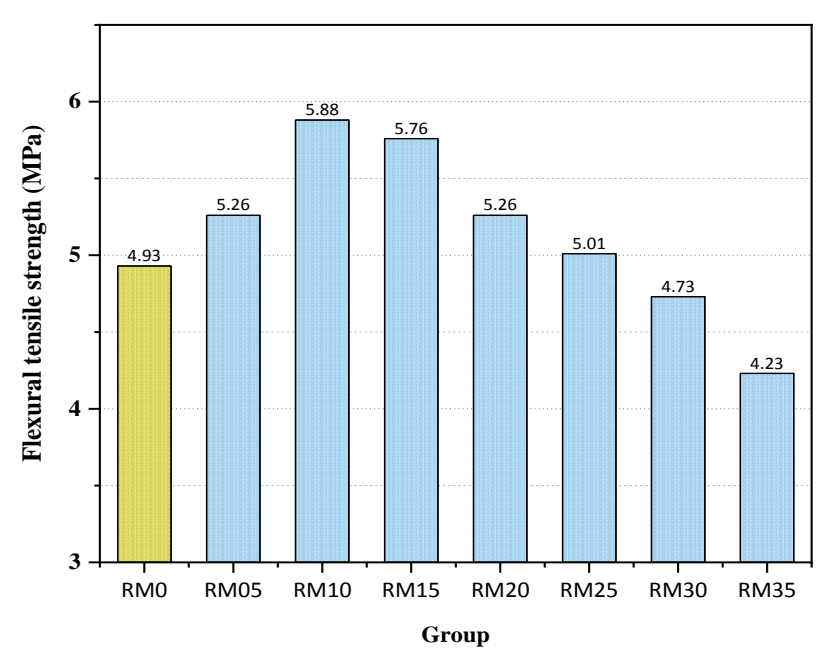


Fig. 8. Flexural strength results of the tested groups.

3.1.7. Durability properties

3.1.7.a. Effect of exposure temperature on compressive strength

Residual compressive strength results are summarized in Table 4 and shown in Fig. 9. After 365 days of normal curing, the control mixture (RM0) exhibited a compressive strength of 87.9 MPa, which increased to 95.5 MPa, reflecting an 8.6% strength gain after exposure to 200°C. This improvement is attributed to the continuous hydration of unreacted cement particles and the reduction of free water, which increases matrix densification. Similarly, RM15 and RM20 showed the highest strength increases, rising by 10.2% and 13.9%, respectively.

In contrast, RM10 and RM05 showed reductions of 8.9% and 7.5%, respectively, indicating that certain RM levels may cause internal shrinkage stresses or increased microcracks under thermal exposure. Although RM15 and RM20 outperformed RM0 in relative strength gain, higher RM contents exhibited decreasing thermal efficiency. RM30 and RM35 only retained 65.5 MPa and 62.0 MPa, respectively, which are 31.4% and 35.1% lower than RM0 at 200°C. Although these groups showed minor strength improvements compared to their normal case values (7.4% and 2.0%, respectively), their overall performance remained significantly weaker than the control. This suggests that excessive RM replacement increased porosity and weakened cementitious bonding, leading to lower thermal resistance.

At 400 °C, the control group (RM0) experienced a significant strength reduction, decreasing from 87.9 MPa to 68.7 MPa (21.9% reduction), indicating thermal-induced microcracking and dehydration effects. RM05, RM10, and RM15 showed similar reductions of 22.8%, 14.1%, and 13.5%, respectively, indicating that moderate RM incorporation slightly improved the thermal resistance. However, higher RM contents (RM20–RM35) experienced larger reductions, with RM35 decreasing by 30.6%.

Compared with RM0 at 400 °C, RM10 and RM15 retained higher strength (67.6 MPa and 62.4 MPa, respec-

tively) with less than 15% loss, indicating improved thermal stability. However, RM30 and RM35 exhibited 17.0% and 38.7% lower strength than RM0, respectively, confirming that excessive RM incorporation leads to thermal degradation.

After exposure to 600 °C, the control mix (RM0) experienced a significant strength reduction, from 87.9 MPa to 62.9 MPa, representing a 28.5% loss. RM05 and RM10 showed a strength reduction of 35.1% and 32.8%, respectively. Although moderate red mud incorporation slightly alleviated thermal degradation, strength losses remained significant. In contrast, RM15 showed a slight strength increase of 3.9%.

3.1.7.b. Effect of freeze-thaw on compressive strength

Residual compressive strength results are summarized in Table 4 and shown in Fig. 10. After 50 freezethaw cycles, the control group (RM0) showed a decrease in compressive strength from 87.9 MPa to 81.6 MPa, a decrease of 6.3%, indicating the effect of freeze-thaw cycles on the cementitious matrix, leading to microcracks and pore expansion. RM05, RM10, RM15, RM20, and RM25 showed similar decreases of 12.4%, 17.6%, 16.2%, 26.4%, and 14.5%, respectively, indicating that RM incorporation experienced more significant strength losses due to freeze-thaw damage by weakening the microstructure and increasing water absorption during the cycles.

After 100 freeze-thaw cycles, the control group (RM0) deteriorated further and decreased to 76.0 MPa (13.5% decrease from the original 87.9 MPa). This decrease is attributed to extensive internal damage due to repeated freezing and thawing, which increased pore connectivity and promoted cracking. Similarly, RM05, RM10, and RM15 showed decreases of 14.9%, 15.2%, and 30.2%, respectively. In particular, RM30 and RM35 showed larger decreases of 39.5% and 40.0%; indicating that higher red mud contents significantly reduce freeze-thaw durability, probably due to weaker microstructural cohesion and increased porosity.

Table 4. Compressive strength test results after exposure to high temperatures and freeze-thaw cy	cles.
--	-------

Group	365-day avg. comp. strength after high temp. (MPa)		365-day avg. comp. after freeze thaw cycles (
Group	200°C	400°C	600°C	50 cycles	100 cycles
RM0	95.5	68.7	62.9	81.6	76.0
RM5	79.8	66.6	56.1	75.5	73.5
RM10	71.7	67.6	53.3	61.9	50.0
RM15	79.6	62.4	65.0	60.5	50.1
RM20	72.2	52.4	52.4	43.6	41.0
RM25	65.9	61.4	44.0	52.0	47.9
RM30	65.5	57.0	50.0	43.3	37.0
RM35	62.0	42.1	46.1	44.4	36.0

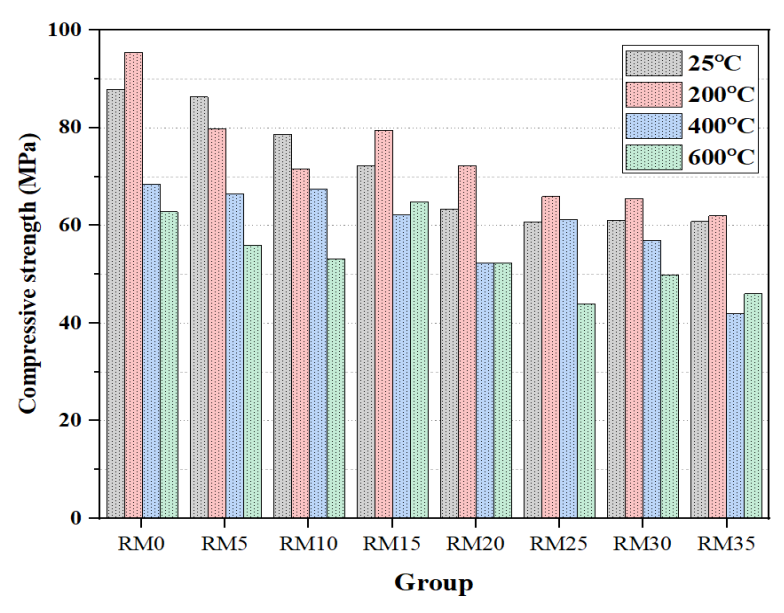


Fig. 9. 365-day average compressive strength results of the tested groups after exposure to elevated temperatures.

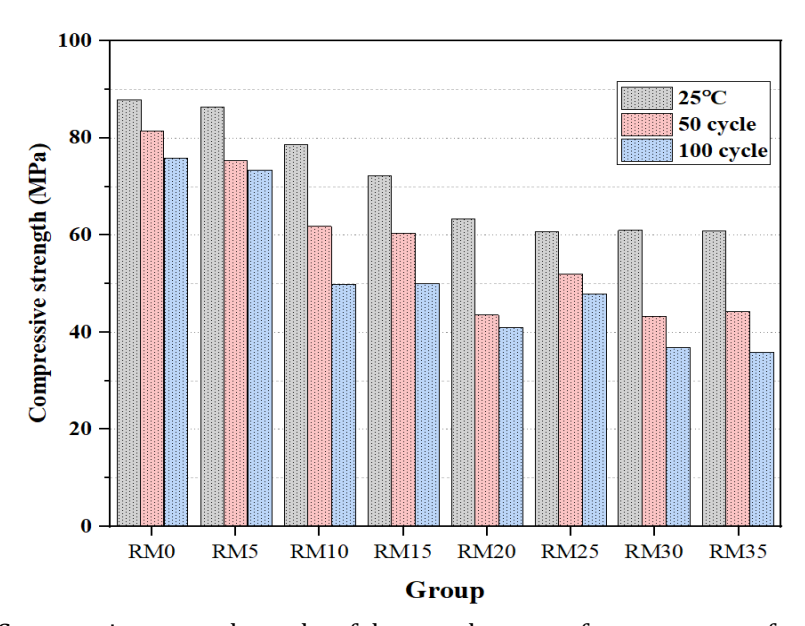


Fig. 10. Compressive strength results of the tested groups after exposure to freeze-thaw.

SEM-EDX analysis was conducted on sample RM5 to examine its microstructure and confirm the uniform distribution of red mud. Additionally, EDX results revealed the chemical composition present in the sample (Fig. 11).

4. Conclusions

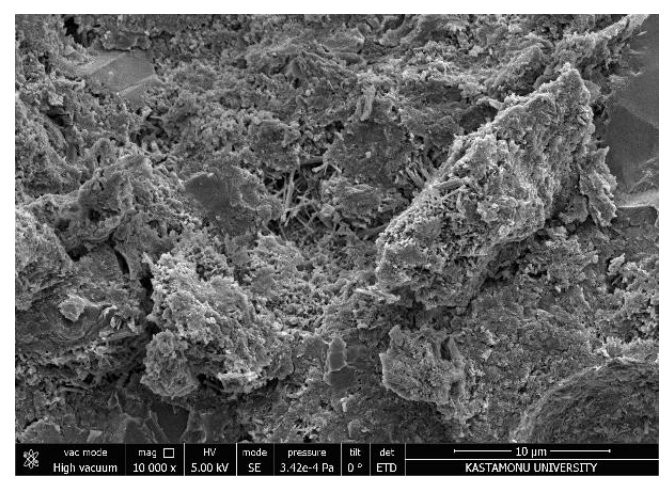
This study investigated the effects of red mud (RM) incorporation on the mechanical properties of cement mortars, with particular emphasis on compressive strength, durability under thermal and freeze-thaw conditions, and long-term effects after 365 days. The results revealed that:

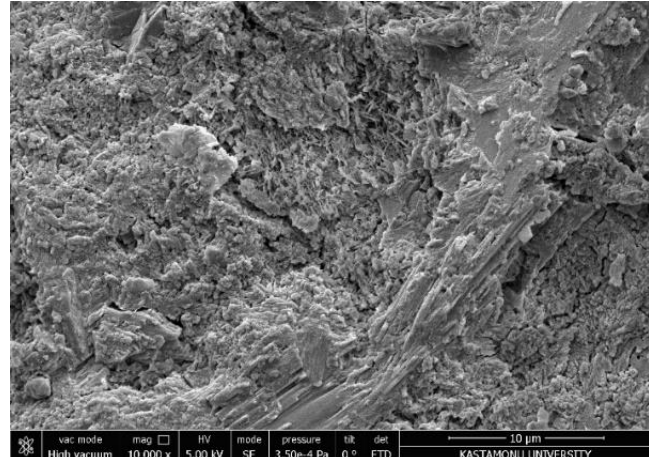
Incorporating red mud at a 10% replacement ratio provided optimal enhancement of mortar performance, significantly improving density, dynamic modulus of elasticity, and flexural strength due to better particle packing and refined microstructural compactness.

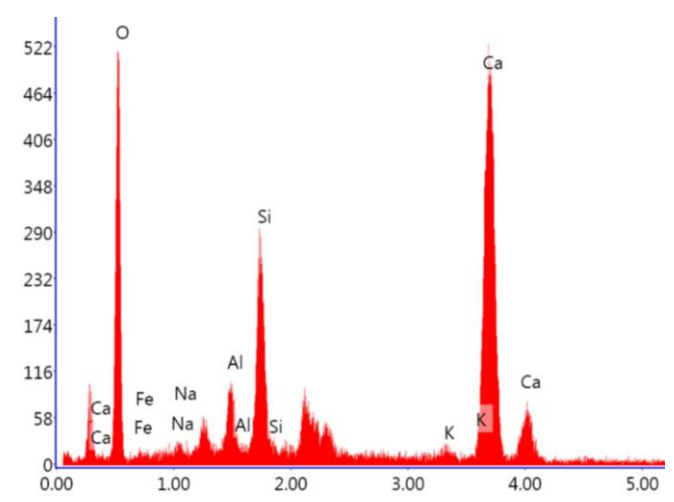
- Compressive strength results showed that red mud content up to 10% increased early and long-term strength, while higher replacement levels (above 20%) led to strength reduction due to increased porosity and decreased cementitious bonding.
- Durability assessments revealed that moderate red mud incorporation improved thermal resistance up to 400 °C, while higher contents significantly reduced freeze-thaw resistance, primarily due to poor microstructural integrity.

The following recommendations are provided for future studies:

- Examination of the changes in properties with different curing methods.
- Detailed pore structure and microstructural studies are recommended on the subject.
- Examination the other durability properties such as acidic and sulphate attack.







Element	Weight (%)	Atomic (%)
0	47.3	67.54
Na	0.72	0.71
Al	2.42	2.05
Si	7.48	6.09
K	0.61	0.36
Ca	39.08	22.27
Fe	2.40	0.98

Fig. 11. SEM-EDX analysis of sample RM5.

Acknowledgements

None declared.

Funding

The authors received no financial support for the research, authorship, and/or publication of this manuscript.

Conflict of Interest

The authors declared no potential conflicts of interest with respect to the research, authorship, and/or publication of this manuscript.

Author Contributions

All of the authors made substantial contributions to conception and design, or acquisition of data, or analysis and interpretation of data; were involved in drafting the manuscript or revising it critically for important intellectual content; and gave final approval of the version to be published.

Data Availability

The datasets created and/or analyzed during the current study are not publicly available, but are available from the corresponding author upon reasonable request.

REFERENCES

Aboalella AA, Elmalky A (2023). Use of crushed bricks and recycled concrete as replacement for fine and coarse aggregates for sustainable concrete production. *Challenge Journal of Concrete Research Letters*, 14(2), 39-46.

Ai T, Zhong D, Zhang Y, Zong J, Yan X, Niu Y (2021). The effect of red mud content on the compressive strength of geopolymers under different curing systems. *Buildings*, 11(7), 298.

Alameri IA, Oltulu M (2020). The physico-mechanical properties of concrete with red mud at high temperatures. *Challenge Journal of Concrete Research Letters*, 11(4), 82-91.

Anirudh M, Rekha KS, Venkatesh C, Nerella R (2021). Characterization of red mud based cement mortar; mechanical and microstructure studies. *Materials Today: Proceedings*, 43, 1587-1591.

ASTM C666 / C666M – 15 (2015). Standard test method for resistance of concrete to rapid freezing and thawing. ASTM International, West Conshohocken, PA, USA.

ASTM E494 – 95 (2017). Standard practice for measuring ultrasonic velocity in materials. ASTM International, West Conshohocken, PA, USA.

Bergonzoni M, Melloni R, Botti L (2023). Analysis of sustainable concrete obtained from the by-products of an industrial process and recycled aggregates from construction and demolition waste. *Procedia Computer Science*, 217, 41-51.

Díaz B, Freire L, Nóvoa XR, Pérez MC (2015). Chloride and CO₂ transport in cement paste containing red mud. *Cement and Concrete Composites*, 62, 178-186.

- Gao Y, Li Z, Xin G, Shen Q, Zhang J, Yang Y (2023). Utilization of highvolume red mud application in cement-based grouting material: Effects on mechanical properties at different activation modes. *Jour*nal of Materials in Civil Engineering, 35(4), 04023011.
- Gou M, Hou W, Zhou L, Zhao J, Zhao M (2023). Preparation and properties of calcium aluminate cement with Bayer red mud. Construction and Building Materials, 373, 130827.
- Hou D, Wu D, Wang X, Gao S, Yu R, Li M, Wang P, Wang Y (2021). Sustainable use of red mud in ultra-high performance concrete (UHPC): Design and performance evaluation. *Cement and Concrete Composites*. 115, 103862.
- Hyeok-Jung K, Kang SP, Choe GC (2018). Effect of red mud content on strength and efflorescence in pavement using alkali-activated slag cement. *International Journal of Concrete Structures and Materials*, 12, 19
- Kang SP, Kwon SJ (2017). Effects of red mud and alkali-activated slag cement on efflorescence in cement mortar. Construction and Building Materials, 133, 459-467.
- Kostrzewa-Demczuk P, Stepien A, Dachowski R, da Silva RB (2023). Influence of waste basalt powder addition on the microstructure and mechanical properties of autoclave brick. *Materials*, 16(2), 870.
- Krivenko P, Kovalchuk O, Pasko A, Croymans T, Hult M, Lutter G, Vandevenne N, Schreurs S, Schroeyers W (2017). Development of alkali activated cements and concrete mixture design with high volumes of red mud. Construction and Building Materials, 151, 819-826.
- Li X, Zhang Q, Mao S, Li L, Wang J (2019). Study on the preparation and fracture behavior of red mud-yellow phosphorus slag-based concrete. *Advances in Materials Science and Engineering*, 2019, 1-15.
- Liang L, Du X, Gao X, Wang Y, Zhang J, Xue X, Shi S, Su N, Zhang K, Li G (2023). Construction and optimization of Fe₃O₄/C/ceramic composite absorbents by one-step recycling red mud and coal hydrogasification residue. *Materials Today Communications*, 34, 105303.
- Liu C, Wu H, Jiang J, Wang L, Kong D, Yu K (2023). Properties of flue gas desulphurization gypsum-activated steel slag fine aggregate red mud-based concrete. *Journal of Materials in Civil Engineering*, 35(4), 04023025.
- Liu Z, Zhang S, Hu D, Zhang Y, Lv H, Liu C, Chen Y, Sun J (2019). Paraffin/red mud phase change energy storage composite incorporated gypsum-based and cement-based materials: Microstructures, thermal and mechanical properties. *Journal of Hazardous Materials*, 364, 608-620.
- Neves A, Almeida J, Cruz F, Miranda T, Cunha VMCF, Rodrigues M, Costa J, Pereira EB (2023). Design procedures for sustainable structural concretes using wastes and industrial by-products. *Applied Sciences*, 13(4), 2087.
- Nikbin IM, Aliaghazadeh M, Charkhtab S, Fathollahpour A (2018). Environmental impacts and mechanical properties of lightweight concrete containing bauxite residue (red mud). *Journal of Cleaner Production*, 172, 2683-2694.
- Oltulu M, Alameri I (2019). The mechanical properties of concrete with red mud (bauxite residue) and nano-Al $_2$ O $_3$ at high temperatures. Fresenius Environmental Bulletin, 28(6), 4692-4701.
- Ortega J, Cabeza M, Tenza-Abril A, Real-Herraiz T, Climent M, Sánchez I (2019). Effects of red mud addition in the microstructure, durability and mechanical performance of cement mortars. *Applied Sciences*, 9(5), 984.
- Pei J, Pan X, Wang Y, Lv Z, Yu H, Tu G (2023). Effects of alkali and alkaline-earth oxides on preparation of red mud based ultra-light-weight ceramsite. *Ceramics International*, 49(11, Part B), 18379-18387

- Qureshi HJ, Ahmad J, Majdi A, Saleem MU, Al Fuhaid AF, Arifuzzaman M (2022). A study on sustainable concrete with partial substitution of cement with red mud: A review. *Materials*, 15(21), 7761.
- Ribeiro DV, Silva AS, Labrincha JA, Morelli MR (2013). Rheological properties and hydration behavior of portland cement mortars containing calcined red mud. *Canadian Journal of Civil Engineering*, 40(6), 557-566.
- Sruthi S, Gayathri V (2023). Synthesis and evaluation of eco-friendly, ambient-cured, geopolymer-based bricks using industrial by-products. *Buildings*, 13(2), 510.
- Tang WC, Wang Z, Liu Y, Cui HZ (2018). Influence of red mud on fresh and hardened properties of self-compacting concrete. *Construction and Building Materials*, 178, 288-300.
- Tang WC, Wang Z, Donne SW, Forghani M, Liu Y (2019). Influence of red mud on mechanical and durability performance of self-compacting concrete. *Journal of Hazardous Materials*, 379, 120802.
- TS EN 196-1 (2016). Methods of testing cement Part 1: Determination of strength. Turkish Standards Institution, Ankara, Türkiye.
- TS EN 197-1 (2016). Cement Composition, specifications and conformity criteria for common cements. Turkish Standards Institution, Ankara, Türkiye.
- TS EN 206 (2014). Concrete Specification, performance, production, and conformity. Turkish Standards Institution, Ankara, Türkiye.
- TS EN 12390-3 (2019). Testing hardened concrete Part 3: Compressive strength of test specimens. Turkish Standards Institution, Ankara, Türkiye.
- TS EN 12390-6 (2010). Testing hardened concrete Part 6: Tensile splitting strength of test specimens. Turkish Standards Institution, Ankara, Türkiye.
- Vedaiyan B, Govindarajalu E (2023). A multi-objective robust grey wolf optimization model for the study of concrete mix using copper slag and glass powder. *International Journal of Advanced Manufacturing Technology*, 125(3), 1941-1953.
- Venkatesh C, Nerella R, Chand MSR (2019). Comparison of mechanical and durability properties of treated and untreated red mud concrete. *Materials Today: Proceedings*, 27, 284-287.
- Venkatesh C, Nerella R, Chand MSR (2020). Experimental investigation of strength, durability, and microstructure of red-mud concrete. *Journal of the Korean Ceramic Society*, 57(2), 167-174.
- Verma NK, Meesala CR, Kumar S (2023). Developing an ANN prediction model for compressive strength of fly ash-based geopolymer concrete with experimental investigation. *Neural Computing and Appli*cations, 35, 10329–10345.
- Wang L, Chen L, Guo B, Tsang DCW, Huang L, Ok YS, Mechtcherine V (2020). Red mud-enhanced magnesium phosphate cement for remediation of Pb and As contaminated soil. *Journal of Hazardous Materials*, 400, 123317.
- Wang Y, Zhen Z (2024). Properties of red-mud-modified basic magnesium sulfate cement. *Materials*, 17(16), 4085.
- Yavuz D (2024). Freeze-thaw and drop-weight impact resistance of fiber-reinforced pervious concretes produced using recycled pervious concrete aggregate. Challenge Journal of Structural Mechanics, 10(4), 138-148.
- Yuan B, Yuan S, Straub C, Chen W (2020). Activation of binary binder containing fly ash and portland cement using red mud as alkali source and its application in controlled low-strength materials. *Journal of Materials in Civil Engineering*, 32(2), 04019356.
- Zhu J, Yue H, Ma L, Li Z, Bai R (2023). Study on hydration mechanism and environmental safety of thermal activated red mud-based cementitious materials. *Environmental Science and Pollution Research*, 30, 55905–55921.



Research Article

Impact of screw arm angle, material property, and applied force on the behavior of maxillary expander

Salim Çam ^a , Nurver Karslı ^{b,*} , Hojjat Ghahramanzadeh Asl ^c

- ^a Department of Mechanical Engineering, Erzincan Binali Yıldırım University, 24002 Erzincan, Türkiye
- ^b Department of Orthodontics, Karadeniz Technical University, 61080 Trabzon, Türkiye
- ^c Department of Mechanical Engineering, Karadeniz Technical University, 61080 Trabzon, Türkiye

ABSTRACT

A unilateral or bilateral posterior crossbite is a common and severe malocclusion characterized by maxillary transversal deficiency. Various expansion appliances are employed to correct this condition. The objective of this study was to evaluate the forces transmitted to the teeth and the deformation of the expander appliance resulting from modifications to the screw arms of a slow maxillary expander with different angles, using finite element analysis. All models were created in SolidWorks and analyzed using ANSYS Workbench. The analysis revealed that the models with different angular configurations of the expander screw arms (0°, 15°, and 30°) exhibited very similar reaction forces on the teeth. However, significant differences in deformation values were observed among the models. The most effective parameter is the force applied to the expander with a rate of 46%, followed by the arm angle with a rate of 44%, while the effect of material type is 10%. The most significant conclusion that can be drawn from these findings is that the arm angle is as important as the force applied to the expander. In situations where the force that can be applied is limited by various factors, it can be demonstrated that altering the arm angle can lead to the achievement of the desired outcome.

ARTICLE INFO

Article history:

Received – February 25, 2025 Revision requested – March 25, 2025 Revision received – April 1, 2025 Accepted – April 14, 2025

Keywords:

Crossbite

Expansion

Screw arm

Finite element analysis



This is an open access article distributed under the CC BY licence.

© 2025 by the Authors.

Citation: Çam S, Karslı N, Ghahramanzadeh Asl H (2025). Impact of screw arm angle, material property, and applied force on the behavior of maxillary expander. *Challenge Journal of Structural Mechanics*, 11(3), 128–136.

1. Introduction

Transversal maxillary deficiency (TMD) is a prevalent malocclusion that necessitates early intervention in orthodontics. The transverse dimensional discrepancy in maxillo-mandibular relationships often leads to the development of posterior crossbite, which can be either unilateral or bilateral. Posterior crossbite is particularly common during the mixed dentition (Da Silva Filho et al. 2007; Leonardi et al. 2018). Unilateral posterior crossbite is typically associated with lateral displacement of the mandible, resulting from maxillary transverse deficiency in maximal intercuspation. This condition causes the mandibular midline to shift toward the side of the crossbite (Alsawaf et al. 2022; Kutin and Hawes 1969).

Such a change has been shown to lead to the development of craniofacial asymmetry in adulthood. Therefore, early diagnosis and management of this condition is essential to prevent long-term functional and aesthetic complications (Tsanidis et al. 2016).

Traditional rapid maxillary expanders (RMEs) are widely recognized as effective for correcting TMD (Silveira et al. 2021). These devices deliver heavy and intermittent forces to the dento-skeletal structures, promoting rapid expansion (Isaacson and Ingram 1964; Haas 1970). In contrast, slow maxillary expanders (SMEs) aim to achieve more gradual expansion by focusing on maximizing dental effects while applying lower, continuous force levels (Andrew 1985). Furthermore, nickel-titanium (Ni-Ti) expanders have been introduced, which

provide continuous, low-level force application, enhancing comfort and treatment efficiency (Arndt 2004; Wichelhaus et al. 2004). Among these, the Ni-Ti Memoria Leaf Spring Self-Activated Expander has been developed as an innovative expansion device, further optimizing the expansion process (Gianolio et al. 2015). It has been reported that the Ni-Ti MEMORIA® Leaf Spring Expander is utilized in growing patients for the correction of transverse maxillary insufficiency. It provides adequate expansion without significantly tipping the teeth and is regarded as an effective device for slow expansion when used in accordance with the recommended protocol (Manzella et al. 2018). Furthermore, research has shown that both the Rapid Palatal Expander and the Leaf Expander induce similar changes in palatal surface area in individuals with maxillary transverse deficiency during the mixed dentition period (Silvestrini-Biavati et al. 2024: Ugolini et al. 2025). It has been confirmed that these two expanders produce comparable skeletal and dental effects in subjects (Lanteri et al. 2021; Inchingolo et al. 2023).

Similar to the SME protocol, the leaf expander is an innovative device characterized by a double nickel-titanium leaf spring, in addition to a midline jack screw. The screw is pre-activated in the laboratory, and the orthodontist can activate the leaf springs by compressing them, generating a constant force of either 450 g or 900 g. The primary benefits of using this device are its ease of activation and the fact that it does not require patient cooperation during the expansion process (Salgueiro et al. 2015; Inchingolo et al. 2023). Previous studies have evaluated the effects of 6 mm and 10 mm expander op-

tions in patients with mixed and permanent dentition (Lanteri et al. 2016; Manzella et al. 2018).

Finite element analysis (FEA) is a well-established method for structural simulation and mechanical analysis, widely applied in research on maxillary expansion (Lee et al. 2017). By substituting complex structures with a finite number of elements having simple geometric shapes, FEA plays a crucial role in the field of medical biomechanics (Pan et al. 2024; Shetty et al. 2009). To date, the evaluation of Ni-Ti Memoria Leaf Spring Activated Expander arm modifications has been limited to a single in vitro study (Lowe et al. 2020).

However, there is still a lack of comprehensive research examining the various material properties and mechanical modifications of the slow maxillary expander, particularly those involving the leaf-shaped elements. The objective of this study was to evaluate the deformation of the slow expander and the forces transmitted to the teeth as a result of applying different configurations to the slow maxillary expander screw arms, using FEA.

2. Materials and Method

2.1. Geometric details and material properties

The present study encompasses three distinct maxillary expander geometries. Given that all other components remain identical, the expander forms an angle of 0° , 15° and 30° relative to the teeth in each configuration, respectively. The designed expander geometries are illustrated in Fig. 1.

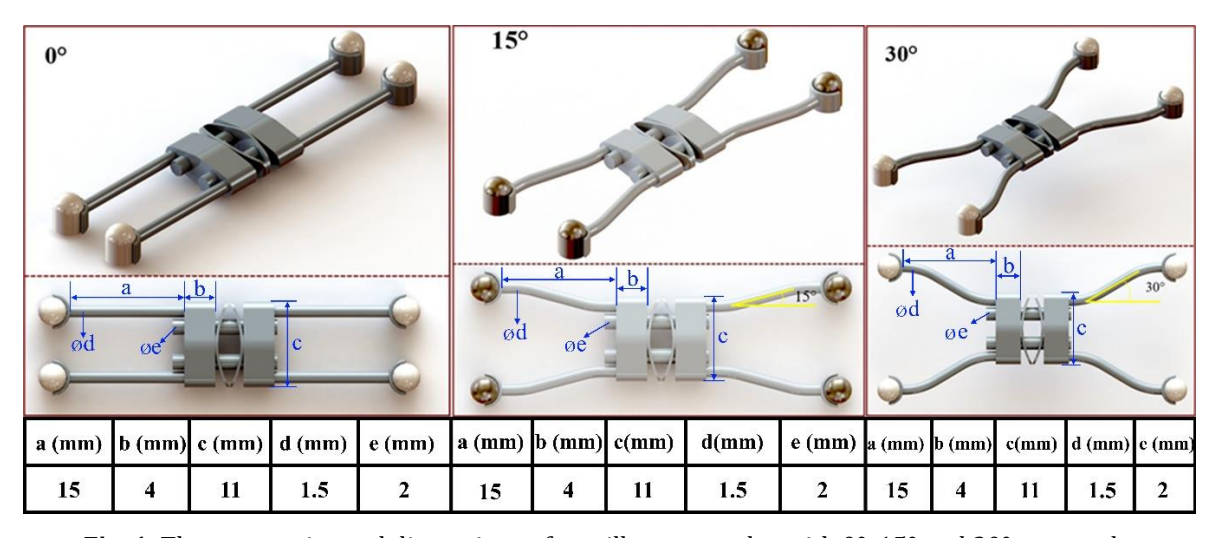


Fig. 1. The geometries and dimensions of maxillary expander with 0°, 15° and 30° arm angle.

The materials that were considered for use in the maxillary expander included the Ti6Al4V alloy, 316-L stainless steel and CoCr alloy. The mechanical properties of these materials are outlined in Table 1.

2.2. Finite element model

Numerical studies were conducted utilizing ANSYS Workbench, a commercial finite element software. Given that the stresses are not expected to exceed the yield stress,

Table 1. Material properties used in finite element analysis (Karslı et al. 2024; Karaman et al. 2022).

Mat	erial	Young's modulus (GPa)	Poisson's ratio
Ti6	Al4V	113.8	0.34
31	6-L	193	0.25
Co	Cr	213	0.28
То	oth	19.6	0.3

and the loadings are minimal, the analyses were performed employing a linear-elastic material model. Fig. 2 illustrates the mesh structure for each configuration. For all components of the expander, an element size of 0.15 mm was selected, taking into account the mesh dependency. A mesh convergence analysis was conducted on three distinct element sizes (0.10, 0.15 and 0.20 mm). Following the implementation of the 0.15 mm element size, no substantial alterations were observed in the results or mesh metrics. Consequently, 0.15 mm was selected as the optimal element size. The mesh metrics are presented in Table 2.

The boundary conditions are illustrated in Fig. 3. Due to the computational expense, the two leaf springs located at the center of the expander (Fig. 1) were excluded from the finite element model, with the forces generated by the springs being incorporated directly into the finite element model. The expander sliding on the pins exerts three different forces of 2.943 N, 5.886 N and 8.829 N in both directions in the *x*-axis, respectively, on the teeth fixed from the bottom surface. Three different expander arm angles, three different material types and three different loading magnitudes were taken into consideration in this study and a total of 27 FEA were

performed to obtain the equivalent stresses and deformations in *x*-direction. The analysis parameters are given in Table 3.

Table 2. Mesh metric values for all finite element analysis configurations.

Configuration	Number of elements	Number of nodes	Element quality
0°	250,279	1,067,591	0.870±0.11
15°	169,140	733,522	0.879±0.12
30°	194,590	832,970	0.860±0.12

Table 3. Finite element analysis parameters for maxillary expander.

	Parameters	
Arm Angle	Material	Load (N)
0°	Ti6Al4V	2.943
15°	316-L	5.886
30°	CoCr	8.829

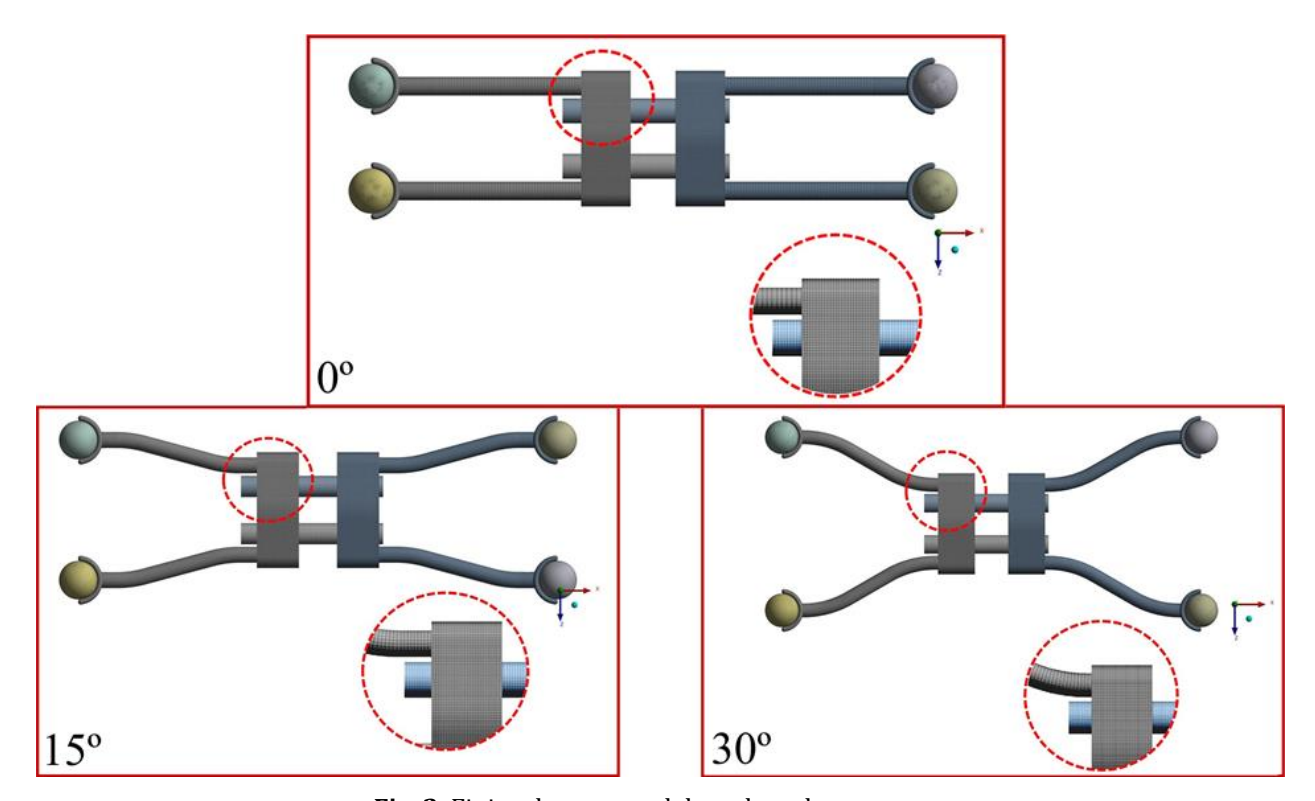


Fig. 2. Finite element models and mesh structures.

2.3. ANOVA analysis

In order to ascertain the effect of arm angle, material and load on equivalent stress and deformation in the x-direction, an analysis of variance (ANOVA) test was performed using Minitab software. A parameter was deemed to be statistically significant if p < 0.05. The effect of each parameter was explained with graphs showing the S/N ratios obtained. In this statement, the signal value (S) is

the value to be measured, and the noise value (N) is the effectiveness of the undesired factors within the measured value. The graphs of the calculated S/N ratios represent the degree of influence of any variable parameter used in the analysis. In addition to the S/N ratio, ANOVA analysis was used to determine the significance levels of variable parameters affecting the mechanical properties of the structures. This analysis was performed with Minitab software (Ghahramanzadeh Asl et al. 2023).

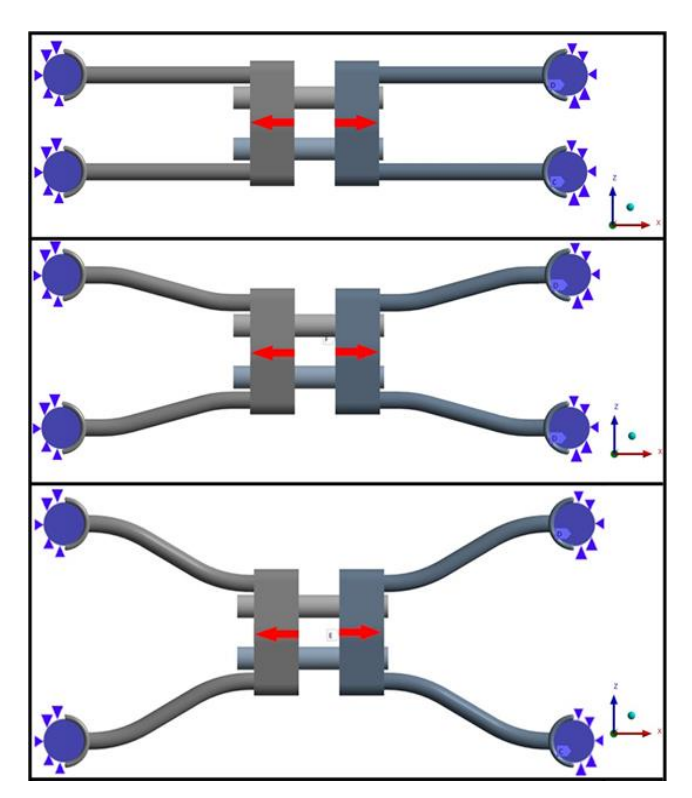


Fig. 3. Boundary conditions of models.

3. Result and Discussion

3.1. Finite element analysis results

As illustrated in Figs. 4–6, the FEA of the expanders with arm angles of 0° , 15° and 30° reveals the equivalent stress and deformation results in the *x*-direction.

The maximum equivalent stress and maximum deformation in the *x*-direction results obtained from all configurations are presented comparatively in Figs. 7 and 8, respectively.

When the equivalent stresses were analyzed, the situation was reversed. In each configuration, the stress reached a maximum at the screw arms, while it was significantly lower at the center and at the endpoints in contact with the threads. The only difference between the configurations is related to the stress distribution in the arms. In the expander with an arm angle of 0° , a more homogeneous stress distribution was observed due to the linear arm geometry. In contrast, in the expanders with arm angles of 15° and 30° , stress concentration occurred in the curved regions due to the geometry of the arms. However, since the maximum equivalent stress obtained (19.233 MPa) is nowhere near the yield stress for all three expander materials, there is no cause for concern

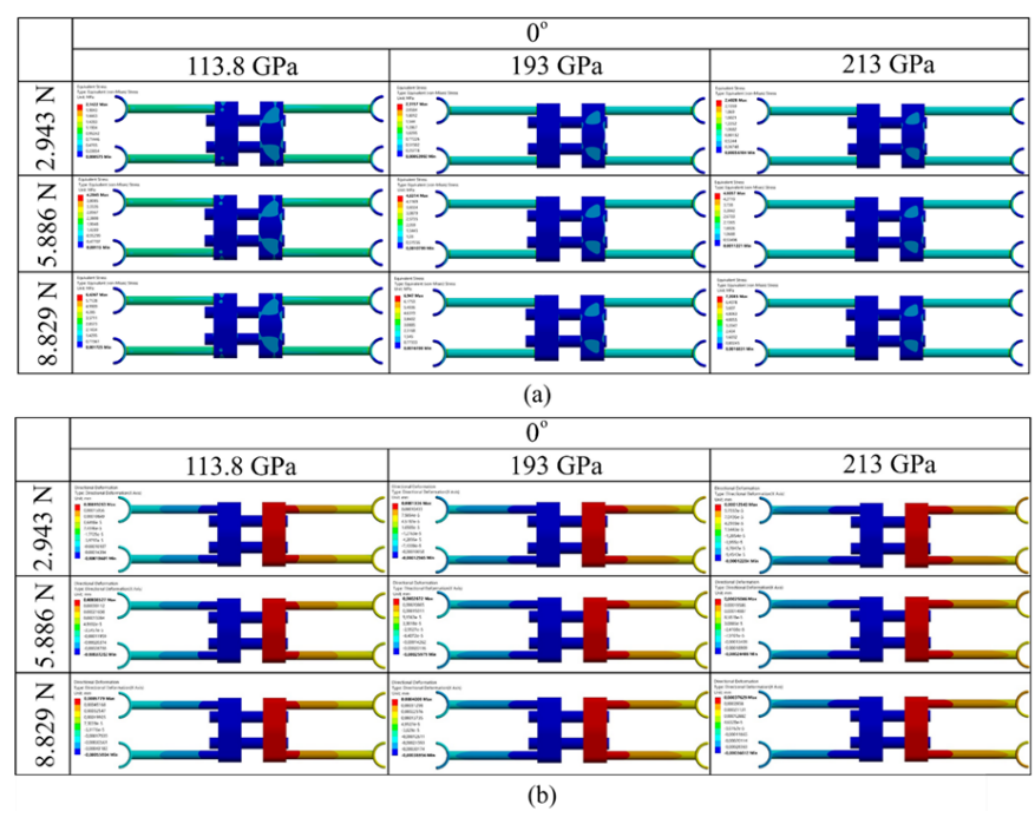


Fig. 4. Finite element analysis results for 0-degree arm angle: (a) Equivalent stress distribution; (b) Directional deformation along *x*-direction.

It can be posited that the maximum and minimum deformation in the *x*-direction are nearly equivalent for all three configurations, with deformation concentrated at the center of the expander. This observation is consistent with the anticipated outcomes, given the lo-

cation where the force was applied to the expander in both directions (Fig. 3). However, for expanders with arm angles of 15° and 30° , an increase in deformation was observed at the ends of the areas in contact with the teeth.

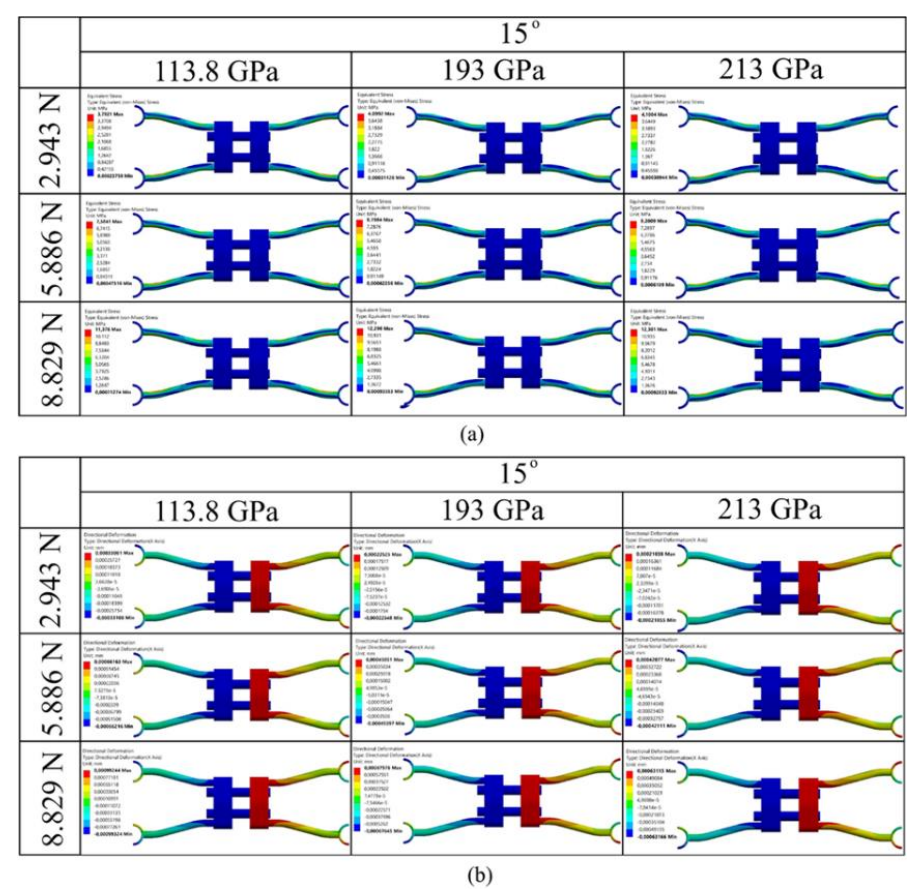


Fig. 5. Finite element analysis results for 15-degree arm angle: (a) Equivalent stress distribution; (b) Directional deformation along *x*-direction.

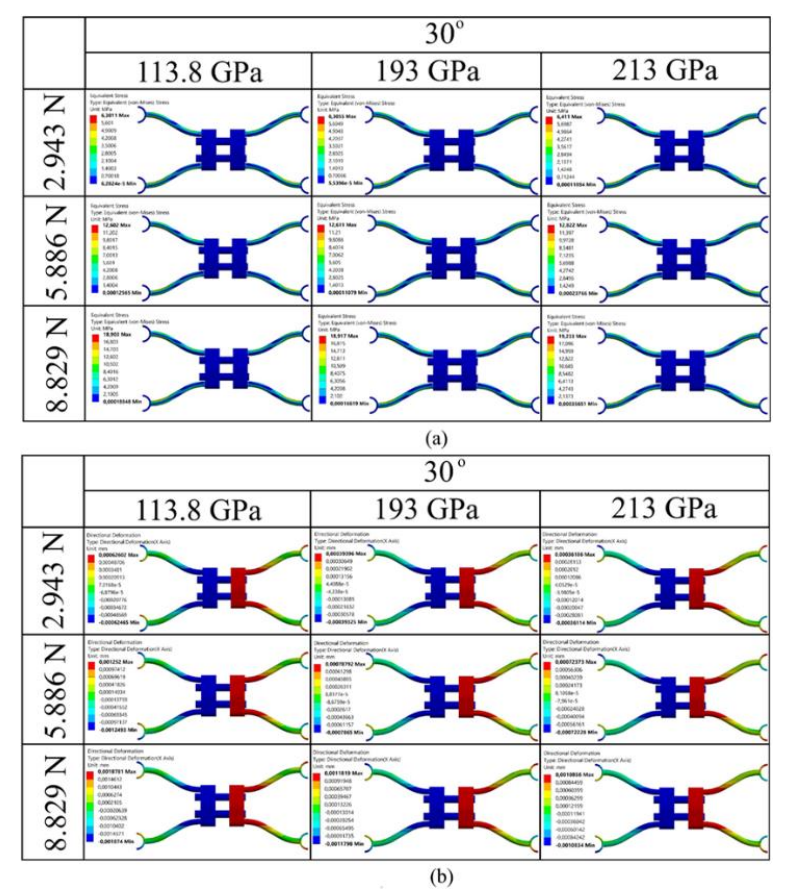


Fig. 6. Finite element analysis results for 30-degree arm angle: (a) Equivalent stress distribution; (b) Directional deformation along *x*-direction.

When the configurations for each angle value were evaluated individually, it was observed that the maximum equivalent stress increased as the rigidity of the material used for the expander increased. Conversely, as predicted, expander deformation decreased with increasing elastic modulus. In accordance with the linear-elastic analysis, it was observed that as the applied force increased, the maximum equivalent stress also increased at the same rate. This increase was reflected in

the maximum deformation as well. A noteworthy observation is the impact of the expander arm angle on both maximum stress and deformation.

It is evident that as the arm angle increases, both the maximum stress and deformation also increase, indicating a dependence on arm geometry. It is also important to note that as the expander screw arm angle increases, the curvature increases, leading to higher stress concentrations.

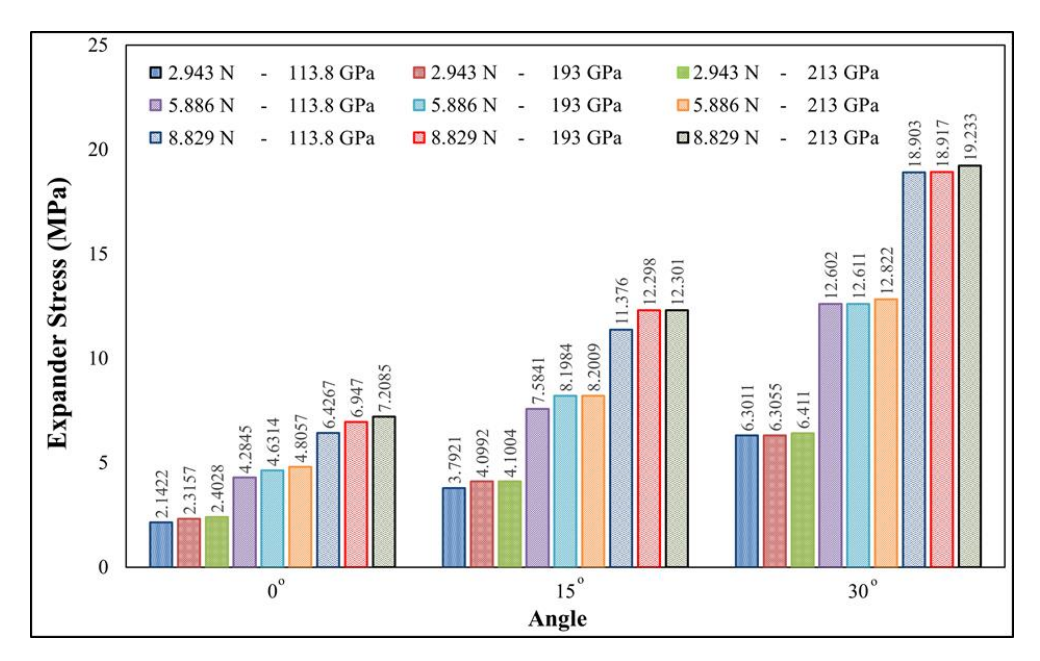


Fig. 7. Comparative maximum equivalent stress results for all configurations.

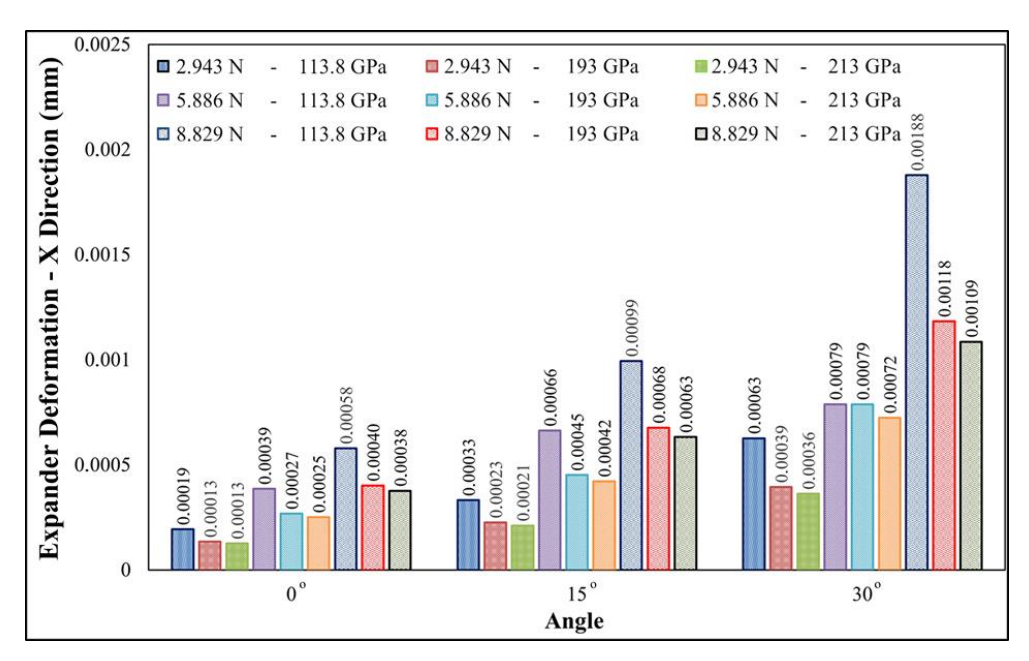


Fig. 8. Comparative maximum deformation results of expander along x-direction for all configurations.

The effect of the expander on the displacement of the tooth in the *x*-direction is comparatively given in Fig. 9 for all configurations. When Fig. 9 was analyzed, it was observed that the primary factor influencing tooth displacement was the force applied to the expander, while material type and arm angle had no significant effect.

However, it would be erroneous to interpret tooth displacement in this manner. In actual practice, the expander remains in the upper jaw for extended periods, exerting continuous force. This temporal aspect is not feasible to incorporate within finite element analysis. Consequently, the tooth deformation depicted in Fig. 9

represents instantaneous deformations corresponding to the force application, without accounting for the duration of force application.

Additionally, the fixed position of the teeth from below, as illustrated in Fig. 3, contributes to this phenomenon. Consequently, the most efficacious method of inter-

preting the deformation occurring in the tooth/jaw by finite element analysis is to interpret the results through the expander. Furthermore, measuring the reaction forces between the expander and the tooth can also provide some insight, and the relevant results are given in Fig. 10.

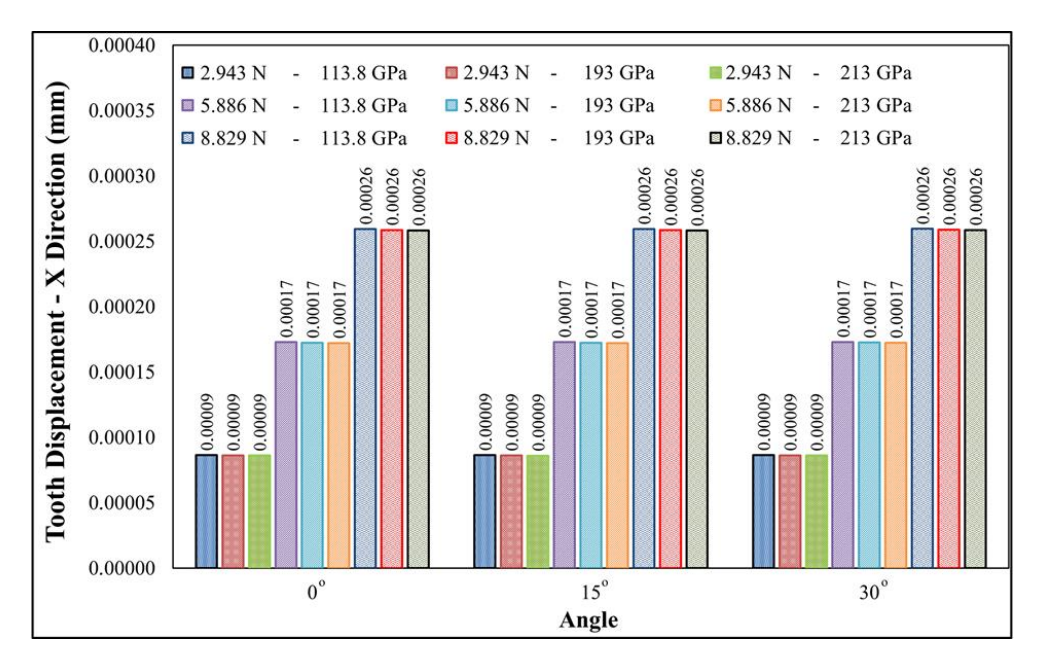


Fig. 9. Comparative maximum deformation results of tooth along *x*-direction for all configurations.

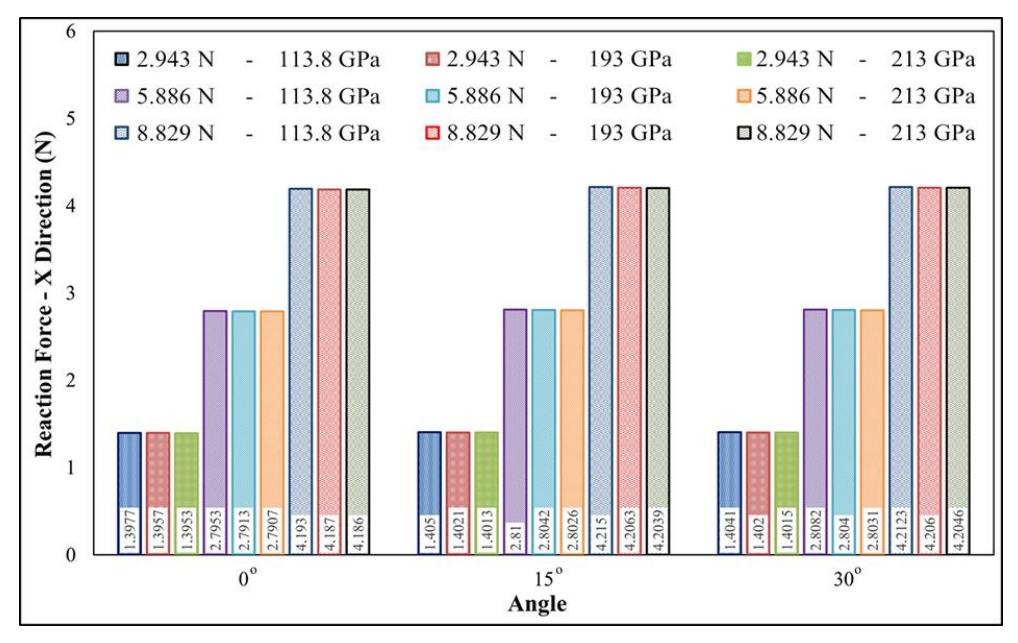


Fig. 10. Comparative maximum reaction force results along *x*-direction for all configurations.

As demonstrated in Fig. 10, a comparative analysis of the reaction forces in the *x*-direction is provided for all configurations. In accordance with the predictions, the reaction force increases in proportion to the applied force to the expander. However, the effect of material properties and arm angle is not significant, as discussed in the preceding section. However, a detailed analysis of Fig. 10 reveals that as the elastic modulus of the preferred material increases for the expander with each arm

angle, the reaction force in the *x*-direction decreases, albeit in small amounts. This is an important sign that tooth deformation increases as the elastic modulus increases.

Similarly, when the arm angle is 15° , there is an increase in the reaction force compared to 0° . However, no significant disparities were identified between configurations with an arm angle of 30° and those with an arm angle of 15° .

3.2. ANOVA results

The results obtained from the analysis of variance (ANOVA) test using the maximum expander deformations in the *x*-direction obtained from the FEA are presented in Fig. 11. According to this, the most effective parameter is the force applied to the expander with a rate of 46%, followed by the arm angle with a rate of 44%, while the effect of material type is 10%. The most

significant conclusion that can be drawn from these findings is that the arm angle is as important as the force applied to the expander. In situations where the force that can be applied is limited by various factors have been examined. As a result of the examination, it can be demonstrated that altering the arm angle can lead to the achievement of the desired outcome. This suggests that by modifying the arm angle, it is possible to achieve superior results by applying a lesser amount of force.

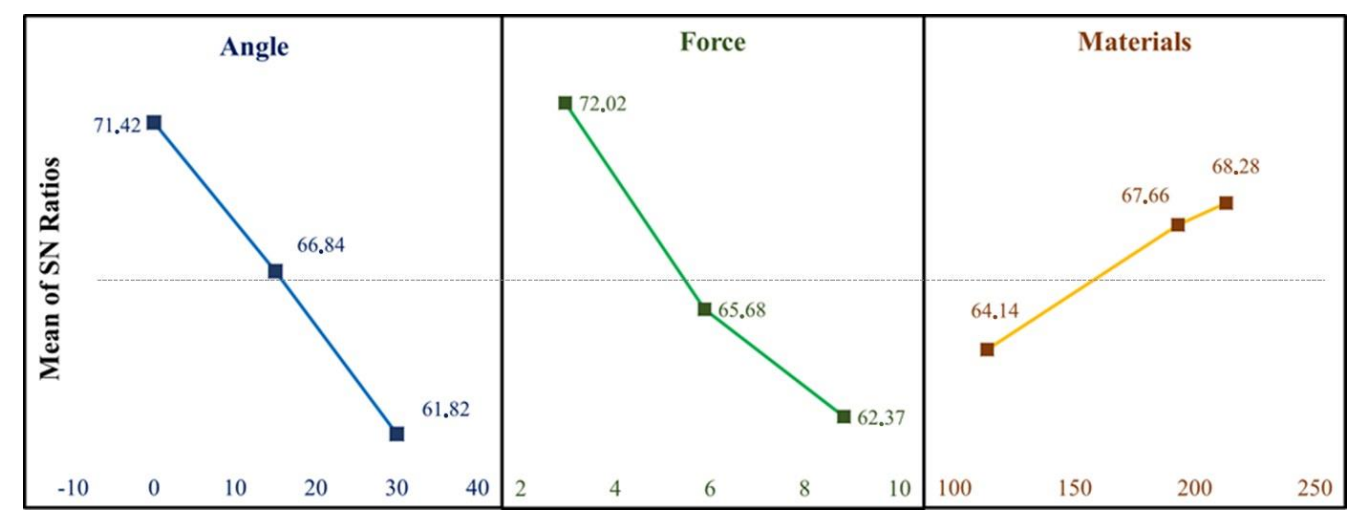


Fig. 11. ANOVA test results based on maximum deformation of expander along *x*-direction.

4. Conclusions

This study aims to evaluate the deformation of the slow expander, and the forces transmitted to the teeth. Three different expander arm angles (0°, 15° and 30°), three different material types (Ti6Al4V, 316-L and CoCr alloy) and three different loading magnitudes (2.943 N, 5.886 N and 8.829 N) were considered. In addition, total of 27 finite element analyses were performed. Based on the results obtained, the following conclusions were reached:

- An increase in the arm angle of the expander led to greater deformation within the tooth contact areas.
- A more homogeneous stress distribution was achieved in the expander with a screw arm angle of 0 degrees; however, stress concentrations were observed in the curved regions as the screw arm angle increased.
- In all screw angle configurations, an increase in the Young's modulus of the expander material resulted in greater deformation of the expander.
- The results of the ANOVA analysis indicated that the screw arm angle is as significant as the force applied by the expander. In situations where sufficient force cannot be applied due to various constraints, better results may be achieved by adjusting the screw angle
- The applied force was found to have a more significant impact on expander deformation compared to the other variables.
- In cases where a high force is applied to the leaf expander, it is crucial to consider the potential deformations that may occur.

Acknowledgements

None declared.

Funding

The authors received no financial support for the research, authorship, and/or publication of this manuscript.

Conflict of Interest

The authors declared no potential conflicts of interest with respect to the research, authorship, and/or publication of this manuscript.

Author Contributions

All of the authors made substantial contributions to conception and design, or acquisition of data, or analysis and interpretation of data; were involved in drafting the manuscript or revising it critically for important intellectual content; and gave final approval of the version to be published.

Data Availability

The datasets created and/or analyzed during the current study are not publicly available, but are available from the corresponding author upon reasonable request.

REFERENCES

Alsawaf DH, Almaasarani SG, Hajeer MY, Rajeh N (2022). The effectiveness of the early orthodontic correction of functional unilateral posterior crossbite in the mixed dentition period: A systematic review and meta-analysis. *Progress in Orthodontics*, 23(1), 5.

Arndt WV (1993). Nickel titanium palatal expander. *Journal of Clinical Orthodontics*, 27, 129-137.

Da Silva Filho OG, Santamaria MJr, Filho LC (2007). Epidemiology of posterior crossbite in the primary dentition. *Journal of Clinical Pediatric Dentistry*, 32, 73-78.

- Ghahramanzadeh Asl H, Altıntaş Kahriman E, Karaman D (2023). Numerical investigation of the effective mechanical properties of Octet Truss lattice structures with different strut geometry. *Challenge Journal of Structural Mechanics*, 9(4), 133-144.
- Gianolio A, Lanteri C, Lanteri V, Cherchi C (2015). A new device for calibrated maxillary expansion: The Ni-Ti Memoria® leaf spring activated expander. *Leone America's Ortho News*, I, 1-10.
- Haas AJ (1970). Palatal expansion: Just the beginning of dentofacial orthopedics. *American Journal of Orthodontics*, 57, 219-255.
- Inchingolo AM, Patano A, De Santis M, Del Vecchio G, Ferrante L, Morolla R, Pezzolla C, Sardano R, Dongiovanni L, Inchingolo F (2023). Comparison of different types of palatal expanders: Scoping review. *Children*, 10(7), 1258.
- Isaacson RJ, Ingram AH (1964). Forces produced by rapid maxillary expansion: II. Forces present during treatment. The Angle Orthodontist, 34, 261-270.
- Karaman D, Ghahramanzadeh Asl H, Altıntaş Kahriman E (2022). Estimation and comparison of effective elastic modulus of different scaffolds using curve fitting method for additive manufacturing field. Arabian Journal for Science and Engineering, 47, 15973-15987.
- Karslı N, Yıldırım F, Dingiloğlu A, Polat Özsoy Ö (2024). Does the trimline extension and attachment size affect maxillary arch expansion in clear aligner therapy? A finite element study. Australasian Orthodontic Journal, 40, 121-133.
- Kutin G, Hawes RR (1969). Posterior cross-bites in the deciduous and mixed dentitions. American Journal of Orthodontics, 56, 491-504.
- Lanteri C, Beretta M, Lanteri V, Gianolio A, Cherchi C, Franchi L (2016). The leaf expander for non-compliance treatment in the mixed dentition. *Journal of Clinical Orthodontics*, 50, 552-560.
- Lanteri V, Abate A, Cavagnetto D, Ugolini A, Gaffuri F, Gianolio A, Maspero C (2021). Cephalometric changes following maxillary expansion with Ni-Ti leaf springs palatal expander and rapid maxillary expander: A retrospective study. Applied Sciences, 11(12), 5748.
- Lee RJ, Moon W, Hong C (2017). Effects of monocortical and bicortical mini-implant anchorage on bone-borne palatal expansion using finite element analysis. *American Journal of Orthodontics and Dentofacial Orthopedics*, 151(5), 887-897.
- Leonardi R, Lo Giudice A, Rugeri M, Muraglie S, Cordasco G, Barbato E (2018). Three-dimensional evaluation on digital casts of maxillary palatal size and morphology in patients with functional posterior crossbite. *European Journal of Orthodontics*, 40, 556-562.
- Lowe R, Makowka S, Manzella K, Warunek S, Al-Jewair T (2020). Mechanical properties of the NiTi Memoria leaf spring activated ex-

- pander (NiTi MLSAE) for maxillary transverse discrepancy correction: An in-vitro study. *Journal of Clinical and Experimental Dentistry*, 12, e154-e160.
- Manzella K, Franchi L, Al-Jewair T (2018). Correction of maxillary transverse deficiency in growing patients with permanent dentitions. *Journal of Clinical Orthodontics*, 52, 148-156.
- McAndrew J (1985). The continuous force control system. Lancer Technical Report, Lancer Pacific, Carlsbad, CA, USA.
- Pan Y, Peng W, Wang Y (2024). Comparison of the effects of different palatal morphology on maxillary expansion via RME and MSE: A finite element analysis. *Clinical and Experimental Dental Research*, 10(5), e70005.
- Salgueiro DG, De O Rodrigues VHL, Tieghi V, De Menezes CC, Gonçales ES, Ferreira O (2015). Evaluation of opening pattern and bone neoformation at median palatal suture area in patients submitted to surgically assisted rapid maxillary expansion (SARME) through cone beam computed tomography. *Journal of Applied Oral Science*, 23. 397-404.
- Shetty P, Hegde AM, Rai K (2009). Study of stress distribution and displacement of the maxillary complex following application of forces using jackscrew and nitanium palatal expander 2: A finite element study. *Journal of Clinical Pediatric Dentistry*, 34, 87-93.
- Silveira GS, Abreu LG, Palomo JM, da Matta Cid Pinto LS, de Sousa AA, Gribel BF, Oliveira DD (2021). Mini Hyrax vs Hyrax expanders in the rapid palatal expansion in adolescents with posterior crossbite: A randomized controlled clinical trial. *Progress in Orthodontics*, 22(1), 30.
- Silvestrini-Biavati F, Oliva G, Ghislanzoni LH, Ottonelli E, Dalessandri D, Lanteri V, Ugolini A (2024). Evaluation of palate morphology in patients treated with leaf expander and hyrax expander: A geometric morphometric analysis. Orthodontics & Craniofacial Research, 27(6), 959-966.
- Tsanidis N, Antonarakis GS, Kiliaridis S (2016). Functional changes after early treatment of unilateral posterior cross-bite associated with mandibular shift: A systematic review. *Journal of Oral Rehabilitation*, 43, 59-68.
- Ugolini A, Bruni A, Abate A, Pistoni F, Donelli M, Quinzi V, Lanteri V (2025). Effects on palatal surface area in mixed dentition patients treated with leaf expander and rapid palatal expander, compared to untreated subjects: A randomised clinical trial. *European Journal of Paediatric Dentistry*, 26(1), 48-54.
- Wichelhaus A, Geserick M, Ball J (2004). A new nickel titanium rapid maxillary expansion screw. *Journal of Clinical Orthodontics*, 38, 677-680.



Research Article

Influence of damage state threshold variability on the seismic vulnerability analysis of masonry aqueducts

Ali Yesilyurt a,* (D)

^a Department of Earthquake Engineering, Disaster Management Institute, İstanbul Technical University, 34469 İstanbul, Türkiye

ABSTRACT

The accuracy of fragility curves, a key outcome of seismic vulnerability studies, directly influences rational seismic risk assessments. In this study, analytical-based fragility curves for a masonry aqueduct were derived using tested earthquake-based Intensity Measure (IM) parameters and various threshold limit values for specific damage states, as commonly used in the literature. The Maximum Intensity Damage Ratio (MIDR) thresholds for specific damage states proposed by FEMA 356, GERMHS, and ASCE 41-13 standards were considered. Additionally, damage state thresholds were determined through a capacity curve obtained via nonlinear static analysis and empirical relationships found in the literature. The effect of damage thresholds on the Probability of Exceedance (PoE) values for a specific damage state was analyzed using the reference MIDR values determined in this study. Based on earthquake ground motion records, PoE values corresponding to different damage states were evaluated separately for each IM parameter. The results demonstrate that the damage threshold value significantly impacts the developed fragility curves. Therefore, when developing fragility curves for the seismic risk assessment of masonry structures, it is crucial to analyze and determine the appropriate threshold levels for each structure individually, rather than directly applying the threshold values used in the literature.

ARTICLE INFO

Article history:

Received – May 2, 2025 Revision requested – June 2, 2025 Revision received – June 10, 2025 Accepted – June 20, 2025

Keywords:

Masonry aqueduct Intensity measure Cloud Analysis Drift ratio Fragility curve



This is an open access article distributed under the CC BY licence. © 2025 by the Author.

Citation: Yesilyurt A (2025). Influence of damage state threshold variability on the seismic vulnerability analysis of masonry aqueducts. *Challenge Journal of Structural Mechanics*, 11(3), 137–148.

1. Introduction

Aqueducts are significant engineering structures built to transport water from natural sources to settlements by crossing valleys, rivers, and various natural or artificial obstacles. These structures, tangible examples of the masonry design approach that developed particularly from ancient times onward, reflect past civilizations' technical knowledge and aesthetic sensibilities. Numerous surviving masonry aqueducts draw attention today not only for their historical significance but also for their architectural and cultural heritage value (Balcan et al. 2024). Although modern infrastructure systems are widely used today and contemporary water conveyance structures are being constructed, numerous aqueducts

belonging to different cultures remain standing within the borders of present-day Türkiye (Fig. 1).

Despite having lost their original function, these structures are preserved as significant elements of cultural heritage due to their architectural characteristics and historical value (Gonen et al. 2021). Preserving these engineering marvels and passing them on to future generations is of great importance. However, there are relatively few comprehensive studies that assess the seismic vulnerability and risk of such historic structures (Dogangun and Sezen 2012). In general, historic masonry aqueducts are classified into sub-categories based on their construction techniques, material properties, and geometric configurations. Seismic vulnerability and risk assessments are conducted for each subcategory

separately (Çakır 2021; Ercan et al. 2015). Seismic vulnerability and risk assessment studies are of crucial importance, with the objective being the quantification of potential damage and losses caused by earthquakes. The capacity to predict accurately the losses that a given type of structure may encounter post-earthquake is a critical reference, as it enables the effective planning of both pre-earthquake preparedness and post-earthquake action and rehabilitation processes (Cattari et al. 2022; Yücemen and Yılmaz 2015; Işık et al. 2020). Fragility curves are a valuable tool that provides the probability of exceeding (PoE) a particular damage state for a given

seismic intensity measure parameter value. A review of the existing literature shows that fragility curves are extensively utilized in seismic risk analysis (Yesilyurt et al. 2024; Rota et al. 2010; Yesilyurt et al. 2021a). It is known that the extant literature on seismic risk studies of historical masonry structures is more limited compared to traditional residential buildings, industrial structures, and steel constructions (Gkournelos et al. 2022; Alpaslan and Karaca 2020; Lagomarsino and Cattari 2015). Moreover, the scarcity of literature addressing the seismic fragility functions specific to masonry aqueducts is particularly pronounced.

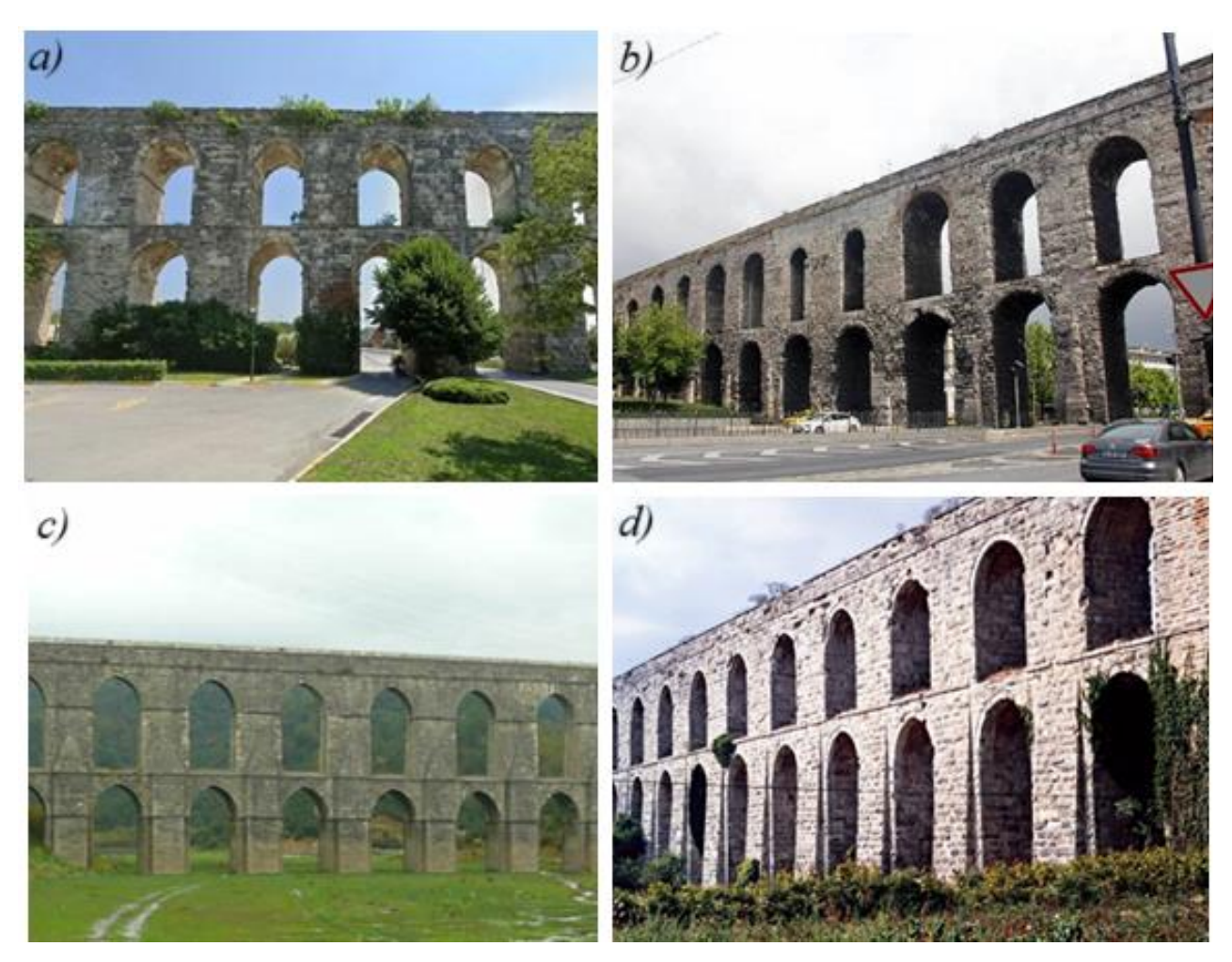


Fig. 1. Examples of masonry aqueducts located in Türkiye: a) Uzun Aqueduct; b) Bozdogan (Valens) Aqueduct; c) Güzelce Aqueduct; d) Kırkçeşme Aqueduct.

Du et al. (2023) derived fragility curves based on peak ground acceleration (*PGA*) for a sample aqueduct in south-west China. The effects of both mainshock and aftershock ground motion sequences were considered. The Incremental Dynamic Analysis (IDA) method was applied. The impact of aftershocks on seismic risk was examined through the fragility surface. Liu et al. (2025) conducted a seismic vulnerability analysis of a threespan simply supported aqueduct in China. The probability of damage under seismic loading was analyzed through the implementation of probability density functions. In the study by Zhang et al. (2022), the seismic response of high-span aqueduct structures was in-

vestigated under Near-Far field ground motions, with fragility curves developed as a function of *PGA*. A comparative assessment of *PoE* at specific intensity measure levels revealed that aqueduct structures are more vulnerable to damage under near-fault ground motions. In a similar study, Zheng et al. (2023) examined the effects of aftershocks on structural damage. The IDA method was employed, and seven main aftershock sequences were considered. Fragility curves were proposed for four different damage states as a function of *PGA*. For specific *PGA* values, the damage-increasing effect of aftershocks was assessed based on the exceedance probability.

Xu et al. (2021) developed fragility curves for a largescale aqueduct structure using IDA and the Multiple Stripe Analysis (MSA) method. The study considered four distinct damage states, and the fragility curves were derived as a function of spectral acceleration (Sa). Du et al. (2024a) presented fragility curves for a typical threespan aqueduct structure by considering both single and compound intensity measures. Moreover, the study provided quantitative recommendation values regarding record-to-record variability, design parameters, performance index values, and limit states. Yesilyurt (2025) proposed the earthquake and structure-based optimal intensity measure (IM) parameters for quantifying the seismic risk of a typical Roman masonry aqueduct. The study considered 29 IMs, and fragility curves were derived based on the identified optimal IMs and various damage parameters. Similarly, the suitability of IMs for modern aqueduct structures was examined through the utilization of near-field non-pulse, near-field pulse, and far-field sets of ground motion records. The influence of these ground motion sets on PoEs was also analyzed for the selected optimal IMs (Du et al. 2024b).

Ma et al. (2022) developed component-based fragility curves for a three-span aqueduct with an equidistant simply supported beam. The general product of conditional marginal method is performed. The study incorporated both structural and ground motion uncertainties to develop fragility curves. Similarly, Cheng et al. (2020) developed component-based fragility curves for a typical aqueduct structure.

In addition to the aforementioned studies, the maximum inter-story drift ratio (*MIDR*) is frequently utilized as a damage parameter in the risk assessment of historic masonry structures (Korkmaz et al. 2018; Vanin et al. 2017; FEMA 274 1997). Furthermore, various standards provide threshold values for different damage states based on the *MIDR* parameter. The primary objective of this study is to develop analytically based fragility curves for aqueduct structures using these predefined threshold values. Subsequently, the study aims to investigate the impact of these thresholds on seismic vulnerability assessment.

To this end, a finite element model of a typical masonry aqueduct was constructed. Response spectrum analyses were then performed using the cloud analysis method on a set of 479 ground motion records. The dispersion between the selected *IMs* and the *MIDR* damage parameter was obtained. Based on these intensity and damage measure relationships, fragility curves were derived separately for different thresholds. Furthermore, the *PoE* values corresponding to different damage states were comparatively analyzed for selected earthquake ground motion records.

2. Seismic Vulnerability Analysis

An examination of the seismic-tectonic setting of Türkiye reveals that the Arabian plate, located to the south, is moving northwards and colliding with the Eurasian plate, resulting in significant compression in the eastern Anatolian region. As a result of this plate interaction, the Anatolian plate is being pushed westward, mainly by the

North Anatolian Fault Zone (NAFZ) and the East Anatolian Fault Zone (EAFZ) (Erdik et al. 1985).

Among the major destructive earthquakes that have occurred in Türkiye over the past 30 years are the 17 August 1999 Mw 7.4 Kocaeli, 12 November 1999 Mw 7.2 Düzce, 3 February 2002 Mw 6.4 Afyon, 1 May 2003 Mw 6.4 Bingöl, 23 October 2011 Mw 7.2 Van, 24 January 2020 Elazığ, 30 October 2020 Mw 6.9 Samos (İzmir), and 23 November 2022 Mw 5.9 Düzce earthquakes. In the recent past, a sequence of earthquakes that struck on February 6, 2023, centered in Kahramanmaraş, caused unprecedented destruction and loss of life, marking one of the most powerful and impactful seismic events in Türkiye's history. The epicentres of the two destructive earthquakes were located in the districts of Pazarcık and Elbistan, with focal depths measured at 8.6 km and 7.0 km, respectively. The rupture occurred along the northern segment of the East Anatolian Fault and severely affected several provinces (AFAD 2023). Furthermore, numerous unique historic masonry structures were destroyed during these events (Kocaman 2023; Kocaman et al. 2024; Erkek and Yetkin 2023). Seismic vulnerability and risk analyses are vital studies in reducing casualties following earthquakes. The recurrence of similar loss of life and property after earthquakes has increased interest in such studies (Alparslan et al. 2017; Cosgun and Mangir 2018). In parallel with technological advancements, there has been an increase in the number of seismic vulnerability and risk analyses studies, which are becoming more comprehensive and effective.

In the context of seismic vulnerability and risk mitigation studies, the RADIUS project, HAZUS (Multi-hazard Loss Estimation Methodology), PBEE-PBEE methodology, DBLA (the Displacement-Based Loss Assessment), ESPREME, GEM (Global Earthquake Model), RADIUS (Risk Assessment Tools for Diagnosis of Urban Areas against Seismic Disasters), SHARE (Seismic Hazard Harmonization in Europe), the SESAME project, NGA (Next Generation Attenuation) project, LESSLOSS, RISK-UE, The World Bank's CAPRA, SYNER-G, and NERA projects provide insightful guidance. Fragility curves are widely preferred in risk assessment calculations because of the convenience they provide (Yılmaz et al. 2018). These curves can be developed using empirical, analytical, hybrid, and expert judgement methods (Yesilyurt et al. 2021b). In this study, the analytical method has been considered, and the main components can be outlined as follows: numerical modelling, Compilation of an Earthquake Ground Motion Set, definition of damage and intensity measure parameters, structural analysis, damage analysis, and statistical procedures.

2.1. Description of the modelling and non-linear static analysis

Three-dimensional finite element modeling (FEM) is widely recognized as a reliable and effective approach for the seismic performance assessment of historical masonry structures. In this study, the finite element model of the investigated segment of the masonry aqueduct was developed using ANSYS Workbench. A visual of the 3D structural model considered in the analysis is presented in Fig. 2.

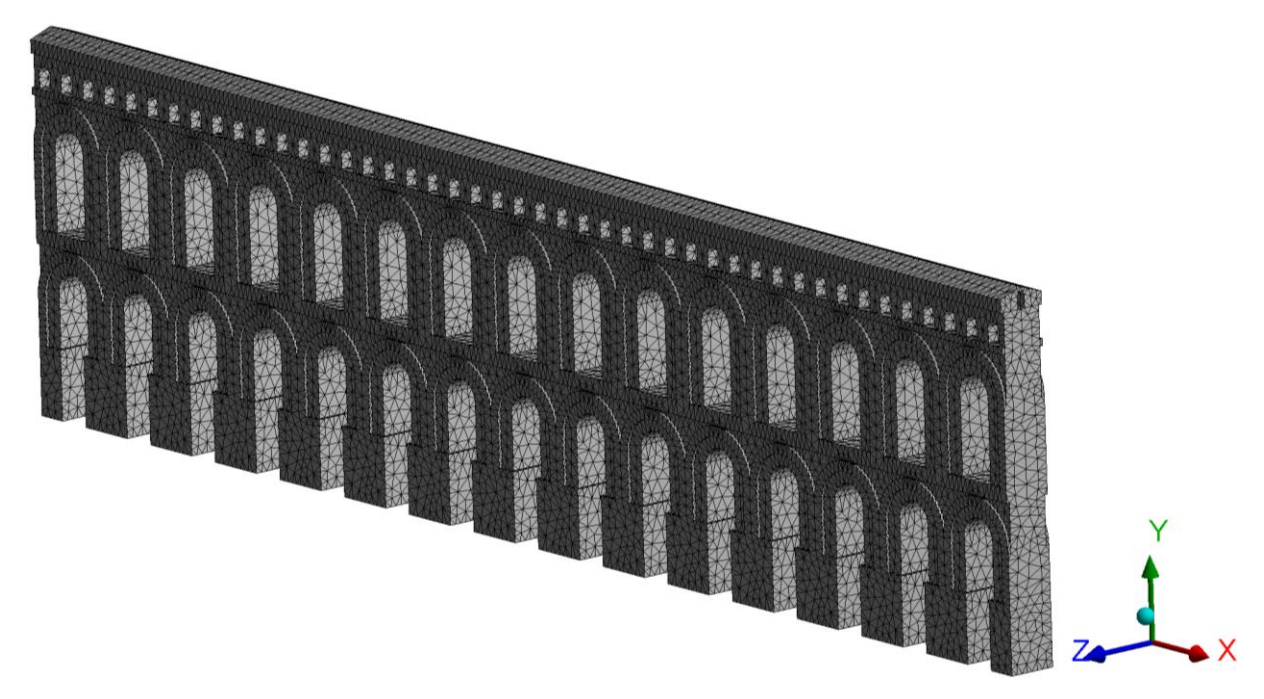


Fig. 2. Three-dimensional finite element model of the masonry aqueduct.

The 3D finite element model contained 261,619 nodes and 151,406 elements, utilizing a 20-node solid element with 3 degrees of freedom per node. Research on the most accurate modeling approaches for masonry structures continues to be a subject of advanced engineering studies. In this study, to improve computational efficiency in structural modeling, the aqueduct was treated as a homogeneous composite material, and the macro modeling approach was adopted, in which the masonry units and mortar are represented as a single equivalent material (Drougkas 2022). The aqueduct was modeled with fixed boundary conditions applied along its base and at its end supports. To accurately capture the nonlinear mechanical behavior of the masonry material, the Drucker-Prager yield criterion, which is considered suitable for materials with low tensile and high compressive strength, was employed (Drucker and Prager 1952).

As previously discussed, the primary objective of this study is to investigate the influence of different damage thresholds on the seismic vulnerability of the structure. The material properties used in the finite element modelling were determined based on previous studies in the literature and generally accepted engineering assumptions. The mechanical properties of the stone material considered were defined as Young's modulus 8729.6 MPa, Poisson's ratio 0.1238, bulk modulus 3.867×10⁹ Pa, and shear modulus 3.88×10⁹ Pa. In addition, the main parameters of the bilinear isotropic hardening model, yield strength and the tangent modulus, were considered as 3.2 MPa and 144 MPa, respectively.

A modal analysis was carried out to evaluate the seismic behavior and to examine the dynamic characteristics of the aqueduct. The first 30 vibration modes were considered to fully evaluate the dynamic response of the structure. This analysis identified the natural frequencies, periods, and mode shapes of the structure. The first six mode shapes and their corresponding frequency values are shown in Fig. 3.

In Fig. 3, the X, Y, and Z directions correspond to the in-plane, vertical, and out-of-plane directions of the structure, respectively, for the first six mode shapes. It is observed that the first mode of the aqueduct is in the out-of-plane (Z) direction, characterized by translational motion. This mode represents the most critical direction in the seismic performance of the structure. The out-of-plane response has been determined as a reference in the seismic vulnerability assessment. Therefore, in the subsequent cloud analysis, which will be detailed in the following sections, the structural response is primarily evaluated in the Z-direction, taking into account the out-of-plane behavior.

A non-linear static analysis was performed using an incremental-iterative procedure to evaluate the out-of-plane seismic performance of the structure based on the finite element model. The capacity curve calculated by the pushover analysis is shown in Fig. 4.

2.2. Definition of damage and intensity measure parameters

As previously stated, in seismic vulnerability studies, the Damage Measure (DM) parameter quantitatively defines the limit value of a specific damage state of a given structure. A review of studies conducted on masonry structures in the literature shows that the MIDR damage parameter is commonly utilized. Numerous studies, codes, and standards such as ASCE 41-13 (2013), FEMA 356 (2000), GERMHS (2017), have proposed threshold values corresponding to different damage states based on the MIDR damage parameter. When these studies are analyzed as a whole, it is observed that the thresholds proposed for a given damage state vary considerably. The objective of this study is to evaluate the influence of different threshold values on seismic vulnerability through fragility curves. In this context, initial damage (Damage Limitation) and expected partial collapse (Heavy Damage) have

been considered. The rationale behind this selection is related to the inherent characteristics of historic masonry structures, such as aqueducts, which exhibit limited nonlinear behavior and are prone to sudden brittle failure.

Furthermore, the yield and ultimate points on the capacity curve of the analyzed structure can be determined precisely. In this context, Table 1 presents the thresholds based on the MIDR parameter considered in this study.

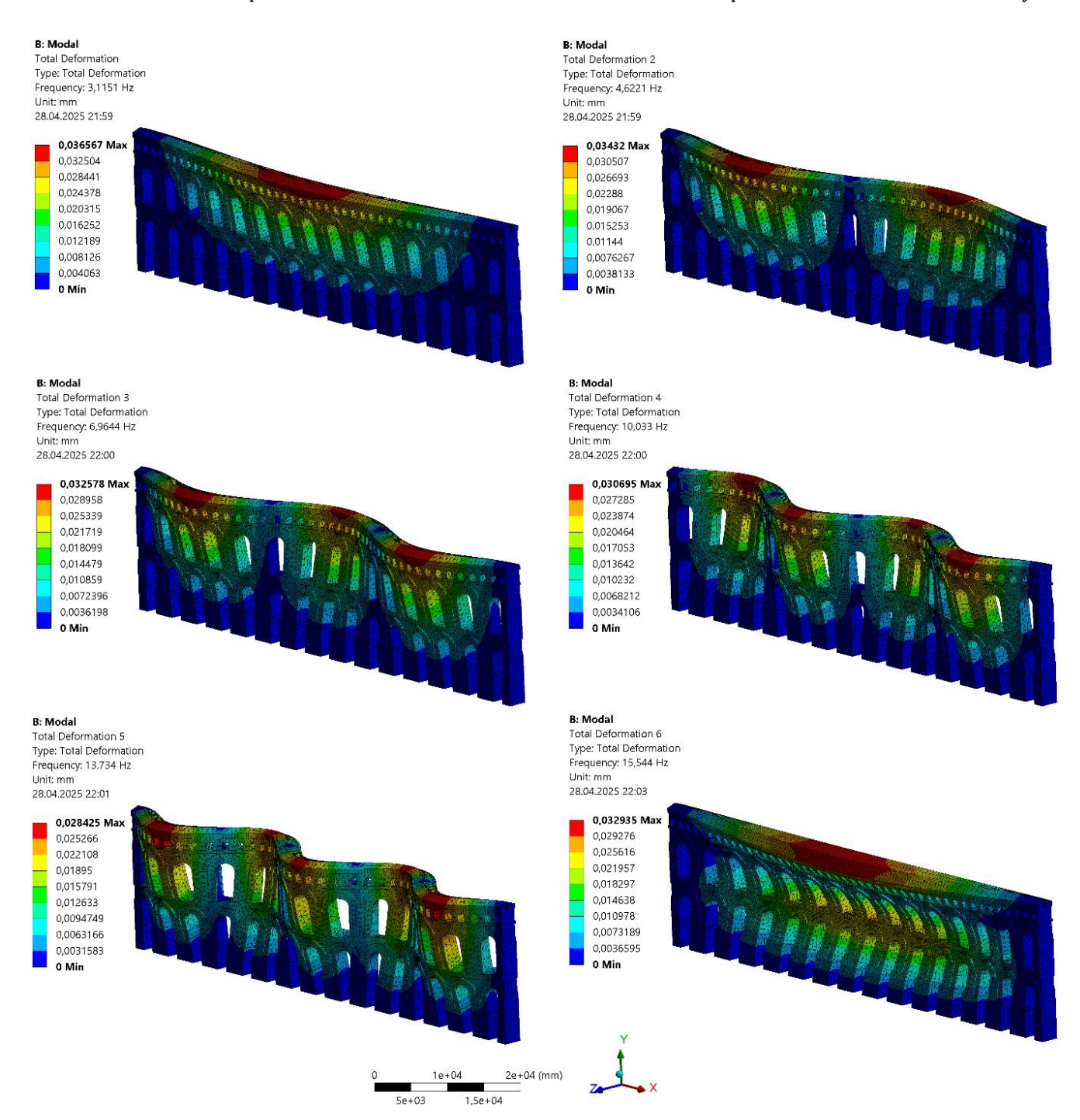


Fig. 3. The first six mode shapes and corresponding frequency values of the model.

Table 1. Various MIDR threshold values used as references for masonry structures.

Standards	Damage limitation (%)	Heavy damage (%)
FEMA 356 (2000)	0.10	0.40
GERMHS (2017)	0.30	0.70
ASCE 41-13 (2013)	0.10	0.75
Current study	0.18	0.53

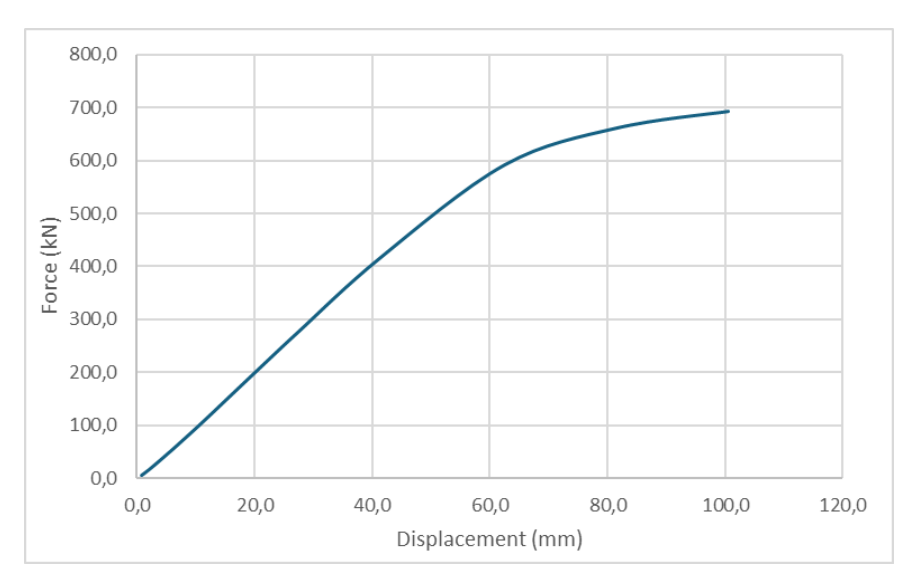


Fig. 4. Capacity curve of the aqueduct structure in the out-of-plane direction.

As can be seen in Table 1, in addition to the MIDR values presented in the existing standards, this study has provided different threshold values corresponding to structure-specific damage states. As demonstrated in numerous studies conducted by various researchers, the vield (dv) and ultimate (du) displacement values obtained from the capacity curve have been used as reference points to define different damage states (Lamego et al. 2017; Kappos et al. 2006; Vicente 2008; Lagomarsino and Giovinazzi 2006). In the relationship proposed by Kappos et al. (2006), 0.7 dy is suggested for Damage Limitation, while du is recommended for Heavy Damage. These threshold values have been calculated by utilizing the capacity curve depicted in Fig. 4 and the empirical relationships proposed by Kappos et al. (2006) as a reference.

The appropriateness of the IM parameters, which characterize ground motion and reflect the destructive potential of an earthquake, for a given class of structure directly impacts the accuracy of the derived fragility curves for that class. It is well known in the literature that the appropriate IMs vary depending on the structural typology. In this study, the earthquake-based IMs evaluated by Yesilyurt (2025) for their applicability in assessing the seismic vulnerability of aqueduct structures, namely Acceleration Spectrum Intensity (ASI), Arias Intensity (*Ia*), Characteristic Intensity (*Ic*), Sustained Maximum Acceleration (SMA), Effective Design Acceleration (EDA), and Peak Ground Acceleration (PGA) are considered. Accordingly, the analytically derived fragility curves are developed as functions of these IM parameters.

2.3. Seismic performance analysis method

The Cloud analysis method is particularly well-suited to vulnerability assessment of structures. In this method, the real unscaled ground motion records are utilized with a wide frequency range. This analysis approach can be adapted to various methodologies, including dynamic analysis, modal pushover analysis, and response spec-

trum analysis. The response spectrum analysis method is a widely employed technique in the relevant literature to evaluate the seismic performance and vulnerability of historical masonry structures. This is since it is both computationally efficient and practical (Akturk et al. 2025). The method has been employed in the analysis of finite element models of various masonry structures, including churches, mosques, arch bridges, and slender structures. The findings demonstrated a high level of consistency with post-earthquake field observations (Cakir et al. 2015; Ozdemir et al. 2017; Cakir et al. 2016; Cakir 2022).

In this study, the response spectrum method was adopted for performing structural analyses. In methods such as IDA, which involve a scaling process, the frequency content of the ground motion records remains unchanged. In contrast, the cloud analysis approach utilizes unscaled original ground motion records. This enables the consideration of a broader range of intensity and frequency characteristics, rather than being limited to the seismicity of a specific region.

The main challenge of this method lies in the necessity to include a large number of ground motion records to ensure that the selected set can adequately capture the overall structural response, ranging from slight damage to heavy damage. To this end, the ordinary earthquake ground motion record set was considered. This set incorporated near-far fault effects and all rupture mechanisms. A total of 479 real processed ground motion records were selected from the Pacific Earthquake Engineering Research Center (PEER) Ground Motion Database for the structural analysis of the aqueduct. The distribution of the sites where the selected ground motion records were recorded, along with the relationship between earthquake magnitude and source-to-site distance for the generated earthquake set, is presented in Fig. 5. Response spectrum analyses were performed on 479 real, unscaled earthquake records. The scatter plots illustrating the relationship between the IM parameters ASI, Ic, Ia, SMA, EDA, and PGA, as defined in the previous section, and the MIDR damage parameter are shown in Fig. 6.

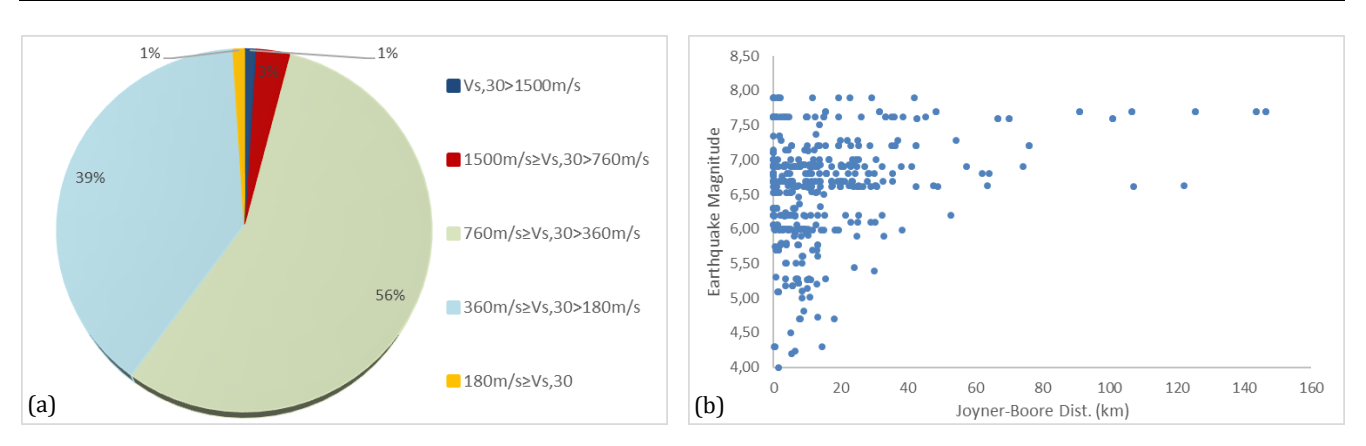


Fig. 5. Earthquake ground motion records: a) Site information at the locations of the stations; b) Magnitude-Distance relationship.

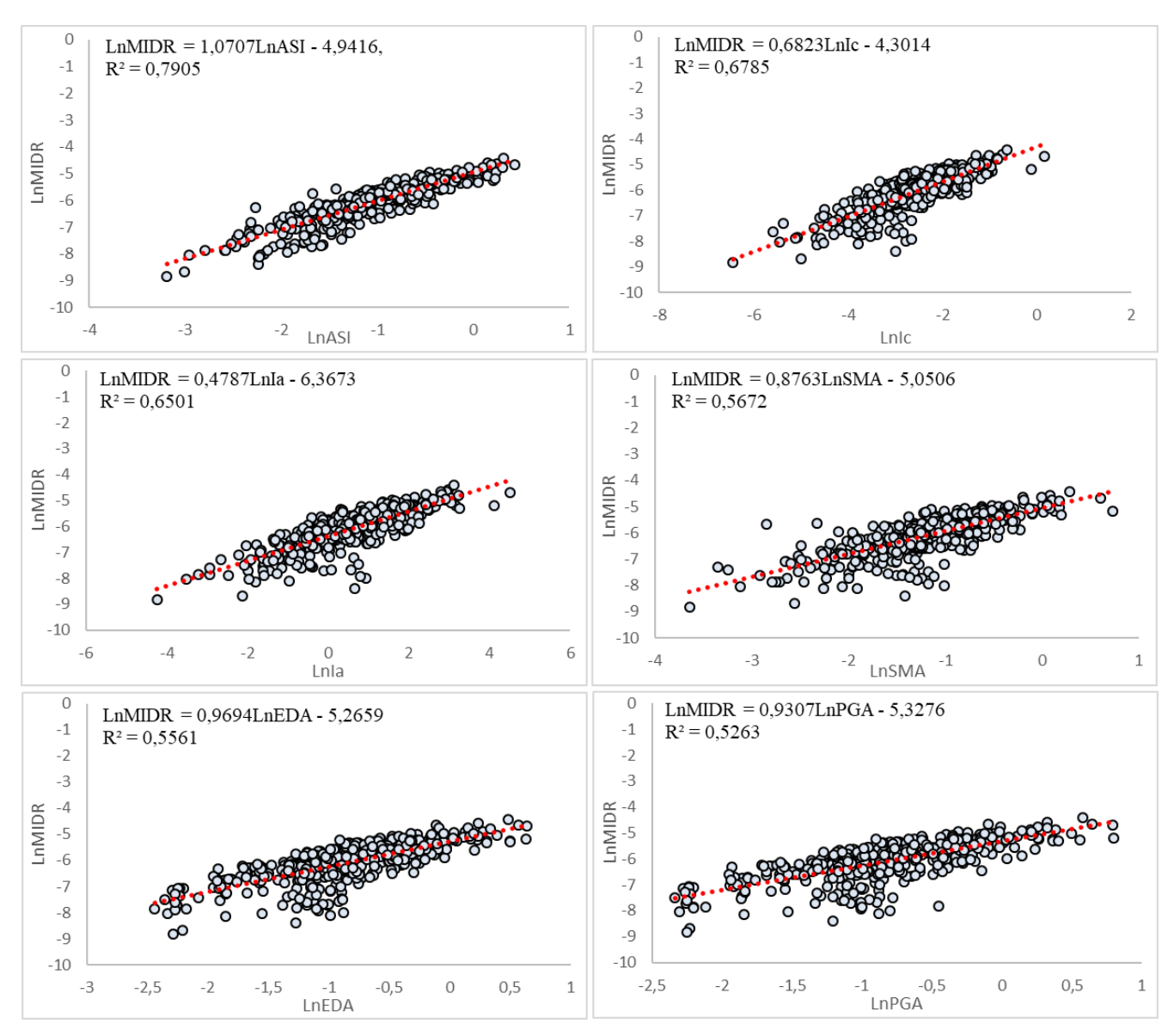


Fig. 6. *DM-IM* scatter plots computed using the cloud analysis method.

As shown in Fig. 6, *DM–IM* scatter plots were obtained for the aqueduct structure considered in this study using the *IM* parameters evaluated by Yesilyurt (2025) for their suitability. Among these, the *ASI* parameter exhibits a denser clustering of data points around the linear

regression line, clearly indicating that the standard deviation associated with this ASI-MIDR pair is lower compared to the others. Furthermore, the highest goodness of fitting (\mathbb{R}^2) and the regression slope (b) were also computed for the ASI parameter.

The main objective of this study is to examine the effect of different damage threshold levels on structural vulnerability. Therefore, fragility curves were developed for the six *IM* parameters shown in Fig. 6 using the threshold values given in Table 1.

2.4. Analytical-based fragility curve

As explained in the previous sections, fragility curves are functions that represent the *PoE* of a certain damage state for a given level of ground motion intensity measure. The procedure for deriving analytical-based fragility curves using the cloud analysis method consists of four main steps. First, *DM-IM* distributions are obtained for the set of earthquake ground motions considered in the study. These distributions illustrate the relationship between the seismic damage parameter and the selected intensity measure parameter. Second, the distribution of the damage parameter corresponding to each intensity level is analyzed, and the probability density function of the damage parameter is computed. In the next step, the damage measure variable is transformed into a log-normal distribution, and the cumulative distribution func-

tion of the log-normal variable is obtained. Based on the threshold values defined in Table 1, the probabilities of reaching or exceeding each damage state are discretely calculated by repeating the process for each intensity level. In the final step of the procedure, the obtained cumulative log-normal probability distribution is fitted to the most appropriate curve. Subsequently, fragility curves are constructed for each damage state, utilizing a two-parameter log-normal distribution, specifically the median (IM_{DS_i}) and logarithmic standard deviation (β_{DS_i}), according to Eq. (1).

$$P[\text{Damage} \ge DS_i | IM] = \Phi\left(\frac{\ln(IM) - \ln IM_{DS_i}}{\beta_{DS_i}}\right)$$
 (1)

In Eq. (1), ϕ denotes the standard cumulative normal distribution function, and IM represents ground motion intensity measure. In this study, fragility curves were derived separately for each IM parameter using the threshold values presented in Table 1. The fragility curves corresponding to the Damage Limitation state are presented in Fig. 7, while those corresponding to the Heavy Damage state are shown in Fig. 8.

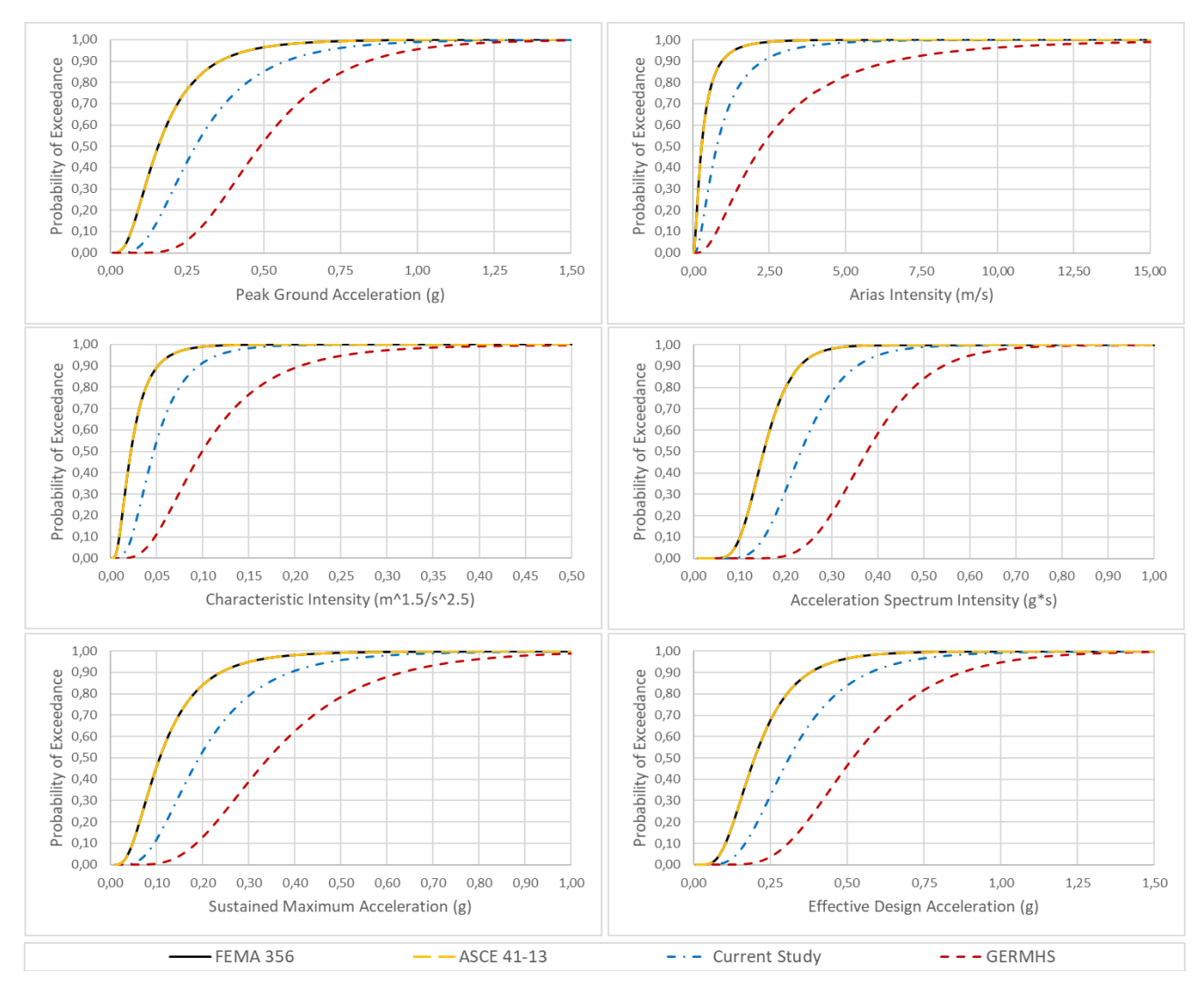


Fig. 7. Fragility curves derived for the Damage Limitation state, taking into account IMs and damage state threshold values.

The fragility curves presented in Figs. 7 and 8 illustrate the probabilistic relationship between seismic demand and the probability of exceeding the Damage Limitation and Heavy Damage state thresholds, emphasizing the impact of varying threshold values on seismic vulnerability.

Since the threshold values for the Damage Limitation state defined by FEMA 356 (2000) and ASCE 41-13 (2013) are identical, the fragility curves presented in Fig. 7 overlap. The fragility curves derived using the threshold values provided by these two standards yield the highest *PoEs* for a given *IM* value. In contrast, the lowest exceedance probabilities are computed using the threshold defined by GERMHS (2017). When the fragility

curves developed based on the threshold levels proposed in the current study are taken as reference, *PoE* values computed for a given *IM* value are found to be higher than those based on the GERMHS (2017) threshold, but lower than those obtained using the threshold values from the other two standards. Examining the fragility curves for the Damage Limitation state in Fig. 7, it is observed that for the *PGA IM* value of 0.25 g, the *PoE* was calculated as 0.765, 0.765, 0.425, and 0.057 for FEMA 356 (2000), ASCE 41-13 (2013), the current study, and GERMHS (2017), respectively. Similarly, for the SMA IM value of 0.30 g, these PoE values were determined to be 0.951, 0.951, 0.792, and 0.389, respectively.

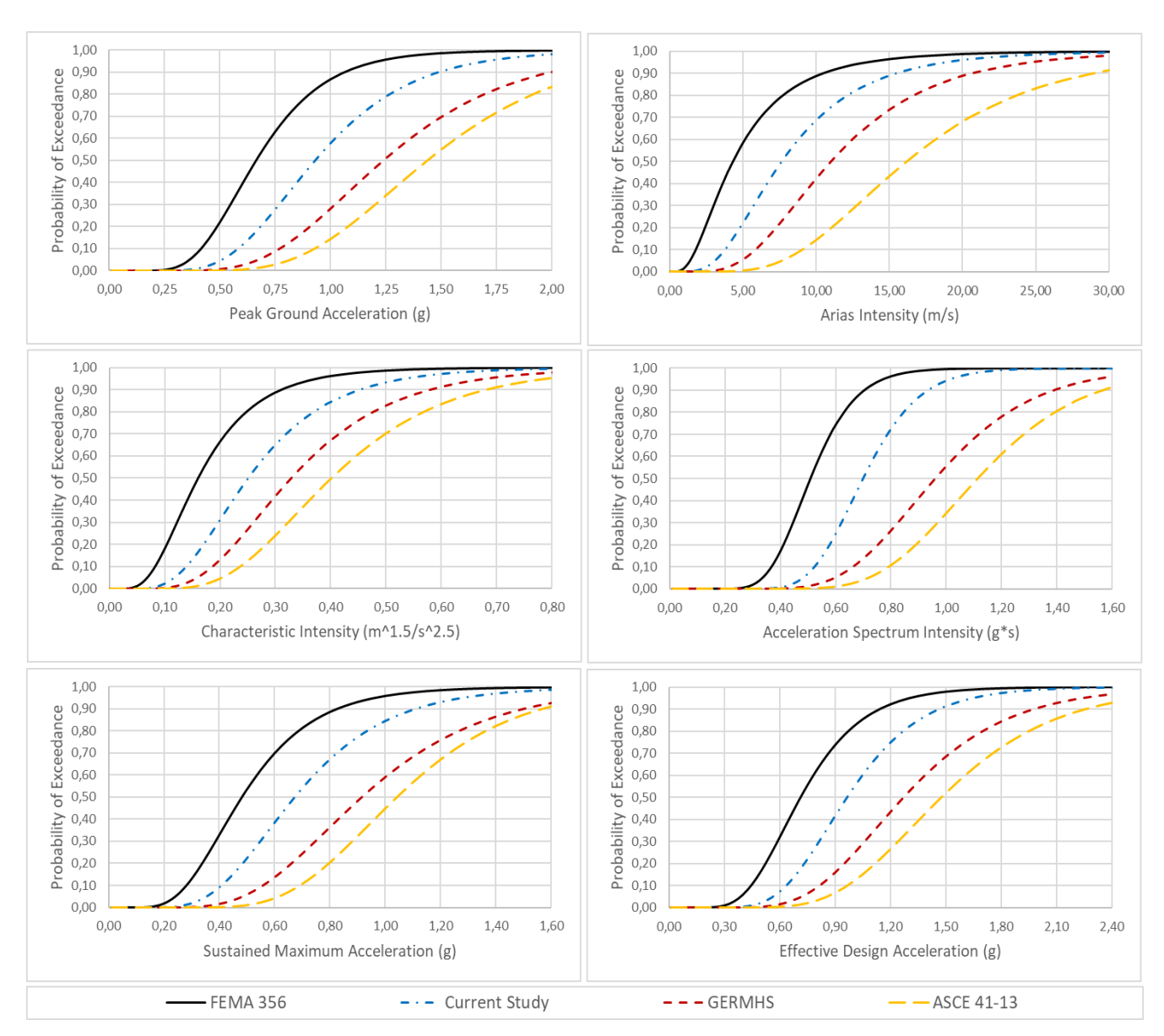


Fig. 8. Fragility curves developed for the Heavy Damage state, considering appropriate intensity measures and damage state threshold values.

In Fig. 8, the fragility curves developed for the Heavy Damage state indicate that, for a given *IM* level, the highest *PoE* is obtained using the FEMA 356 (2000) standard, while the lowest exceedance probability is ob-

served for the ASCE 41-13 (2013) standard. The fragility curves developed in the current study show *PoEs* that are higher than those of GERMHS (2017) and ASCE 41-13 (2013), but lower than those associated with

FEMA 356 (2000) for the same *IM* value. Fig. 8 shows the *PoE* values for the Heavy Damage state for the *EDA IM* parameter value of 1.2 g, which were calculated as 0.922, 0.748, 0.433, and 0.265 for FEMA 356 (2000), the current study, GERMHS (2017), and ASCE 41-13 (2013), respectively. Similarly, for the *AI* value of 10 m/s, the corresponding *PoE* values were computed as 0.887, 0.688, 0.423, and 0.144 for FEMA 356 (2000), the current study, GERMHS (2017), and ASCE 41-13 (2013), respectively.

To enable a more comprehensive assessment, the *PoE* values for the Damage Limitation state, computed using earthquake ground motion records RSN95 and RSN517, are presented in Fig. 9. Similarly, Fig. 10 illustrates the *PoE* values calculated for the Heavy Damage state using

ground motion records RSN143 and RSN1004.

As illustrated in Fig. 9, when the Current study is taken as a reference, the influence of damage threshold levels on the *PoE* varies depending on the earthquake record and the selected *IM*. For example, for a RSN95 record and *PGA*, the computed *PoE* values for the current study, FEMA 356 (2000), ASCE 41-13 (2013), and GERMHS (2017) are 0.6578, 0.893, 0.893, and 0.216, respectively. Similarly, the Heavy Damage state in Fig. 10, for RSN143 and *Ic*, the *PoE* values computed for the current study, FEMA 356 (2000), GERMHS (2017), and ASCE 41-13 (2013) are 0.745, 0.9268, 0.531, and 0.345, respectively. Similar assessments can also be conducted for other *IM* parameters that provide internally consistent *PoE* values.

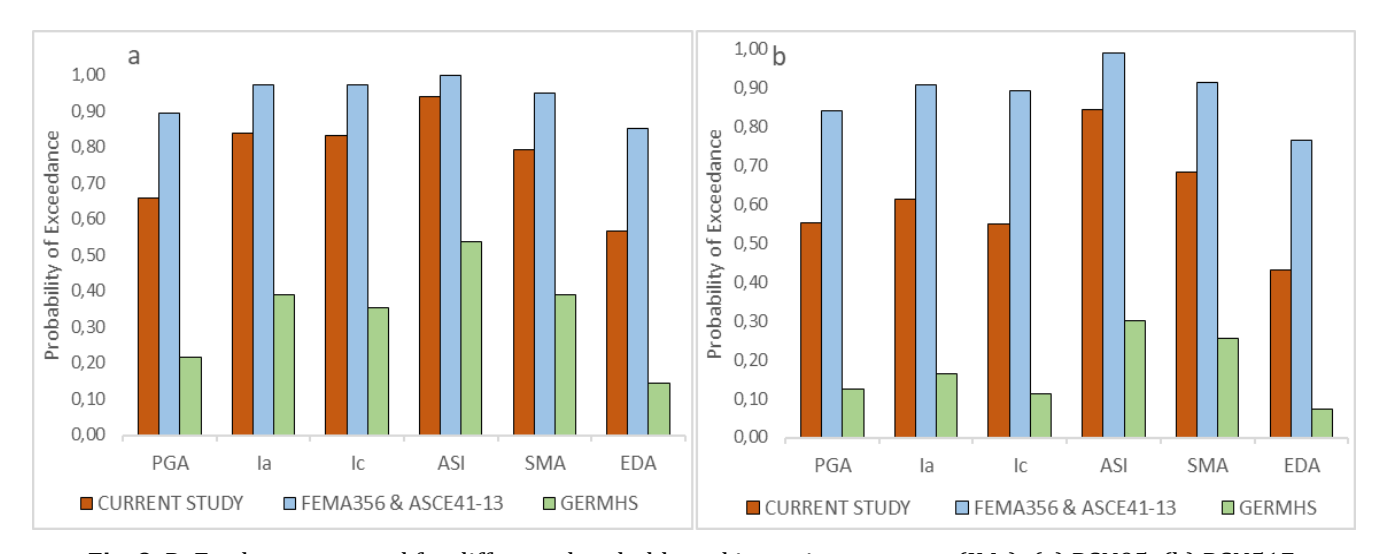


Fig. 9. PoE values computed for different thresholds and intensity measures (IMs): (a) RSN95; (b) RSN517.

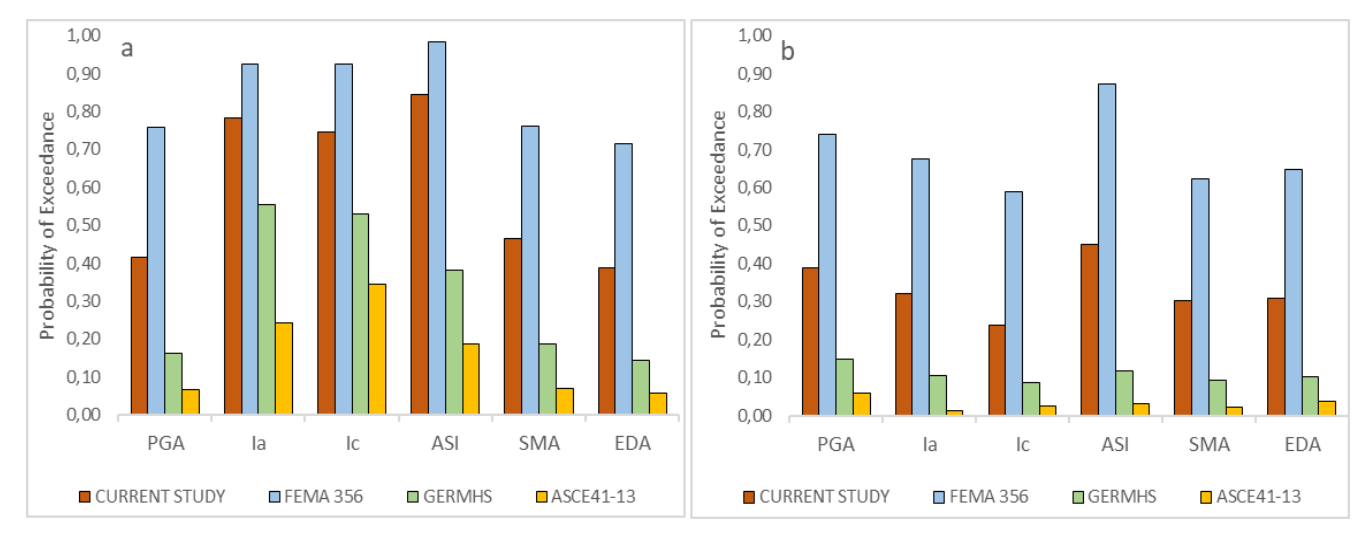


Fig. 10. PoE values computed for different thresholds and intensity measures (IMs): (a) RSN143; (b) RSN1004.

Considering the results of this study as a whole, the damage thresholds used in seismic vulnerability studies have a significant impact on the *PoE* values. Therefore, to carry out a rational and accurate risk assessment, the suitability of the thresholds for the target structure should be thoroughly analyzed, rather than directly using the thresholds presented in the literature.

3. Conclusions

The preservation of historical structures is important for the benefit of future generations. These structures serve as a testament to the cultural characteristics of the period in which they were constructed. In this context, the development of effective decision-making mechanisms based on the reliable assessment of the seismic risk of such structures has become increasingly significant in recent years. The reliability of fragility curves, which are frequently utilized in seismic vulnerability and risk assessment studies, is closely related to the selection of appropriate intensity measures and damage parameters. Moreover, accurately determining the threshold values corresponding to various damage states is critically important for the reliability of these curves.

In this study, the influence of different threshold levels associated with a specific damage state on the seismic vulnerability of a historic masonry aqueduct was examined. For this purpose, a 3D finite element model of the structure was developed, and then response spectrum analyses were conducted. Using the cloud analysis method, the dispersion relationships between the MIDR damage parameter and several *IM* parameters, namely PGA, Ia, Ic, ASI, SMA, and EDA, were obtained. Based on these relationships, fragility curves were developed by adopting MIDR threshold values defined in widely accepted standards such as FEMA 356 (2000), ASCE 41-13 (2013), and GERMHS (2017). Additionally, reference fragility curves were constructed using MIDR values determined via nonlinear static analysis and empirical relationships, and comparative evaluations were carried out through *PoE* values. For instance, at an *EDA IM* value of 0.3 g, the *PoE* value for the "Damage Limitation" damage state in the current study was calculated as 0.468, while the corresponding values based on FEMA 356 (2000), ASCE 41-13 (2013), and GERMHS (2017) were 0.792, 0.792, and 0.088, respectively. In the analysis of the "Heavy Damage" state, for an SMA value of 0.7 g, the PoE values were calculated as 0.541 for the current study, 0.813 for FEMA 356 (2000), 0.244 for GERMHS (2017), and 0.107 for ASCE 41-13 (2013). Similarly, for an ASI value of 0.75 g, the *PoE* in the current study was found to be 0.622, compared to 0.068 for ASCE 41-13 (2013), 0.938 for FEMA 356 (2000), and 0.196 for GERMHS (2017). Such notable differences were also observed for other IM parameters.

These results emphasize that the determination of threshold values plays a critical role in the development of fragility curves, directly affecting their reliability and the accuracy of the seismic risk assessment. Therefore, rather than directly adopting threshold values presented in the literature, it is essential to conduct a detailed evaluation of their suitability for the specific structural characteristics of the target building.

This study demonstrates the importance of threshold values for different damage states and provides a valuable reference for future research on historic masonry aqueducts with different construction characteristics. In future studies, it is essential to establish a sub-classification of historical masonry aqueducts by considering their construction techniques, material properties, geometric configurations, and different modelling assumptions. Following this classification, the derivation of fragility curves for each subclass under both near- and farfault ground motion sets would provide valuable insights. It is anticipated that such a study would yield valuable outcomes, enabling rapid seismic risk assessments of historical aqueducts located in various regions.

Acknowledgements

None declared.

Funding

The author received no financial support for the research, authorship, and/or publication of this manuscript.

Conflict of Interest

The author declared no potential conflicts of interest with respect to the research, authorship, and/or publication of this manuscript.

Author Contributions

The author confirms sole responsibility for all aspects of the study including conception and design, acquisition of data, analysis and interpretation of data, drafting the manuscript, revising it critically for important intellectual content; and gave final approval of the version to be published.

Data Availability

The datasets created and/or analyzed during the current study are not publicly available, but are available from the corresponding author upon reasonable request.

REFERENCES

AFAD (2023). Şubat 2023 Pazarcık–Elbistan Kahramanmaraş (Mw: 7.7 – Mw: 7.6) depremleri raporu. General Directorate of Earthquake and Risk Reduction, Earthquake Department, Ankara, Türkiye. (in Turkish)

Akturk F, Yesilyurt A, Cakir F (2025). Optimal intensity measures for probabilistic seismic demand modeling of single-domed historical masonry buildings. *Engineering Failure Analysis*, 171,109378.

Alpaslan E, Dinç B, Hacıefendioğlu K, Demir G, Köksal O (2017). Modal identification of a reduced-scale masonry arch bridge with experimental measurements and finite element method. *Challenge Journal of Structural Mechanics*, 3(3), 108-115.

Alpaslan E, Karaca Z (2020). Model updating of a reduced-scaled masonry bridge by using response surface method. *Challenge Journal of Structural Mechanics*, 6(1), 41-51.

ANSYS (2022). Engineering Simulation Software. , ANSYS [Online]. Available: https://www.ansys.com

ASCE 41-13 (2013). Seismic rehabilitation of existing buildings. American Society of Civil Engineers, Reston, VA.

Balcan C, Aydın EÖ, Ünsal Ö (2024). Value-based optimization model for cultural route design: Ancient Water Supply Heritage of Istanbul (Türkiye). *Journal of Cultural Heritage*, 70, 97-110.

Cattari S, Calderoni B, Caliò I, Camata G, de Miranda S, Magenes G, Saetta A (2022). Nonlinear modeling of the seismic response of masonry structures: critical review and open issues towards engineering practice. *Bulletin of Earthquake Engineering*, 20(4), 1939-1997.

Cheng G, Zhang Y, Huang J, Liu J, Zhang J (2020, September). Vulnerability analysis of aqueduct structure based on boundary method. IOP Conference Series: Earth and Environmental Science, 567(1), 012036.

Cosgun C, Mangir A (2018). Earthquake performance of collapsed school building under Van-Tabanli (Mw=7.2) earthquake. *Challenge Journal of Structural Mechanics*, 4(4), 159-175.

Çakır F (2021). A simplified method for determining the seismic performance of historical structures: a case of Kaya Çelebi Mosque. Journal of the Faculty of Engineering and Architecture of Gazi University, 36(3), 1643-1656.

Cakir F (2022). Performance-based assessment of long masonry structures. *Challenge Journal of Structural Mechanics*, 8(2), 47-56.

Cakir F, Uckan E, Shen J, Seker BS, Akbas B (2015). Seismic damage evaluation of historical structures during Van earthquake, October 23, 2011. Engineering Failure Analysis, 58, 249-266.

- Cakir F, Uckan E, Shen J, Seker S, Akbas B (2016). Seismic performance evaluation of slender masonry towers: a case study. *The Structural Design of Tall and Special Buildings*, 25(4), 193-212.
- Dogangun A, Sezen H (2012). Seismic vulnerability and preservation of historical masonry monumental structures. *Earthquake and Structures*, 3(1), 83-95.
- Drougkas A (2022). Macro-modelling of orthotropic damage in masonry: Combining micro-mechanics and continuum FE analysis. *Engineering Failure Analysis*, 141, 106704.
- Drucker DC, Prager WJ (1952). Soil mechanics and plastic analysis or limit design. *Quarterly of Applied Mathematics*, 10(2), 157-165.
- Du M, Zhang S, Wang C, She L, Li J, Lu T (2023). Seismic fragility assessment of aqueduct bent structures subjected to mainshock-aftershock sequences. *Engineering Structures*, 292, 116505.
- Du M, Zhang S, Wang C, Li Z, Yao J, Lu T (2024a). Development of the compound intensity measure and seismic performance assessment for aqueduct structures considering fluid-structure interaction. *Ocean Engineering*, 311, 118838.
- Du M, Yang X, Zhang S, Wang C, Guo R, Li Z, Yao J (2024b). Probabilistic seismic performance assessment of aqueduct structures considering different sources of uncertainty. *Structures*, 70, 107750.
- Ercan E, Alver N, Nuhoğlu A (2015). Evaluation of material properties by NDT methods and FEM analysis of a stone masonry arch bridge. *Challenge Journal of Structural Mechanics*, 1(4), 168-172.
- Erdik M, Doyuran V, Akkaş N, Gülkan P (1985). A probabilistic assessment of the seismic hazard in Turkey. *Tectonophysics*, 117(3-4), 295-344.
- Erkek H, Yetkin M (2023). Assessment of the performance of a historic minaret during the Kahramanmaraş earthquakes (Mw 7.7 and Mw 7.6). *Structures*, 58, 105620.
- FEMA 274 (1997). NEHRP commentary on the guidelines for the seismic rehabilitation of buildings. Federal Emergency Management Agency, Washington, DC.
- FEMA 356 (2000). Pre-standard and commentary for the seismic rehabilitation of buildings. Federal Emergency Management Agency, Washington, DC.
- GERMHS (2017). A guideline for earthquake risk management of historical structures in Turkey. General Directorate of Foundations, Ankara, Türkiye.
- Gkournelos PD, Triantafillou TC, Bournas DA (2022). Seismic upgrading of existing masonry structures: A state-of-the-art review. *Soil Dynamics and Earthquake Engineering*, 161, 107428.
- Gonen S, Pulatsu B, Erdogmus E, Karaesmen E, Karaesmen E (2021).

 Quasi-static nonlinear seismic assessment of a fourth century AD
 Roman Aqueduct in Istanbul, Turkey. Heritage, 4(1), 401-421.
- Işık E, Karaşin İB, Demirci A, Büyüksaraç A (2020). Seismic risk priorities of site and mid-rise RC buildings in Turkey. *Challenge Journal of Structural Mechanics*, 6(4), 191-203.
- Kappos AJ, Panagopoulos G, Panagiotopoulos C, Penelis G (2006) A hybrid method for the vulnerability assessment of R/C and URM buildings. *Bulletin of Earthquake Engineering*, 4, 391–413.
- Kocaman İ (2023). The effect of the Kahramanmaraş earthquakes (Mw 7.7 and Mw 7.6) on historical masonry mosques and minarets. Engineering Failure Analysis, 149, 107225.
- Kocaman İ, Mercimek Ö, Gürbüz M, Erbaş Y, Anıl Ö (2024). The effect of Kahramanmaraş earthquakes on historical Malatya Yeni Mosque. Engineering Failure Analysis, 161, 108310.
- Korkmaz M, Ozdemir MA, Kavali E, Cakir F (2018). Performance-based assessment of multi-story unreinforced masonry buildings: The

- case of historical Khatib School in Erzurum, Turkey. *Engineering Failure Analysis*, 94, 195-213.
- Lagomarsino S, Cattari S (2015). PERPETUATE guidelines for seismic performance-based assessment of cultural heritage masonry structures. *Bulletin of Earthquake Engineering*, 13, 13-47.
- Lagomarsino S, Giovinazzi S (2006). Macroseismic and mechanical models for the vulnerability and damage assessment of current buildings. *Bulletin of Earthquake Engineering*, 4, 415–443.
- Lamego P, Lourenço PB, Sousa ML, Marques R (2017). Seismic vulnerability and risk analysis of the old building stock at urban scale: application to a neighbourhood in Lisbon. *Bulletin of Earthquake En*aineering, 15, 2901-2937.
- Liu J, Xu J, Huang L (2025). Seismic vulnerability analysis of aqueducts based on probability density evolution method. *Transportation Research Record*, 2679(6), 203-226.
- Ma Y, Wu Z, Liu Z, Zhang M, Aibaidula M (2022). Seismic fragility analysis of aqueduct structural systems based on G-PCM method. *Sustainability*, 14(20), 13161.
- Ozdemir MA, Kaya ES, Aksar B, Seker B, Cakir F, Uckan E, Akbas B (2017). Seismic vulnerability of masonry Jack arch slabs. *Engineering Failure Analysis*, 77, 146-159.
- Rota M, Penna A, Magenes GJES (2010). A methodology for deriving analytical fragility curves for masonry buildings based on stochastic nonlinear analyses. *Engineering Structures*, 32(5), 1312-1323.
- Vanin F, Zaganelli D, Penna A, Beyer K (2017) Estimates for the stiffness, strength and drift capacity of stone masonry walls based on 123 quasi-static cyclic tests reported in the literature. *Bulletin of Earthquake Engineering*, 15(12), 5435–5479.
- Vicente R (2008). Estrat'e'gias e Metodologias para Intervençoes ~ de Reabilitacao ~ Urbana—Avaliaç~ ao da Vulnerabilidade e do Risco Sı'smico do Edificado da Baixa de Coimbra. *PhD Thesis*, University of Aveiro, Aveiro, Portugal. (in Portuguese).
- Xu X, Liu X, Jiang L, Ali Khan MY (2021). Dynamic damage mechanism and seismic fragility analysis of an aqueduct structure. *Applied Sciences*, 11(24), 11709.
- Yesilyurt A (2025). Selection of optimum intensity measure parameters for seismic fragility analysis of typical Roman aqueduct. Structures, 71, 108085.
- Yesilyurt A, Akcan SO, Zulfikar A (2021a). Rapid power outage estimation for typical electric power systems in Turkey. *Challenge Journal of Structural Mechanics*, 7(2), 84-92.
- Yesilyurt A, Zulfikar AC, Tuzun C (2021b). Site classes effect on seismic vulnerability evaluation of RC precast industrial buildings. *Earthquakes and Structures*, 21(6), 627-639.
- Yesilyurt A, Akcan SO, Cetindemir O, Zulfikar AC (2024). Probabilistic earthquake risk consideration of existing precast industrial buildings through loss curves. *Geomechanics and Engineering*, 37(6), 565-576.
- Yilmaz MF, Çaglayan BÖ, Özakgül K (2018). Seismic assessment of a curved multi-span simply supported truss steel railway bridge. Challenge Journal of Structural Mechanics, 4(1), 13-17.
- Yücemen MS, Yılmaz Ç (2015). Probabilistic assessment of earthquake insurance premium rates for the Gumusova-Gerede Motorway Section. Challenge Journal of Structural Mechanics, 1(2), 42-47.
- Zhang S, Du M, Wang C, Sun B, She L, Liu W (2022). Fragility analysis of high-span aqueduct structure under near-fault and far-field ground motions. Structures, 46, 681-697.
- Zheng X, Shen Y, Zong X, Su H, Zhao X (2023). Vulnerability analysis of main aftershock sequence of aqueduct based on incremental dynamic analysis method. *Buildings*, 13(6), 1490.



Research Article

Seismic performance assessment of timber-framed (himiş) structures with different infill materials

Muhammed Alperen Ozdemir a,* (D)

^a Department of Civil Engineering, Iğdır University, 76000 Iğdır, Türkiye

ABSTRACT

This study investigates the seismic performance of traditional timber-framed (himiş) structures incorporating different types of infill materials through advanced nonlinear finite element modeling. Timber-infilled walls represent a widely used hybrid construction typology in seismic regions, where the interaction between the ductile timber frame and brittle infill materials critically influences structural behavior. Four configurations are analyzed: (1) Timber frame with adobe (mudbrick) infill; (2) Timber frame with fired clay brick infill; (3) Timber frame with natural rubble stone infill; and (4) Bare timber frame. A series of three-dimensional pushover analyses are conducted using ANSYS Workbench, where all materials are modeled using Multilinear Isotropic Hardening plasticity, including contact-based interface definitions and geometric nonlinearity. The mechanical behavior of each wall system is interpreted based on key seismic performance indicators, including initial lateral stiffness, base shear capacity, effective displacement ductility, and energy dissipation. Results show that while infill materials significantly increase the lateral strength and stiffness of the wall systems, they also introduce varying degrees of brittleness and reduced ductility. These findings emphasize the critical role of infill type in the seismic response of timber-framed walls and highlight the importance of understanding frame-infill interaction for the assessment and retrofitting of traditional building stock in earthquake-prone regions.

ARTICLE INFO

Article history:

Received – July 18, 2025
Revision requested – August 11, 2025
Revision received – August 23, 2025
Accepted – September 3, 2025

Keywords:

Timber-framed structures Himiş structures Infill materials Seismic behavior Pushover analysis



This is an open access article distributed under the CC BY licence.

© 2025 by the Author.

Citation: Ozdemir MA (2025). Seismic performance assessment of timber-framed (himiş) structures with different infill materials. Challenge Journal of Structural Mechanics, 11(3), 149–159.

1. Introduction

Timber-framed structures with infill panels—locally known as *himis* in Türkiye—represent a significant segment of the world's vernacular architectural heritage. These hybrid systems, consisting of a load-bearing timber skeleton and non-structural infill walls made from masonry, adobe, stone, or other locally sourced materials, have been used for centuries across a wide variety of climatic, topographic, and seismic regions. Their prevalence is not limited to Anatolia but extends across Europe, Asia, and the Americas, reflecting a universal architectural response to the need for affordable, adaptable, and earthquake-resistant housing.

Timber-framed structures outperform unreinforced masonry buildings during earthquakes primarily due to their light weight, ductile joints, and ability to dissipate seismic energy through controlled deformations. In contrast, masonry walls are typically heavier and brittle, failing suddenly once their limited tensile strength is exceeded. This fundamental difference explains why properly constructed himis systems have repeatedly shown superior survival rates in past earthquakes. In Europe, these systems are widely known under different names: Fachwerk in Germany, Colombage in France, Half-timbering in the United Kingdom, and Pruga or bondruk in the Balkans. Each term denotes a variation of the same core principle: a flexible timber frame, often

^{*} Corresponding author. Tel.: +90-476-223-0040; E-mail address: m.alperen.ozdemir@igdir.edu.tr (M. A. Ozdemir) ISSN: 2149-8024 / DOI: https://doi.org/10.20528/cjsmec.2025.03.004

filled with clay bricks, wattle and daub, or rubble stone. In Asia, similar typologies exist in Japan (*minka*), Nepal and Bhutan (traditional *dzong* buildings), and in the Indian subcontinent under the term *dhajji dewari*, particularly in the Himalayan regions where seismicity is high (Aktaş 2017). In Latin America, the *bahareque* and *quincha* systems in Colombia and Peru, and *taipa de mão* in Brazil, display a comparable structural logic, developed through indigenous knowledge systems that combine seismic intuition with resource economy (Dima and Dutu 2016; Dutu et al. 2018). The global spread of these structures' underscores not only their adaptability to different environments but also their relevance in seismic resilience (Fig. 1). From a structural engineering perspective, the timber frame provides a flexible yet stable

skeleton that accommodates lateral deformations during seismic events, while the infill materials contribute mass and stiffness but may also become sources of vulnerability if poorly integrated. In seismic events such as the 1999 İzmit Earthquake in Türkiye, the 2005 Kashmir Earthquake in Pakistan, the 2015 Gorkha Earthquake in Nepal and the 2023 Kahramanmaraş Earthquakes in Türkiye, observations consistently showed that timberframed structures, when properly constructed, performed significantly better than unreinforced masonry buildings (Vieux-Champagne et al. 2014; Qu et al. 2020; Tan et al. 2024). Their performance is typically characterized by ductile behavior, energy dissipation through joint flexibility, and the ability to localize damage without total collapse.

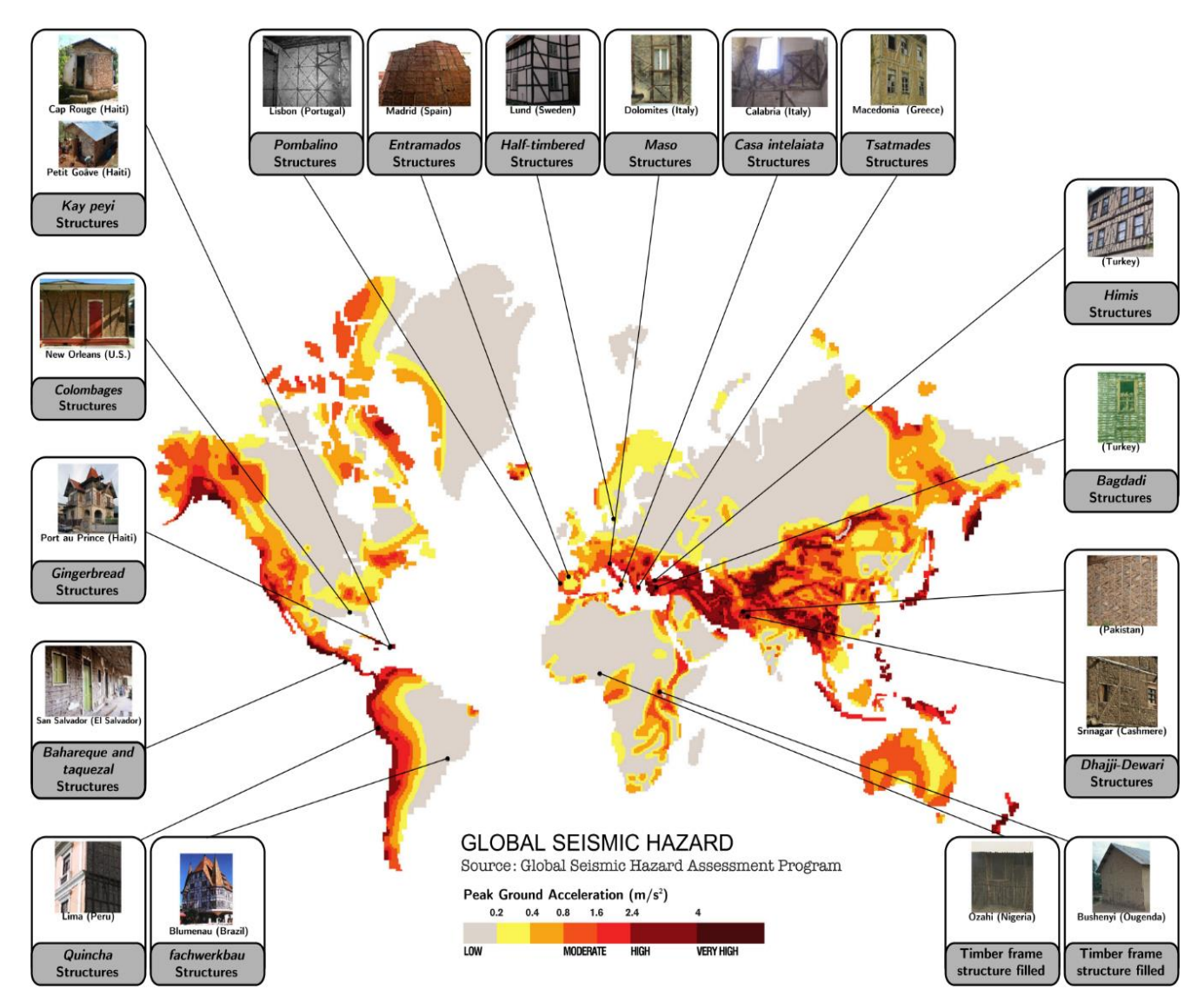


Fig. 1. Examples of the timber-framed structures in the world (Vieux-Champagne et al. 2014).

In addition to their structural role, timber-framed systems with infill panels also offer notable environmental and economic advantages. Locally sourced materials such as timber, adobe, rubble stone, and clay brick reduce transportation needs and embodied energy, contributing to sustainability. These materials are generally

low-cost and easily repairable, which historically made himis construction both affordable and resilient. Recent studies further underline that the ecological footprint of such vernacular materials is significantly lower compared to modern industrial alternatives (Karaman and Zeren 2015; Dikmen 2010).

2. Structural Behavior of the Timber-Framed Structures

In timber-framed wall systems with diagonal bracing and masonry infill, the global lateral stiffness and load-carrying capacity are governed by a combination of axial action in the bracing element, flexural and shear deformation in vertical and horizontal timber members, and in-plane compression of the infill panel. Under in-plane lateral loading, the braced frame with infill may be idealized as a statically indeterminate truss-frame system, where the diagonal brace primarily carries axial forces and the infill behaves as a distributed compression field.

Assuming the brace is pinned at both ends and oriented at an angle θ , the axial force N_b in the brace due to horizontal load P at the top of the wall can be approximated using equilibrium:

$$N_b = \frac{P}{2 \cdot \cos \theta} \tag{1}$$

where, P is the lateral load (e.g., base shear), θ is the angle between brace and horizontal axis and N_b is the axial force in brace.

This force leads to axial deformation in the brace:

$$\delta_b = \frac{N_b \cdot L_b}{A_b \cdot E_b} \tag{2}$$

where, L_b is the length of brace, A_b is the cross-sectional area of brace and E_b is the modulus of elasticity of timber.

The vertical timber elements resist lateral drift through bending. For a cantilever model under lateral top load *P*, the tip displacement due to flexure is:

$$\Delta_{\text{flex}} = \frac{P \cdot h^3}{3EI} \tag{3}$$

Here, Δ_{flex} : Lateral tip displacement due to flexure, P: Lateral load applied at the top, h: Height of the column, E: Modulus of elasticity of timber, I: Moment of inertia of the column cross-section.

The effective lateral stiffness of the system can be idealized as a parallel spring system:

$$K_{\text{total}} = K_{\text{frame}} + K_{\text{brace}} + K_{\text{infill}}$$
 (4)

Here, $K_{\rm frame}$ is the elastic lateral stiffness of the timber frame alone, and $K_{\rm infill,eff}$ is the effective contribution of the infill panel, which depends on its geometry, material stiffness, and contact with the frame. The frame's stiffness can be expressed, for a single-story shear wall, as:

$$K_{\text{frame}} = \frac{12EI}{h^3} \tag{5}$$

Before cracking, the masonry infill panel adds significant stiffness through its in-plane shear and diagonal compression. The initial stiffness of the panel can be approximated using its shear modulus G_m , thickness t, height h, and width b:

$$K_{\text{infill}} = \frac{G_{m} \cdot t \cdot b}{h} \tag{6}$$

$$K_{\text{brace}} = \frac{A_b \cdot E_b}{L_b} \tag{7}$$

where, K_{brace} is the axial stiffness of the diagonal brace, A_b is the cross-sectional area of the brace, E_b is the modulus of elasticity of timber and L_b is the length of the brace.

The lateral resistance from the infill is governed by its compressive strut-like behavior during early loading. However, this capacity rapidly diminishes due to cracking, which can be captured through nonlinear material softening. The energy dissipation potential of the system is closely related to the area under the load–displacement curve:

$$E_d = \int_0^{\Delta_u} P(\Delta) d \tag{8}$$

The ductility ratio μ , which is critical in seismic performance assessment, is defined as:

$$\mu = \frac{\Delta_u}{\Delta_v} \tag{9}$$

where Δ_y is the displacement at yield, and Δ_u is the ultimate displacement at 80% of the maximum lateral load. Higher values of μ indicate greater deformation capacity before collapse.

Contact behavior at the timber–infill interface is another crucial component. The shear resistance at this interface is a function of the friction coefficient μ and the normal contact force N:

$$F_f = \mu \cdot N \tag{10}$$

This governs the onset of sliding and separation, which leads to loss of composite action. Once detachment begins, K_{infill} reduces significantly, and the system behaves similarly to a bare timber frame.

Therefore, the global seismic behavior of timber-framed infilled systems can be understood as a multiphase response:

- Elastic phase: Frame and infill behave monolithically
- Cracking phase: Infill cracks; stiffness decreases
- Plastic/softening phase: Infill loses load-bearing capacity; frame dominates
- Residual phase: Frame sustains remaining loads until failure

3. Finite Element Modeling

This study employs a numerical modeling approach to investigate the seismic performance of traditional timber-framed (himiş) wall systems with various infill materials under lateral earthquake-type loading. The numerical simulations are conducted in a finite element environment using ANSYS Workbench, where nonlinear static (pushover) analyses are performed on three-dimensional wall models. The analysis considers four different wall configurations: (a) A timber frame with adobe (mudbrick) infill; (b) A timber frame with fired clay brick infill; (c) A timber frame with natural rubble stone infill; and (d) A bare timber frame without infill (Fig. 2), used as a reference case to isolate the contribution of infill to the structural behavior.

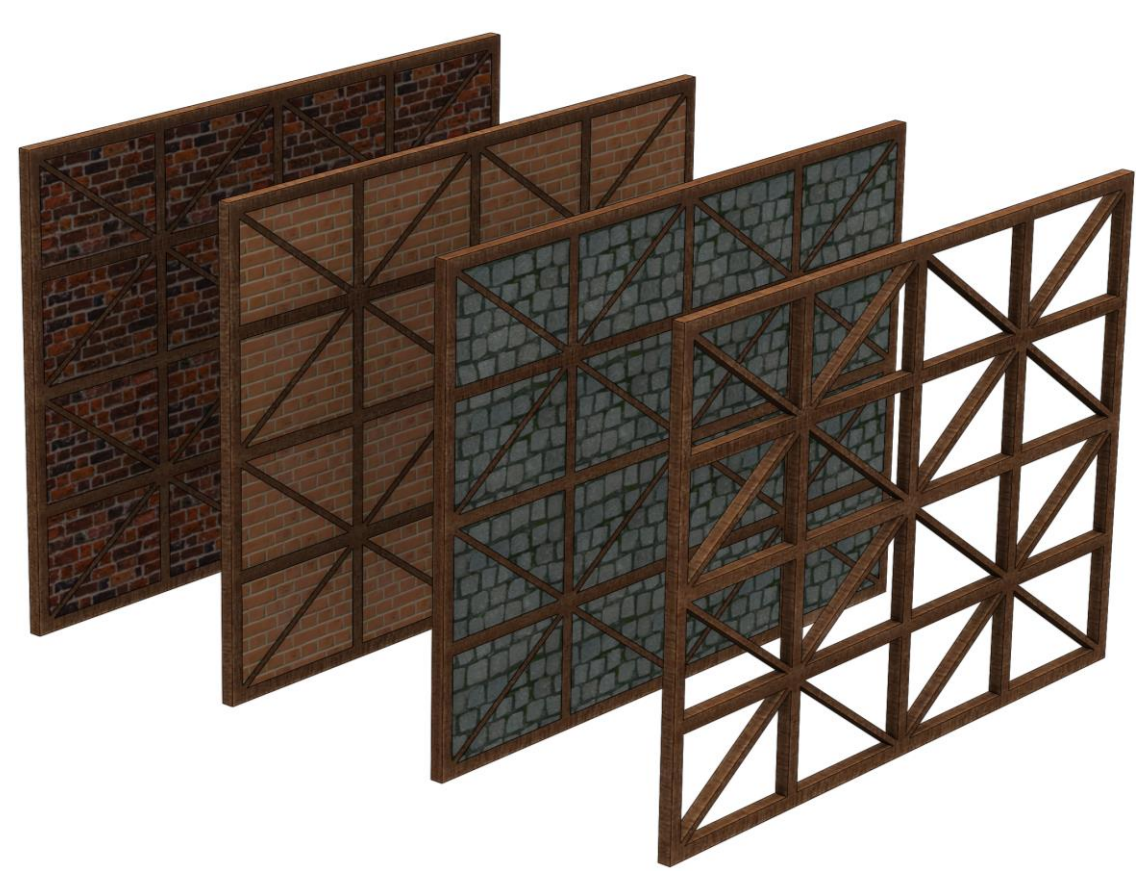


Fig. 2. Different wall configurations: (a) A timber frame with adobe (mudbrick) infill; (b) A timber frame with fired clay brick infill; (c) A timber frame with natural rubble stone infill; and (d) A bare timber frame without infill.

All wall specimens are modeled based on a standardized geometry that reflects traditional himis construction widely observed in Anatolia. The timber framed shear wall has a width of 490 cm and a height of 370 cm, with vertical timber studs spaced at regular intervals and interconnected by horizontal beams and diagonal braces. The cross-sectional dimensions of vertical and

horizontal elements are taken as 10 cm×10 cm while the cross-sectional dimensions of diagonal braces are taken as 10 cm×5 cm, representing typical softwood sections used in himis construction (Fig. 3). The infill is fully enclosed within the timber frame but is not mechanically anchored to it, replicating the friction-based interaction seen in actual historical structures.

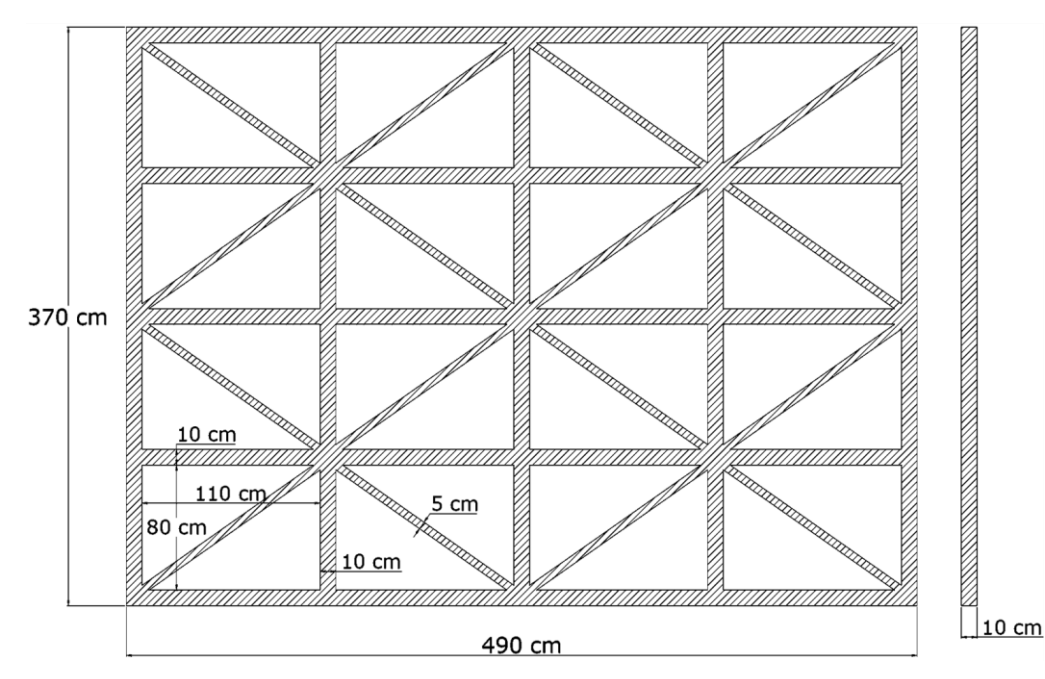


Fig. 3. Dimensions of the timber frame.

The numerical models are developed using SOLID186 elements, which are 20-node hexahedral elements capable of capturing large deformation and plasticity effects. To represent the interaction between the timber frame and the masonry infill, surface-to-surface contact elements (CONTA174 and TARGE170) are employed. Frictional contact is defined as material-dependent coefficients: 0.5 for adobe, 0.4 for fired clay brick, and 0.3 for rubble stone (NAVFAC DM7-02, 1986). Normal separation is allowed, while sliding is governed by a penalty-based Coulomb friction model, enabling the realistic simulation of detachment or slip along the timber-infill interface.

A key feature of this study is the consistent use of the Multilinear Isotropic Hardening (MLIH) plasticity model for all materials, including both the timber and infill types. This modeling choice enables a unified formulation for nonlinear material behavior, while still capturing the distinct stress–strain responses of each material (Table 1). Finite element models (FEMs) of the frames

are given in Fig. 4. The MLIH model was selected for all materials to ensure a unified modeling framework and computational stability. Although timber is orthotropic and masonry materials such as adobe, brick, and rubble stone exhibit brittle fracture modes, adopting a common nonlinear plasticity model allowed for direct comparison between different wall configurations under consistent assumptions. This approach is appropriate for evaluating global seismic performance, although it does not reproduce localized damage mechanisms. While the MLIH plasticity model ensures computational stability and uniformity across different materials, it does not explicitly capture the initiation and propagation of cracks, nor the localization of damage. This simplification is particularly significant for brittle materials such as rubble stone, where fracture and crushing dominate the failure process. Therefore, the results should be interpreted as approximations of global nonlinear response rather than precise simulations of localized cracking behavior.

Table 1. Mechanical properties of materials used in the nonlinear numerical models.

Material	Density (kg/m³)	σ_y (MPa)	E _{initial} (MPa)	Ultimate strain
Timber (pine)	550	30	10,000	0.004
Adobe	1700	1.2	300	0.003
Fired clay brick	1800	10.0	4000	0.0015
Rubble stone	2200	15.0	6000	0.001

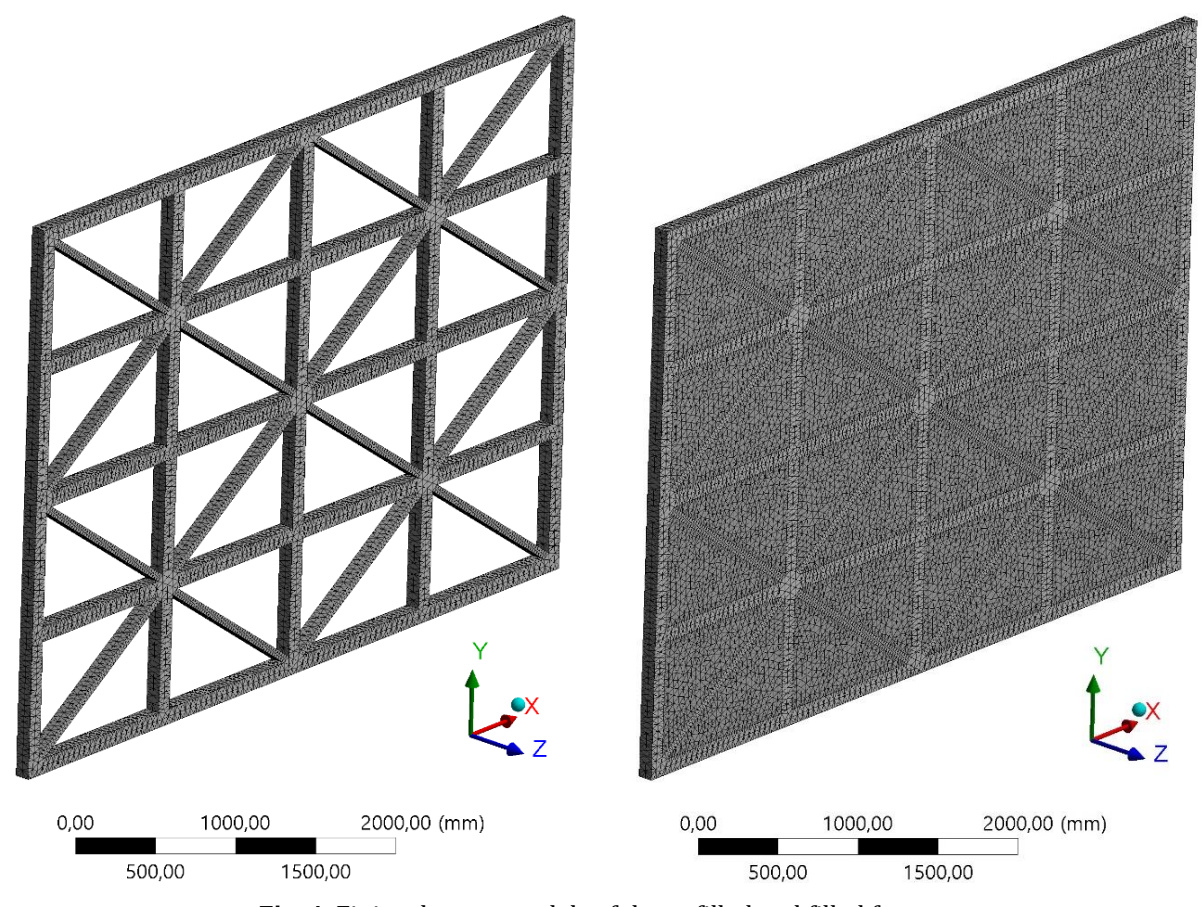


Fig. 4. Finite element models of the unfilled and filled frames.

To ensure reliability of the FEM results, the base of the wall models was fully fixed in all degrees of freedom, while displacement-controlled loading was applied at the top beam to simulate lateral seismic actions. A mesh sensitivity study was conducted, where element sizes were progressively refined until the difference in peak base shear capacity was less than 3%. This confirmed that the selected mesh density provided convergent and mesh-independent results. Convergence was verified in ANSYS through force–displacement equilibrium criteria at each load increment.

4. Pushover Analyses

The pushover analysis is performed under displacement-controlled loading, with a gradually increasing lateral displacement applied at the top beam of the wall. Before lateral loading, self-weight is activated to simulate gravity effects. The base of the wall is fully fixed in all degrees of freedom. The analysis continues until the structure reaches its ultimate capacity and begins to exhibit significant strength degradation or loss of equilibrium. Geometric nonlinearity is included in all analyses to capture large displacement effects, which are particularly relevant for systems with deformable joints and sliding interfaces.

From each simulation, key seismic performance parameters are extracted. These include the initial lateral stiffness, peak base shear, displacement capacity, energy dissipation (measured as the area under the force–displacement curve), and observed failure mechanisms. Special attention is given to the distribution of plastic strain and relative displacement along the timber-infill interfaces, as these are known to influence the global behavior of himis systems. By comparing the capacity curves and ductility of each configuration, the contribution of each infill material to the overall seismic resistance is evaluated.

The methodology adopted herein allows for a controlled comparison of different infill scenarios under consistent boundary and loading conditions, using a computationally efficient and stable material modeling strategy. Although the MLIH model does not capture explicit fracture or crack propagation, it effectively simulates the global nonlinear response and enables meaningful performance assessment of different infill types within timber-framed structures.

The nonlinear pushover analysis provided a clear comparative framework for assessing the seismic performance of the four wall configurations. The force–displacement (capacity) curves obtained from the analysis indicate distinct behavioral patterns for each infill material. Overall, the filled frames exhibited significantly higher lateral stiffness and base shear capacity than the bare timber frame, affirming the structural contribution of the infill panels. However, variations in ductility and energy dissipation behavior among the infill types revealed important trade-offs between strength and deformation capacity.

The rubble stone-infilled frame demonstrated the highest initial stiffness and peak base shear among all

configurations. This is attributed to the high density and compressive strength of stone masonry. However, its capacity curve exhibited a sharp post-peak decline, indicating brittle failure with limited energy dissipation and deformation tolerance. The fired clay brick infill also contributed to considerable stiffness and strength, though to a lesser degree than stone. Its post-peak response was moderately softening, offering a slightly more ductile behavior but still prone to localized interface failure.

The adobe-infilled wall, while having the lowest peak strength among the infilled systems, displayed the most ductile behavior. Its capacity curve showed a gradual softening phase and delayed stiffness degradation, allowing more lateral deformation before failure. This translated into the highest energy dissipation area under the curve and the largest effective ductility ratio. The interface contact in adobe-infilled walls remained engaged longer due to better frictional resistance and more distributed cracking, enabling a more controlled release of seismic energy.

The bare timber frame, as expected, exhibited the lowest strength and stiffness. However, its deformation capacity was considerably high, and no abrupt strength loss was observed even at large lateral displacements. This confirms that in the absence of brittle infill, the timber frame maintains a stable, though flexible, seismic behavior, acting more like a life-safe but damage-prone system.

These behavioral trends are reflected clearly in the following figures (Figs. 5-9). The displacement capacity and energy absorption potential correlate with the postpeak slope and area under each curve, emphasizing the importance of ductility over mere strength. The differences between the configurations highlight the structural and seismic implications of infill material selection in traditional himis walls. The effect of different infill materials on the seismic energy dissipation capacity of timber-framed (himis) structures was investigated in detail. According to the results obtained from pushover analyses, the adobe (mudbrick) infill exhibited the highest energy dissipation capacity with approximately 215.13 kN·m. This was followed by rubble stone infill (113.74 kN·m), fired clay brick infill (27.76 kN·m), and finally the bare frame (4.83 kN·m). The superior performance of adobe can be attributed to its ability to absorb energy through progressive cracking and deformation. Although rubble stone infill had higher strength, its brittle failure mechanism limited its energy dissipation capacity. The brick infill provided moderate performance, while the bare frame exhibited minimal energy absorption due to the absence of lateral stiffness contribution from infill materials. These findings clearly demonstrate that the type of infill material plays a crucial role not only in enhancing load-bearing performance but also in improving the seismic energy absorption and distribution characteristics of the overall structure.

The quantitative results presented in Table 2 high-light the pronounced effect of different infill materials on the seismic behavior of timber-framed (himiş) walls. The bare timber frame exhibited the weakest performance, with an initial stiffness of only 20.57 kN/mm, a maximum base shear of 385 kN, and a ductility ratio of 1.53,

corresponding to an ultimate displacement of 22.8 mm. Its energy dissipation capacity was also minimal (4.83 kN·m), confirming that a timber skeleton alone, without infill, provides inadequate resistance against lateral seismic demands. When adobe (mudbrick) was used as infill, the system demonstrated a moderate increase in strength with $V_{\rm max}$ =908 kN and $K_{\rm initial}$ =38.00 kN/mm,

while achieving a significantly larger ductility ratio (μ =2.50) due to its ultimate displacement of 50 mm. Moreover, adobe exhibited the highest energy dissipation among all configurations (215.13 kN·m), indicating that despite its lower strength, its progressive cracking behavior allows for greater energy absorption and deformation capacity.

Table 2. Seismic performance indicators of timber-framed walls with different infill materials.

Wall configuration	K _{initial} (kN/mm)	V _{max} (kN)	Δ_y (mm)	Δ_u (mm)	$\mu=\Delta_u/\Delta_y$	Energy dissipation (kN.m)
Timber frame + Adobe (mudbrick) infill	38.00	908.0	20.02	50	2.50	215.13
Timber frame + Fired clay brick infill	192.77	3260.9	12.69	50	3.94	27.76
Timber frame + Rubble stone infill	261.60	4345.3	12.46	50	4.01	113.74
Bare timber frame	20.57	385.0	15.04	22.8	1.53	4.83

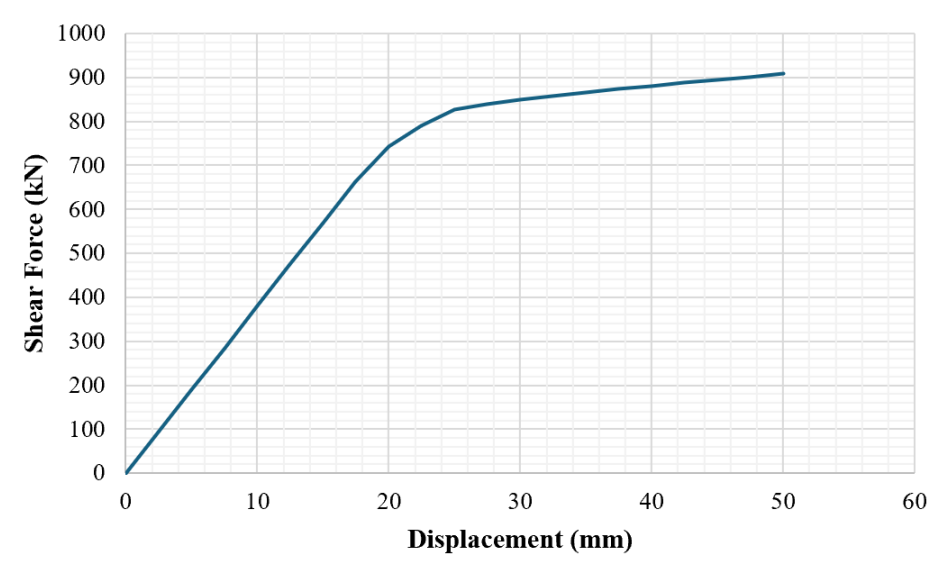


Fig. 5. Pushover curve of the timber frame with adobe (mudbrick) infill.

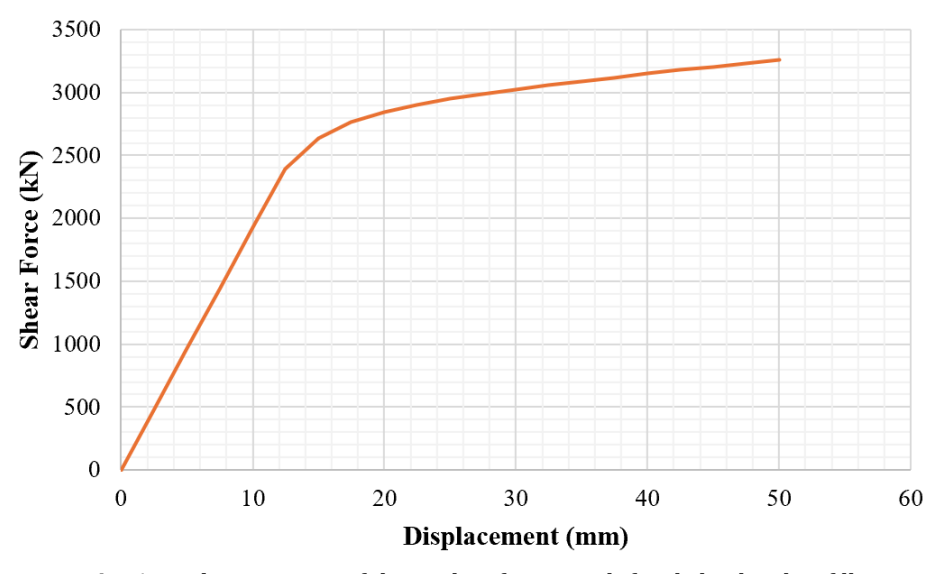


Fig. 6. Pushover curve of the timber frame with fired clay brick infill.

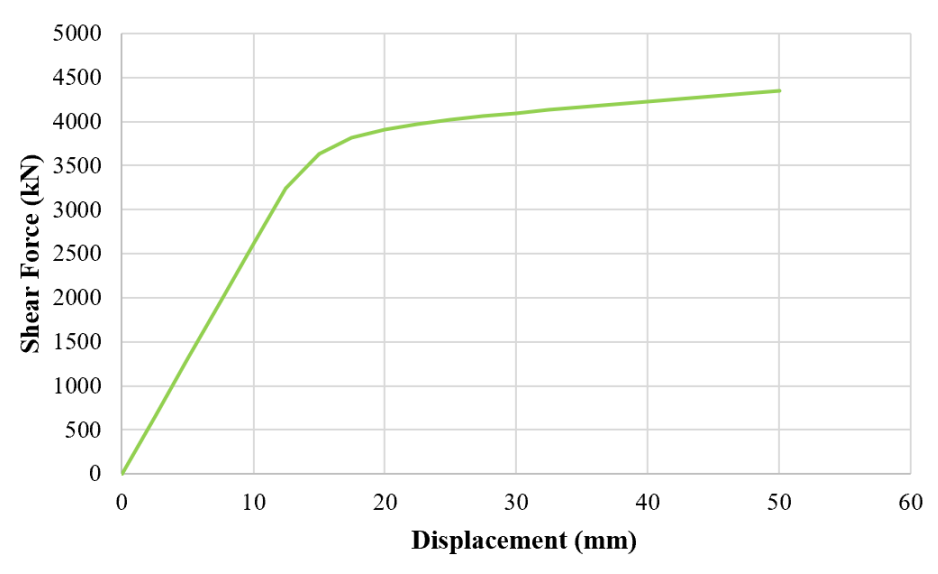


Fig. 7. Pushover curve of the timber frame with natural rubble stone infill.

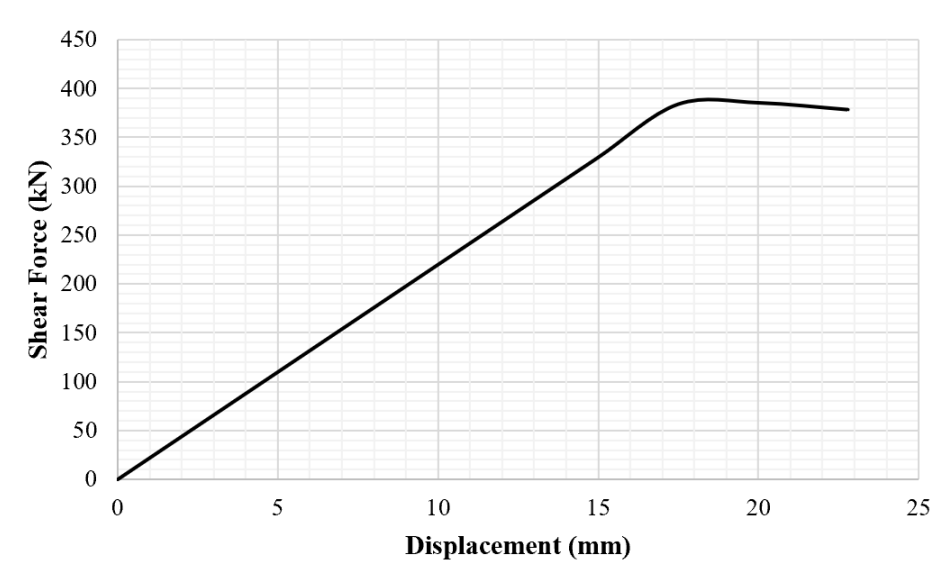


Fig. 8. Pushover curve of the bare timber frame.

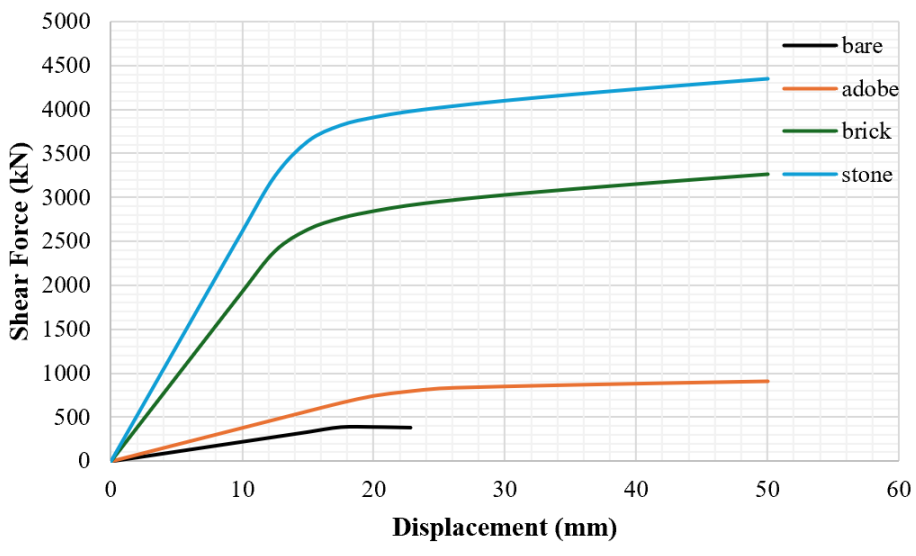


Fig. 9. Force–displacement capacity curves for the wall configurations.

The fired clay brick infill configuration showed a very different pattern. With an initial stiffness of 192.77 kN/mm and a maximum base shear of 3260.9 kN, the brick-infilled wall provided nearly four times the strength of the adobe case (Fig. 10). Its ductility ratio (μ =3.94) was also higher, although the total energy dissipation remained relatively low (27.76 kN·m), pointing to a more brittle failure tendency (Fig. 11). By contrast,

rubble stone infill offered the most balanced seismic performance. It yielded the highest initial stiffness (261.60 kN/mm) and the largest base shear capacity (4345.3 kN), while maintaining a ductility ratio of μ =4.01 with ultimate displacement of 50 mm. Its energy dissipation capacity (113.74 kN·m) was second only to adobe, showing that stone infill can simultaneously provide high strength, stiffness, and considerable energy absorption.

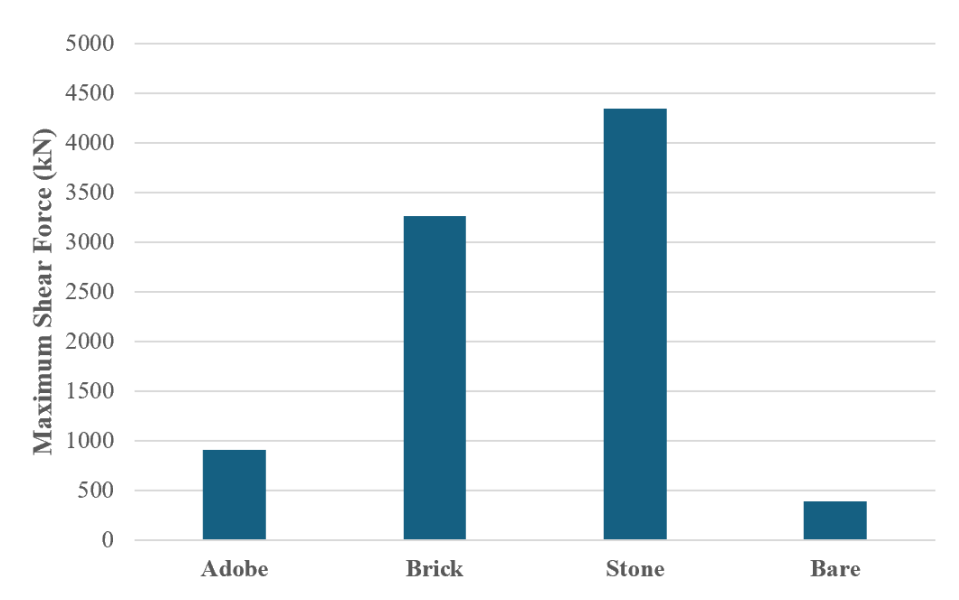


Fig. 10. Maximum shear force results for the wall configurations.

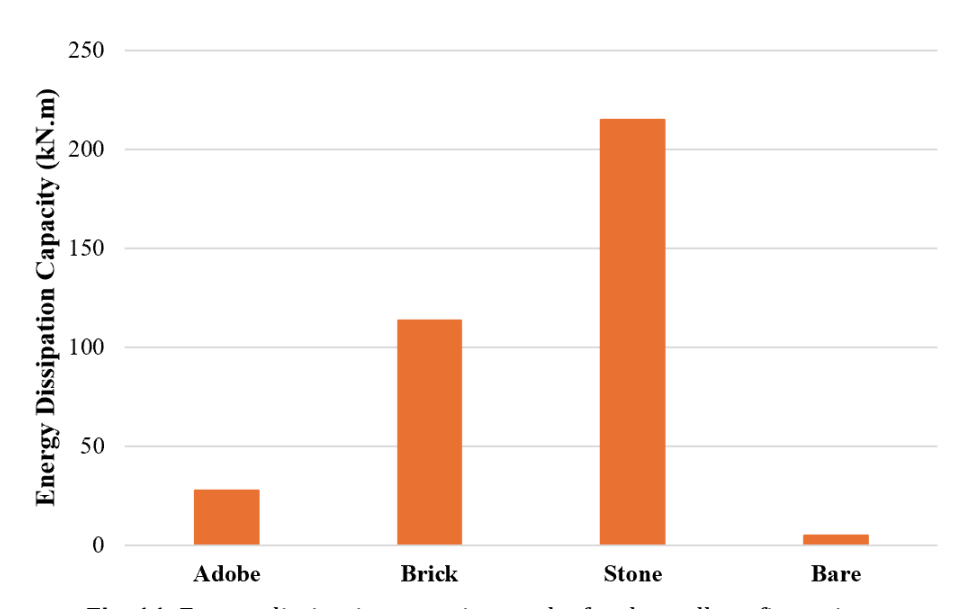


Fig. 11. Energy dissipation capacity results for the wall configurations.

Overall, these findings reveal a distinct trade-off between stiffness and ductility. Adobe infill promotes energy dissipation and ductile behavior but limits lateral strength; fired brick maximizes stiffness and strength at the expense of energy absorption; and rubble stone combines high strength with relatively high ductility, representing the most structurally advantageous configuration. In contrast, the bare timber frame confirms that infill is indispensable for ensuring seismic safety in traditional himis structures.

The failure modes observed in the analyses varied de-

pending on the infill type. In adobe-infilled walls, progressive cracking developed in the panel, while the frame remained engaged until higher drifts, allowing greater ductility. Fired clay brick infill exhibited partial separation at the timber-brick interface, leading to localized sliding and moderate post-peak softening. Rubble stone infill showed brittle crushing and detachment, resulting in a steep strength drop after peak load. In contrast, the bare timber frame exhibited stable but flexible behavior, with deformation concentrated in timber joints and braces (Fig. 12).

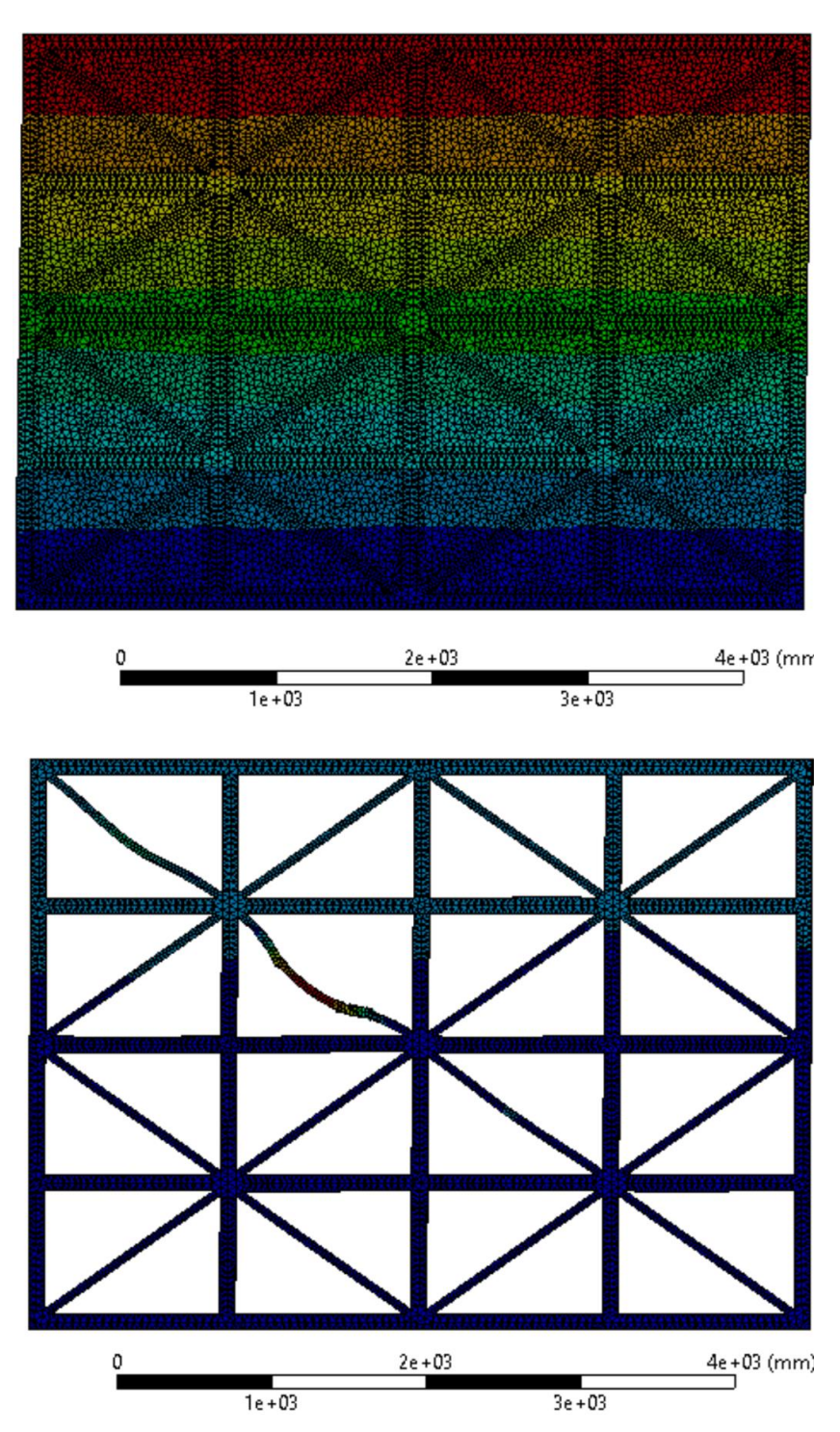


Fig. 12. Structural behavior of the filled and unfilled frames.

5. Conclusions

This study presented a comprehensive seismic performance evaluation of traditional timber-framed (himis) structures with varying infill materials through detailed nonlinear finite element analysis. Four wall configurations were analyzed—bare frame, adobe infill, fired clay brick infill, and rubble stone infill—using 3D pushover analysis in ANSYS Workbench. All materials were modeled with Multilinear Isotropic Hardening plasticity, incorporating frictional contact and geometric nonlinearity to reflect realistic boundary behavior.

The findings revealed that infill materials significantly enhance lateral strength and stiffness but vary widely in terms of ductility and failure mode. Rubble stone provided the highest peak strength but failed in a brittle manner, while fired clay brick offered a more moderate balance between stiffness and ductility. Adobe emerged as the most ductile option, exhibiting high energy dissipation and controlled degradation, making it structurally favorable under large deformations. The bare frame, though weakest, displayed the most stable post-yield behavior and highest drift capacity.

These results underscore the critical influence of infill material properties on the seismic performance of timber-framed systems. In heritage conservation and retrofitting strategies, strength enhancement through infill must be balanced with the need for ductile and energy-dissipating behavior. The numerical framework established in this study allows for effective comparison of different infill typologies under consistent conditions and contributes to the development of performance-based approaches for the preservation and rehabilitation of historic himis buildings in seismic regions.

From a practical perspective, the findings of this study highlight that retrofit strategies for existing himis buildings should carefully consider the choice of infill material. While rubble stone provides higher strength, adobe infill ensures greater ductility and energy dissipation, which is more desirable for seismic safety. In heritage conservation projects, retrofitting approaches should therefore aim not only to strengthen these systems but also to preserve or enhance their ductile performance characteristics.

Acknowledgements

None declared.

Funding

The author received no financial support for the research, authorship, and/or publication of this manuscript.

Conflict of Interest

The author declared no potential conflicts of interest with respect to the research, authorship, and/or publication of this manuscript.

Author Contributions

The author confirms sole responsibility for all aspects of the study including conception and design, acquisition of data, analysis and interpretation of data, drafting the manuscript, revising it critically for important intellectual content; and gave final approval of the version to be published.

Data Availability

The datasets created and/or analyzed during the current study are not publicly available, but are available from the corresponding author upon reasonable request.

REFERENCES

- Aktaş YD (2017). Seismic resistance of traditional timber-frame hımış structures in Turkey: A brief overview. *International Wood Products Journal*, 8(sup1), 21-28.
- Dikmen N (2010). An investigation on traditional timber-framed buildings in Çankırı province of Turkey. *Trakya University Journal of Science*, 11(1), 15-27.
- Dima DI, Dutu A (2016). Traditional buildings with timber frame and various infills in Romania. *Proceedings of the WCTE 2016 World Conference on Timber Engineering*, Vienna, Austria, August 22-25, 1-9
- Dutu A, Niste M, Spatarelu I, Dima DI, Kishiki S (2018b). Seismic evaluation of Romanian traditional buildings with timber frame and mud masonry infills by in-plane static cyclic tests. *Engineering Structures*, 167, 655-670.
- Gani A, Banday JM, Rai DC (2024). Seismic behavior of timber-framed structures infilled with dry brick masonry. *Bulletin of Earthquake Engineering*, 22(13), 6419-6446.
- Karaman ÖY, Zeren MT (2015). Case study: Examples of wooden vernacular architecture Turkish houses in Western Anatolia. YBL Journal of Built Environment, 3(1-2), 77-87.
- NAVFAC DM7-02 (1982). Foundations and Earth Structures. Naval Facilities Engineering Command, Alexandria, VA, USA.
- Qu Z, Fu X, Kishiki S, Cui Y (2020). Behavior of masonry infilled Chuandou timber frames subjected to in-plane cyclic loading. *Engineering Structures*, 211, 110449.
- Tan W, Zhou T, Zhu L, Zhao X, Yu W, Zhang L, Liang Z (2024). Seismic performance of a single-story timber-framed masonry structure strengthened with fiber-reinforced cement mortar. *Materials*, 17(15), 3644.
- Vieux-Champagne F, Sieffert Y, Grange S, Polastri A, Ceccotti A, Daudeville L (2014). Experimental analysis of seismic resistance of timber-framed structures with stones and earth infill. *Engineering Structures*, 69, 102-115.



Research Article

Nonlinear in-plane response of 3D-printed concrete walls with varied infill patterns: Experimental mix design and numerical structural assessment

İsmail Hakkı Tarhan ^{a,*} 📵, Yeşim Tarhan ^b 📵

ABSTRACT

This study investigates the nonlinear in-plane structural behavior of 3D-printed concrete wall elements with two representative internal infill patterns – lattice (L) and triangular (T) - using finite element modeling informed by experimentally derived material properties. A printable concrete mixture was specifically developed using CEM I 42.5 R Portland cement, silica sand, and hydroxypropyl methylcellulose (HPMC) as a viscosity-modifying agent. Conventional cast specimens (40×40×160 mm³) achieved a 28-day flexural strength of 8.7 MPa and a compressive strength of approximately 63 MPa. Nonlinear behavior of wall panels with both infill types was investigated using numerical methods with advanced constitutive laws. These models account for the distinct compressive-tensile response of concrete and damage evolution under monotonic lateral loading, allowing assessment of the influence of geometry on load-bearing capacity and failure mechanisms. The results reveal that both infill patterns exhibit nonlinear load-displacement responses with an initial elastic regime, an early localized cracking peak, followed by a notable recovery in load-bearing capacity, and subsequently a global peak load prior to progressive postpeak softening. While the overall performance of both infill types was comparable, the T pattern exhibited a marginally higher peak load (1.7-2.7%) and improved ductility relative to the L form. These distinctions are attributed to the T-pattern's more efficient diagonal force transfer and the development of a single continuous diagonal shear band, as opposed to the L-pattern's multiple discontinuous cracks and broader damage zones.

ARTICLE INFO

Article history:

Received – July 21, 2025 Revision requested – August 20, 2025 Revision received – August 28, 2025 Accepted – September 3, 2025

Keywords:

3D concrete printing In-plane behavior Nonlinear analysis Structural wall members Infill geometry Failure mechanism



This is an open access article distributed under the CC BY licence.
© 2025 by the Authors.

Citation: Tarhan İH, Tarhan Y (2025). Nonlinear in-plane response of 3D-printed concrete walls with varied infill patterns: Experimental mix design and numerical structural assessment. Challenge Journal of Structural Mechanics, 11(3), 160–173.

1. Introduction

Three-dimensional printing (3DP) technology, also known as additive manufacturing, is rapidly transforming the construction industry by enabling complex, customized components to be fabricated directly from digital models - eliminating conventional formwork, streamlining construction, and reducing material waste (Labonnote et al. 2016; Maskuriy et al. 2019; Scheurer et al.

2020; Tarhan et al. 2024a; Mohamed and Mohamed 2025). Notable projects include Dubai's "Office of the Future" – the world's first fully functional 3D-printed office (Fig. 1(a,b)) – printed on site in just 17 days, achieving nearly 50% reductions in labor and material costs (Archdaily 2019; Hossain et al. 2020). In China, WinSun Company demonstrated the speed and efficiency of 3D construction by producing ten single-story homes in Suzhou within 24 hours (Fig. 1(c)). The company also con-

^a Department of Civil Engineering, Tokat Gaziosmanpaşa University, 60150 Tokat, Türkiye

^b Technical Sciences Vocational School, Ardahan University, 75000 Ardahan, Türkiye

^{*} Corresponding author. Tel.: +90-356-252-1616; E-mail address: ismailhakki.tarhan@gop.edu.tr (İ. H. Tarhan) ISSN: 2149-8024 / DOI: https://doi.org/10.20528/cjsmec.2025.03.005

structed a five-story apartment building (Fig. 1(d)) and a 1,100 m² villa using 3D-printed concrete components (Fig. 1(e)). These projects achieved 30–60% reductions

in material waste and up to 70% shorter build times compared to traditional methods (Winsun3d 2015; Zoey 2018; Hossain et al. 2020).



Fig. 1. Examples of large-scale 3D-printed concrete construction: (a),(b) Dubai "Office of the Future" printed by Apis Cor (Archdaily 2019); (c) Single-story houses by WinSun (Architectsjournal 2014); (d) WinSun's five-story apartment building (Winsun3d 2015); (e) Interior corridor of a 3D-printed villa (Zoey 2018).

In addition to these widely recognized benefits, 3D printing allows for the precise replication of historic or ornamental components, as seen by a recent review study (Tarhan and Tarhan 2025). The unique nature of additive manufacturing also opens the door to further possibilities. For instance, the technology may facilitate the seamless integration of multi-functional features, such as embedded sensors or service conduits, directly during fabrication. Its flexibility enables on-demand construction in remote or disaster-affected regions. Furthermore, the ability to locally tailor material composition and geometry presents opportunities for functionally graded elements and resource-efficient, performance-based design. While many of these possibilities remain aspirational in current practice, they represent promising directions for future research and innovation in digital construction.

Despite significant progress in the development of 3D-printable cement-based mixtures with suitable rheological and mechanical properties (Perrot et al. 2016; Rahman et al. 2024; Tarhan et al. 2024b; Zafar et al. 2025), the widespread use of 3D-printed concrete in structural construction is still hindered by several unresolved challenges at the building scale. One of the major

limitations in layer-by-layer fabrication is the challenge of effectively integrating reinforcement into the printed matrix (Bos et al. 2016; Panda et al. 2018). Traditional steel rebars and meshes are difficult to position continuously, prompting research into alternatives such as robotic bar placement synchronized with the print head (Mechtcherine et al. 2021; Nan et al. 2025), interlayer meshes for enhanced crack control (Ramesh et al. 2024; Tarhan et al. 2024b), direct fiber incorporation (steel, glass, polymer) (Christ et al. 2015; Hambach et al. 2019; Le et al. 2012), and even natural fibers like jute for sustainable earth-based mixes (Tarhan et al. 2024b, 2025a), are being explored, suggesting that natural fibers may also enhance ductility and sustainability in cementitious 3D-printed mixtures. Although promising, each strategy presents its own integration and performance challenges - especially when considered alongside the unique properties and behaviors introduced by additive manufacturing.

Another critical and often overlooked issue is the role of internal infill geometry in the structural performance of 3D-printed elements. Unlike conventional cast concrete, 3D-printed components exhibit pronounced anisotropy, interfacial weaknesses between layers, and a

strong dependency on the specific infill pattern employed (Dey et al. 2023; Panda et al. 2018; Wangler et al. 2016; Yang et al. 2023).

Recent research addressing infill pattern of 3D-printed concrete structural elements can be systematically classified into four main categories based on the loading conditions and performance criteria addressed: (i) fire and thermal performance (AlZahrani et al. 2022; Chamatete and Yalçınkaya 2024; Dziura et al. 2023; Hanifa et al. 2025; Suphunsaeng et al. 2025), (ii) axial compressive performance (Han et al. 2022; Khanverdi and Das 2025; Kumar et al. 2025; Zhang et al. 2025a, 2025b), (iii) out-of-plane structural behavior (Aghajani Delavar et al. 2024; Dey et al. 2023; Hernández Vargas et al. 2024) and (iv) in-plane structural behavior (Aghajani Delavar et al. 2024; Warsi et al. 2025a, 2025b).

Regarding fire and thermal performance, recent studies primarily address the optimization of infill geometries in 3D-printed walls for enhanced insulation. Hanifa et al. (2025) experimentally demonstrated that optimized earthen wall segments featuring carefully designed "infinite" cavity patterns achieved a high thermal resistance (R-value $\approx 1.194 \text{ m}^2 \cdot \text{K/W}$) while maintaining structural compressive strength above 4 MPa. Similarly, Dziura et al. (2023) experimentally validated that cellular concrete walls incorporating PUR-foam cavity infills significantly improved thermal insulation performance, achieving a U-value as low as 0.183 W/m²·K, thus meeting stringent Polish building codes without requiring additional insulation layers. Chamatete and Yalçınkaya (2024) numerically showed that lattice infills combined with granular insulation materials (Expanded Polystyrene (EPS) beads, perlite) reduced thermal transmittance by approximately 26-44%; however, efficiency was highly sensitive to filament width, web length, and thermal bridging at shell connections. AlZahrani et al. (2022) numerically optimized multiple infill geometries (square, triangular, hexagonal, rectangular, diamond), revealing that carefully selected shapes significantly lowered effective thermal conductivities (0.122-0.170 W/m·K) compared to conventional masonry and translated into tangible energy savings. Lastly, Suphunsaeng et al. (2025) performed full-scale fire resistance tests on printed concrete walls with varying cavity arrangements, concluding thicker walls with solid concrete infill filaments had superior insulation ratings under a 3-hour ISO-834 fire exposure, and provided validated numerical models to inform design charts linking wall thickness and cavity geometry to thermal performance.

Recent axial compressive behavior studies on 3D-printed walls have highlighted key influences of reinforcement, openings, and infill geometry on structural performance. Han et al. (2022) experimentally tested full-scale printed walls incorporating internal W-shaped truss infill and horizontal steel reinforcement, reporting an unexpected 25% strength reduction due to the reinforcement layers acting as weak planes; they proposed an analytical model to accurately predict axial capacity. Khanverdi and Das (2025) examined the axial performance of full-scale printed walls with vertical reinforcement and a large window opening, showing vertical rebars enhanced ultimate load by 14–26%, tripled energy

absorption, and shifted failure modes from brittle vertical cracking toward localized crushing, whereas openings modestly reduced capacity (~20%). Kumar et al. (2025) conducted a detailed numerical investigation on the axial compressive (vertical in-plane) response of 3Dprinted concrete walls with different internal lattice geometries, using a coupled Concrete Damaged Plasticity and cohesive-zone modeling framework. To systematically assess the role of internal geometry, they adopted the L-, T-, and LT-type infill patterns originally optimized by Dey et al. (2023) for out-of-plane flexural performance, and applied them under pure axial compression. Their results demonstrated that increasing compressive strength shifts damage from filaments to interfaces, while higher interface shear strength delays instability; among the geometries, larger filament-wall contact (Ltype) enhanced load capacity and delayed cracking. Zhang et al. (2025b) explored the influence of filamentcontact patterns in 2-D infill geometries, revealing that rectangular infills with material overlaps retained stiffness and strength, while honeycomb patterns (pointcontact between layers) experienced up to 45% strength loss due to premature vertical-layer buckling.

The studies on out-of-plane (flexural) performance of 3D-printed concrete have highlighted the significant influence of infill topology and optimized geometry on structural efficiency. Hernández Vargas et al. (2024) introduced a stress-driven internal topology optimization method, locally adjusting the filament width within concrete beams (700×100×100 mm) according to calculated stress distributions. Their approach was experimentally validated via three-point bending tests, clearly demonstrating a 47-63% higher flexural strength-to-weight ratio compared to beams produced using a conventional uniform (zig-zag) infill pattern, highlighting geometryguided thickness variation as a viable strategy to enhance structural capacity and reduce material use simultaneously. Similarly, Dey et al. (2023) experimentally evaluated the flexural behavior of four concrete beams (890 mm length) printed with different lattice-based infills (lattice, triangular, lattice-triangular, and sinusoidal), subjected separately to vertical and transverse three-point bending tests. Their experimental and numerical investigations indicated that triangular infills provided the highest transverse flexural strength (~11.5 kN) and about 30% greater stiffness compared to lattice infills, while subsequent numerical optimization identified a 25% horizontal-to-triangular web-length ratio as optimal for maximizing strength-to-weight efficiency. Finally, addressing specifically wall-scale structures, Delavar et al. (2022) analytically and numerically investigated the outof-plane flexural capacity of slender 3D-printed walls, developing closed-form design equations validated against nonlinear finite-element shell-beam models of four wall prototypes. Their results showed that infill layout directly governed whether failure occurred through oneway or two-way bending mechanisms,

Lastly, in-plane (lateral) structural behavior - crucial for seismic performance - has only recently begun to attract focused research on shear strength, energy dissipation, and seismic resilience. Delavar et al. (2024) analytically and numerically investigated reinforced concrete-

framed 3D-printed walls under quasi-static lateral loading, concluding that the presence of infill patterns increases lateral strength mainly due to an increased cross-sectional area, while the specific type of infill pattern had only a limited impact on overall lateral strength. Warsi et al. (2025b) developed a finite-element composite micro-model combining Concrete Damaged Plasticity (CDP) and cohesive-zone modeling for interlayer interfaces, demonstrating that reducing wall height-towidth ratios, integrating edge columns, and providing continuous reinforcement significantly enhanced lateral strength (~30%), stiffness, and energy dissipation. Additionally, Warsi et al. (2025a) numerically assessed earthquake-resistant design methodologies for hollow 3Dprinted walls based on ACI 318-19 and Eurocode 8 provisions, showing that double-layer reinforcement improved lateral load capacity by approximately 31%, ductility (μ =4.36 versus 4.01), and strain distributions compared to single-layer reinforcement layouts, emphasizing the critical interaction between reinforcement arrangement and internal infill geometry for optimized seismic performance.

Collectively, these studies highlight that internal infill topology, interlayer interface quality, and reinforcement detailing significantly influence the nonlinear behavior and seismic capacity of 3D-printed concrete walls; however, to the best of the authors' knowledge, the nonlinear in-plane performance of unreinforced 3D-printed concrete walls with different infill patterns remains entirely unexplored, leaving a major gap in understanding their failure evolution and ultimate lateral resistance.

To address this gap, the present study systematically evaluates the nonlinear in-plane response of unreinforced 3D-printed concrete walls incorporating different infill geometries - named as lattice (L) and triangular (T). Infill forms previously introduced and geometrically optimized by Dey et al. (2023) for out-of-plane flexural behavior - and subsequently employed by Kumar et al. (2025) for axial compression analysis - are adopted here to systematically investigate their effects under in-plane lateral loading, enabling direct comparison across different structural scenarios. A high-performance, 3D-printable cementitious mix was specifically developed and experimentally characterized, and its measured properties directly informed the nonlinear finite element models.

Thus, the current investigation uniquely addresses this research gap, examining how infill patterns impact the overall nonlinear response, stiffness degradation, damage evolution, and ultimate capacity of structural 3D-printed concrete walls under in-plane lateral loading condition. The findings provide the first comparative insights into the role of complex internal geometry on the in-plane structural behavior of unreinforced 3D-printed walls – delivering essential knowledge for the development of next-generation, high-performance digital construction systems.

2. Materials and Methods

This section details the development and characterization of a high-performance, 3D-printable cementitious mixture tailored for digital construction applications. The experimental program includes the optimization of mix composition, followed by a comprehensive assessment of its fresh and hardened mechanical properties. These experimentally determined parameters form the basis for subsequent nonlinear finite element simulations, enabling a realistic evaluation of wall-scale structural performance. The adopted numerical modeling strategy, implemented in Abaqus, utilizes the Mohr-Coulomb failure criterion and explicitly accounts for the distinct tensile and compressive behavior of concrete. The specific infill patterns, selection rationale, and geometric configurations of the wall models are also described in detail.

2.1. Development of 3D-printable cementitious mix

The cement-based mixture used for 3D printing in this study was developed to offer extrudability and good mechanical performance. The materials and mixture details are presented in Tarhan et al. (2025b). It consisted of CEM I 42.5 R Portland cement, ground granulated blast furnace slag (GGBS), plaster (TRADICAL-PF-80 branded), metakaolin clay, fine quartz sand (0–2 mm), water, a polycarboxylate ether-based superplasticizer (SP) and hydroxypropyl methylcellulose (HPMC) as a viscosity-modifying agent. The proportions for 1 m 3 of the mixture are presented in Table 1.

Table 1. Mix proportions of the printable concrete.

Materials	CEM I 42.5 R Portland cement	GGBS	Plaster	Metakaolin clay	Sand 0–0.5 mm	Sand 0.5–2 mm	Water	SP	НРМС	Air content
Amount (kg)	300	100	100	25	535.8	831.2	200	7.5	0.6	%1

The cement-based mixture was prepared by mixing all the dry ingredients, including cement, aggregate, GGBS, gypsum, clay and methyl cellulose, together at low speed for one minute. Water was then added in two stages, with the plasticiser mixed into the second portion. Mixing continued for a further two minutes. After a short rest period, the mixture was mixed at high speed for a further two minutes, bringing the total mix-

ing time to approximately six minutes. Continuous mixing was used to minimise the risk of premature setting. Penetration depth tests were initially performed to assess printability, but the final mixture was selected based on actual 3D printing trials to ensure suitability. Prismatic samples measuring $40\times40\times160$ mm were cast in molds for flexural and compressive strength testing. After curing for one day under ambient laboratory

conditions, the specimens were demolded and placed in a controlled curing chamber at 20±3 °C with 80% relative humidity until the day of testing, following the approach adopted also in Tarhan et al. (2024b). Meanwhile, 3D-printed samples measuring 110×110×350 mm were fabricated to demonstrate the printability of

the developed mix in terms of its rheological performance.

The 3D printing process was carried out using a Delta WASP 3DMT printer with a 3 cm nozzle operating at a speed of 2 cm/s. Fig. 2 shows the 3D printing process and representative views of the printed layers.



Fig. 2. 3D printing of test samples using a Delta WASP 3DMT printer:
(a) Extrusion of successive layers during printing; (b) Side view of the printed layers with height measurement; (c) Top view of the printed layers with width measurement.

2.2. Experimental characterization of printable concrete

The printable mixture was formulated to ensure adequate buildability and extrusion stability, taking into account the specific rheological demands of layer-by-layer deposition. Key fresh-state parameters were assessed immediately after mixing in order to capture the time-dependent behavior of the material.

The properties of the cement-based mortar in its fresh state were evaluated through a series of standardized tests. Density was measured according to BS EN 12350-6 (2019) and rheological behavior was assessed using a rotational rheometer with four-blade vane geometry. A constant shear rate of $0.05~\rm s^{-1}$ was applied for 200 seconds and the peak torque at flow onset was used to determine the static yield stress, which affects the material's printability and ability to retain its shape. To mon-

itor structuration over time, rheological measurements were repeated at defined intervals. Additionally, the structural build-up was examined using the fall cone penetration method in accordance with CEN ISO 17892-6:2017. The penetration depth of an 80 g, 30° cone dropped into fresh mortar served as an indicator of evolving shear resistance and thixotropic behavior. These combined tests provided insight into the time-dependent characteristics of the mixture, which are critical for ensuring adequate buildability and interlayer adhesion in 3D printing applications.

For material characterization, mold-cast prism specimens were evaluated for mechanical testing. Flexural strength was determined via three-point bending tests on prism specimens with nominal dimensions of $40\times40\times160$ mm, in accordance with TS EN 12390-5 (2019). Following test, the broken halves were tested for compressive strength in accordance with TS EN 12390-3 (2019).

2.3. Numerical modeling approach

The in-plane structural performance of the 3D-printed concrete walls was assessed using nonlinear finite element simulations performed in Abaqus (Abaqus 2022). A macro modeling strategy was adopted, wherein the layered filament architecture of the walls was treated as a homogenized continuum. All solid regions, including the outer wall regions and infill forms, were discretized using four-node linear tetrahedral elements (C3D4). This element type was selected for its suitability with complex geometries, effectiveness in capturing the localized cracking and post-peak softening typical of brittle materials, while maintaining computational efficiency.

The material nonlinearity was represented by the CDP model, which is well established for simulating the inelastic behavior of concrete and similar quasi-brittle materials (Sümer and Aktaş 2015). The CDP model integrates the effects of tensile cracking and compressive crushing by combining plasticity with progressive damage mechanics. The deviatoric yield surface is defined by K_c =2/3, which corresponds to the Mohr–Coulomb criterion in the deviatoric plane (Fig. 3).

Distinct tensile and compressive responses are defined through separate stress–strain relationships for each loading mode. The progressive accumulation of microcracks under tension and crushing damage under compression is tracked using two independent scalar damage variables, d_t and d_c , which reduce the material's elastic modulus with increasing strain, thereby realisti-

cally capturing stiffness degradation. In tension, the model captures the linear elastic response up to the tensile strength, followed by strain-softening due to crack development. In compression, the response includes an initial linear regime, limited hardening, and subsequent exponential softening after peak stress (Fig. 4).

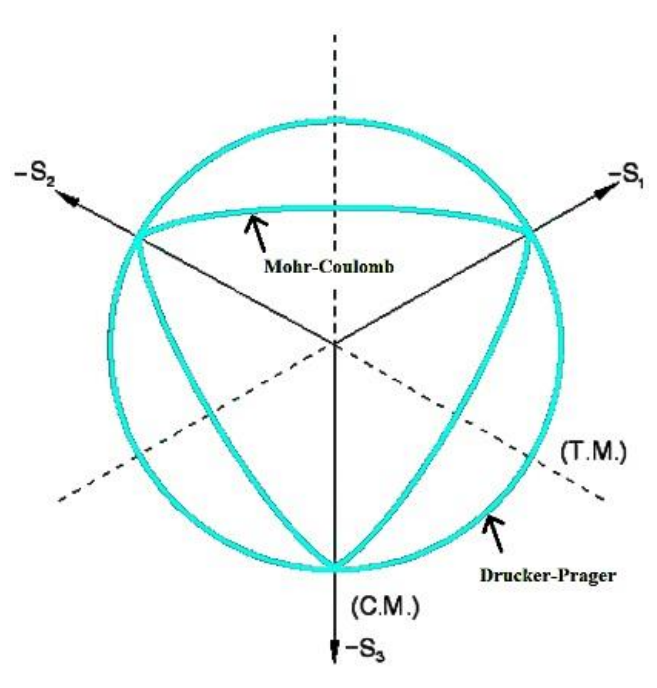


Fig. 3. Deviatoric yield surfaces for Mohr–Coulomb $(K_c=2/3)$ and Drucker–Prager $(K_c=1)$ criteria.

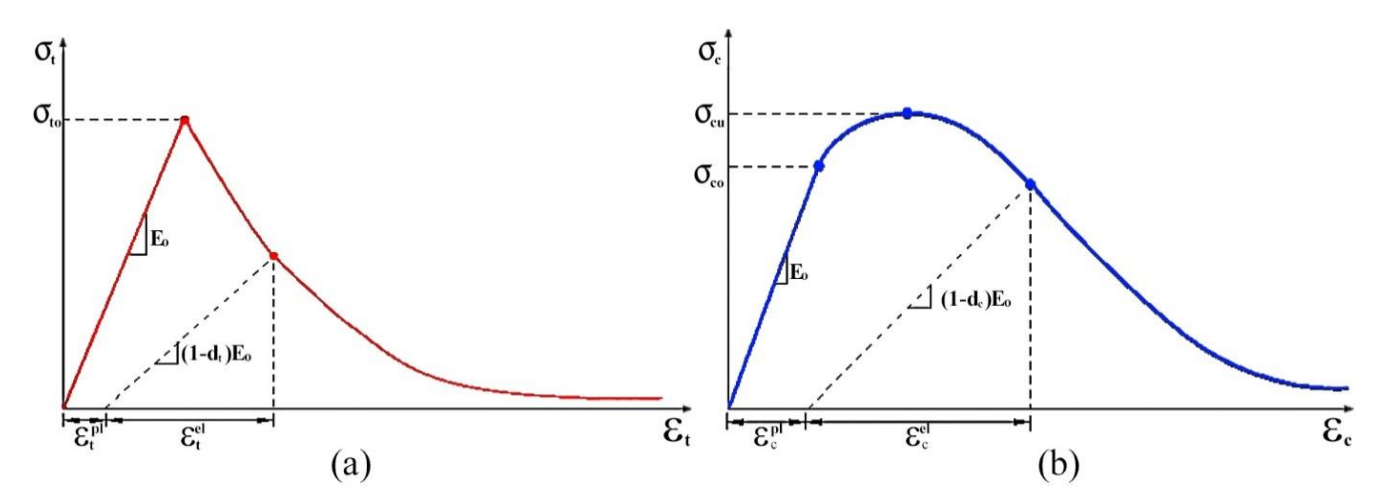


Fig. 4. Material response under (a) tension and (b) compression.

Additional CDP input parameters included a dilation angle of 30°, flow potential eccentricity of 0.1, and a biaxial-to-uniaxial compressive strength ratio of 1.16, reflecting common practice for concrete (Lubliner et al. 1989; Tarhan 2025a). To aid convergence in the postpeak regime, a small viscosity parameter of 0.0001 was introduced, which has negligible effect on the global structural response but improves numerical stability in the softening range (Abaqus 2022; Tarhan 2025b). Material properties (Table 2) and nonlinear constitutive parameters were directly obtained from the experimentally validated cementitious mix, as detailed in Sections

2.1 and 3.1. The direct tensile strength (f_t) of the concrete was estimated as half of the measured flexural strength. The CDP model parameters were implemented as described above, with no further calibration.

2.4. Infill pattern selection, description and wall models

In this study, geometric models of the 3D-printed concrete walls were developed to include both outer wall regions and two distinct internal infill patterns: lattice (L) and triangular (T). These forms were originally intro-

duced and optimized for out-of-plane flexural efficiency by Dey et al. (2023) and later utilized by Kumar et al. (2025) in axial compression studies. By adopting these well-established patterns, the present work contributes complementary insights into their structural performance under in-plane monotonic lateral loading thereby extending the existing knowledge base to encompass a broader range of loading conditions and enabling a more comprehensive understanding of their behavior in digital construction applications (Fig. 5).

		M	lechanical properties			
Density (kg/m	1 ³) Youn	g's modulus (MPa)	Poisson's ratio	f _c (MPa)	$f_t(MPa)$	
2,150		37,318	0.2	63	4.3	
			Plasticity definition			
Dilation angle Eccentricity			f_{b0}/f_{c0}	K_c	Viscosity parameter	
30°		0.1	1.16	0.667	0.0001	
	Stress-inelastic	strain relationships	Damage definition			
Compressive		Tensile		Tension		
Yield stress	Inelastic strain	Inelastic strain Yield stress		Damage parameter	Cracking strain	
20	0	4.3	0	0	0	
40	0.0012	0.43	0.003	0.9	0.003	
55	0.002	-	-	-	-	
63	0.0032	0.0032 –		-	-	
50	0.0075	_	_	-	-	
31	0.012	_	_	-	-	
10	0.017	0.017				

Table 2. Adopted material properties.

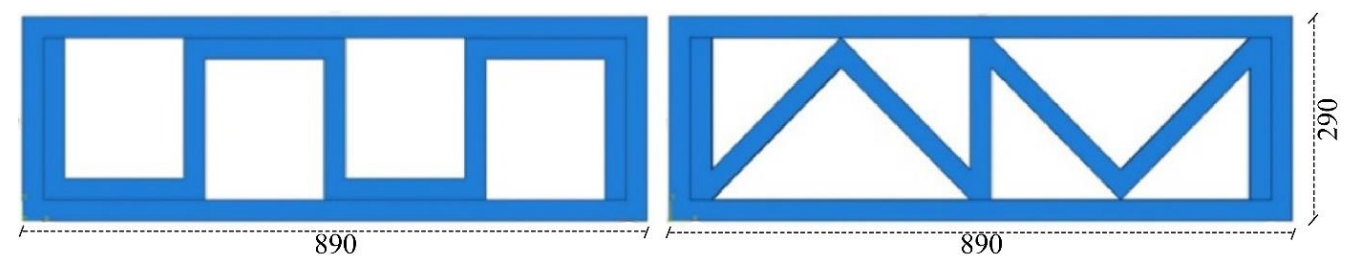


Fig. 5. Schematic representations of the two 3D-printed concrete wall models with different internal infill patterns: (left) L and (right) T adapted from Dey et al (2023) (all dimensions are in millimeters).

All wall geometries were created in SolidWorks and subsequently imported into Abaqus for numerical modeling. Walls were defined with a cross-sectional size of 890 mm×290 mm, consistent with the reference configuration adopted by Dey et al. (2023) (Fig. 5). The layer width and height were 30 and 20 mm, respectively, reflecting the printing process of the experimentally produced mix and ensuring compatibility with common extrusion-based 3D printing processes. An aspect ratio (height to width) of approximately 1:0.5 was adopted, resulting in a total of 85 layers per wall (Fig. 6) - matching the practical constraints and design parameters addressed in Sections 2.1 and 2.2.

According to the adopted macro modeling approach, all interfaces between deposited filaments within a layer, as well as between successive layers, were inherently assumed fully bonded. This means that potential interlayer weaknesses were not explicitly modeled in this study. Such simplification reflects both the cohesive quality ob-

served in the developed 3D-printable mix and prevailing practice in comparable numerical studies. By excluding interface imperfections, the numerical model isolates the structural influence of infill geometry, thereby establishing a benchmark for future studies where interlayer bonding effects may be directly incorporated.

Finite element meshes were generated using four-node linear tetrahedral elements (C3D4), which enabled accurate representation of the complex internal geometries of the wall models (see Fig. 7 for mesh illustration). To assess the influence of mesh dependency on the simulation results, two different mesh densities were employed: a fine mesh with an average element size of 15 mm and a medium mesh of 30 mm. The L-wall models contained 28801 nodes and 126464 elements with the medium mesh and 91481 nodes and 458348 elements with the fine mesh, while the T-wall models contained 35480 and 73567 nodes with 114272 and 280877 elements, respectively.

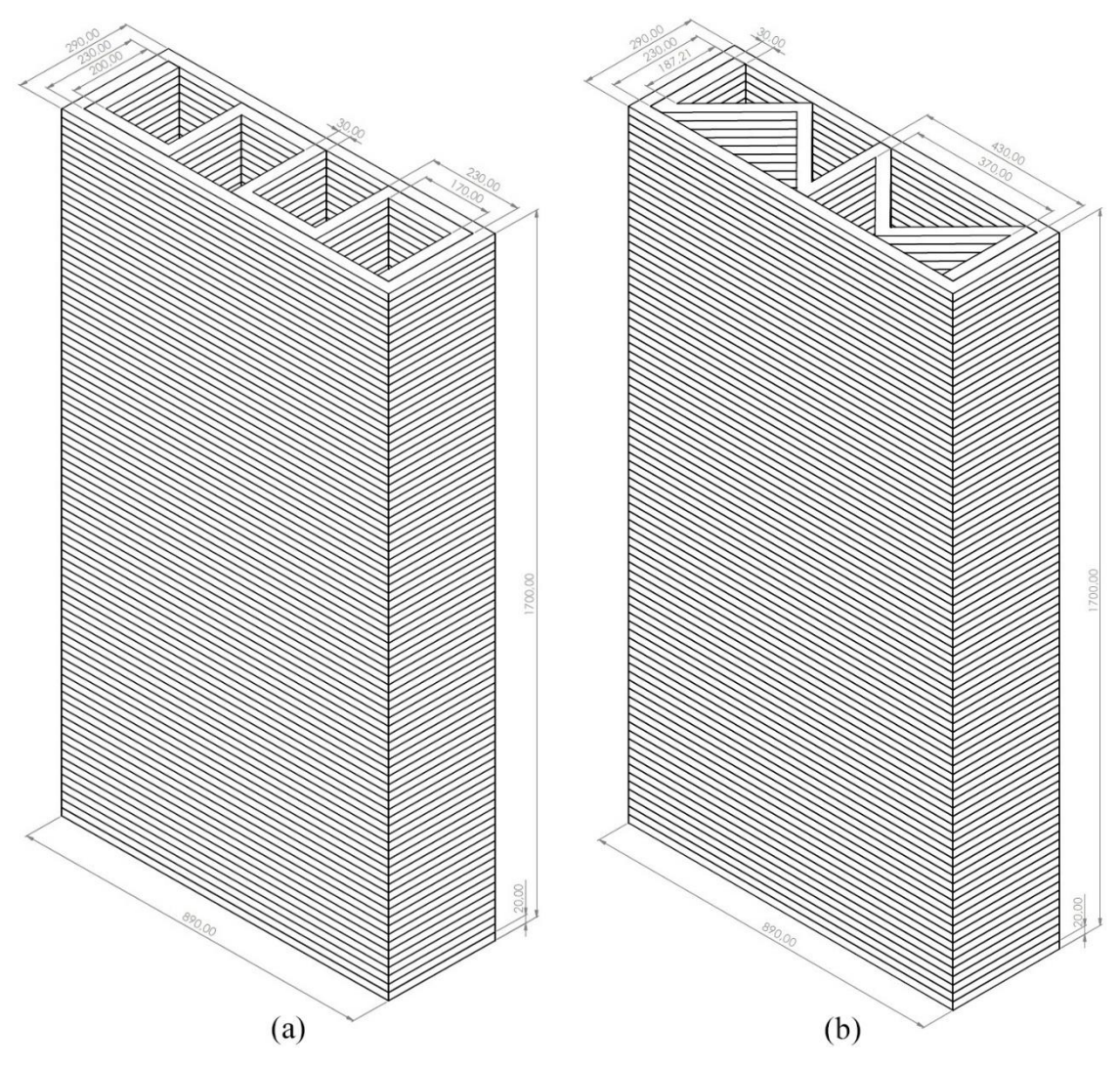


Fig. 6. Three-dimensional CAD views of the 3D-printed wall panels with (a) L and (b) T internal infill patterns (all dimensions are in millimeters).

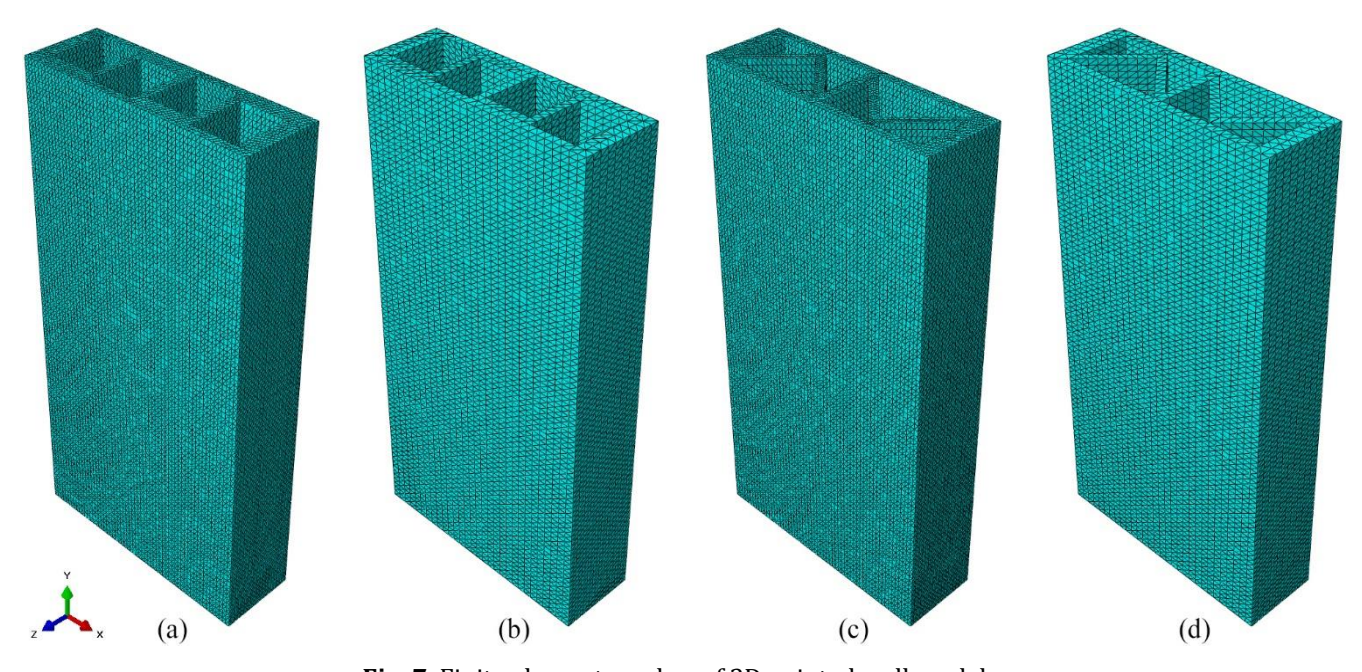


Fig. 7. Finite element meshes of 3D-printed wall models: (a,b) L pattern with fine and medium mesh densities; (c,d) T pattern with fine and medium mesh densities. All meshes are created using four-node linear tetrahedral elements (C3D4).

In the initial step, boundary conditions were defined: the bottom surface of each wall - including both outer wall regions and infill - was fully fixed (encastre) to represent a rigid foundation, restraining all translational and rotational degrees of freedom. At the top edge, all rotational degrees of freedom and translation in the out-ofplane direction (*Z*) were restricted, while horizontal translation in the loading direction (X, in-plane) and vertical translation (Y, wall height) were left free to allow realistic deformation during loading. Numerical simulations were performed in three consecutive analysis steps to capture realistic loading conditions. First, gravity loading was applied to each wall to account for selfweight. In the second step, an additional vertical precompressive load - equal to the calculated self-weight of the wall (4,350 N for the T-pattern, 4,378 N for the L-pattern, based on a measured density of 2.15 g/cm³) - was applied uniformly over the top surface. This step simulated the scenario where the wall supports another identical story above. In the final step, a monotonic lateral displacement was incrementally imposed at the top surfaces until global failure was reached.

3. Results and Discussion

3.1. Fresh and hardened properties of concrete

At the beginning of the testing process, the cement-based mortar had a unit weight of $2.15~\rm g/cm^3$, which indicates that it is a dense, well-compacted mixture that is suitable for structural applications. The penetration depth measured by the fall cone test was $19.74~\rm mm$, reflecting a moderate level of thixotropy and structural build-up in the early stages. Rheological characterization using a rotational rheometer yielded a peak torque of $9.4~\rm mNm$ at a shear rate of $0.05~\rm s^{-1}$, corresponding to the static yield stress of the mix. These values confirm that the mortar possesses adequate resistance to deformation while maintaining sufficient flowability for extrusion-based 3D printing.

The cement-based printable mortar exhibited rapid strength development, with compressive strength in-

creasing from 10.96 MPa at 1 day to 53.75 MPa by day 14 and reaching 62.89 MPa at 28 days. This places the mix in the TS EN 206+A2 (2021) strength class C50/60, indicating its classification as a high-performance mortar. Such rapid hardening is typical of low water-to-binder ratio mixtures with reactive fillers and ensures early load-bearing capacity for successive layers. Flexural strength rose from 3.93 MPa at 1 day to 8.70 MPa at 28 days, demonstrating adequate tensile resistance comparable to engineered 3D-printed mortars reported in the literature.

3.2. Nonlinear in-plane behavior of 3D printed concrete walls

This section presents the nonlinear in-plane response of 3D-printed concrete wall models incorporating L and T infill patterns. Finite element analyses were performed with two mesh densities (fine and medium) to assess mesh sensitivity and the robustness of the results. Fig. 8 shows the load–displacement curves obtained for each configuration, and numerical data are summarized in Table 3.

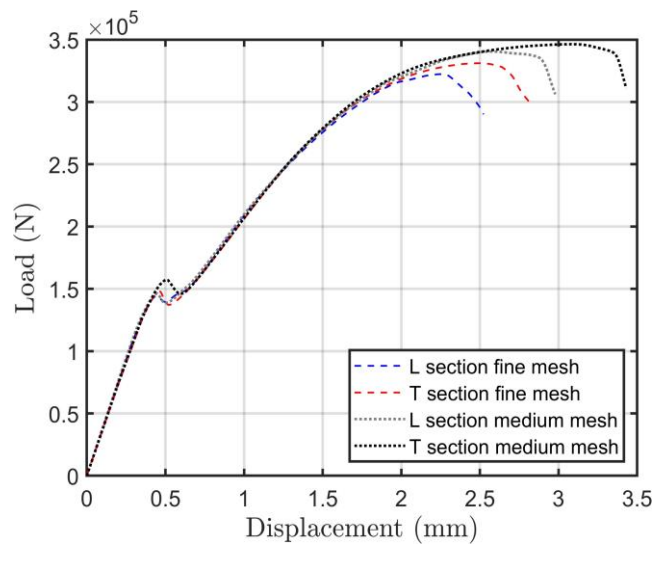


Fig. 8. Load–displacement curves of L and T-pattern wall models, showing higher peak load and ductility for the T-pattern across both mesh densities.

Table 3. Key performance metrics of 3D-printed wall models, including damage initiation and peak load values for each mesh and infill configuration.

Model	Displacement at damage initiation (mm)	Load (kN) at damage initiation	Displacement at peak load (mm)	Peak load (kN)	
L-fine	0.45	144.5	2.24	322.3	
T-fine	0.46	148.0	2.50	331.1	
L-medium	0.45	146.2	2.57	340.5	
T-medium	0.50	157.2	3.08	346.3	

Under monotonic lateral loading, all wall models exhibited a typical nonlinear load-displacement response characterized by an initial stiff elastic regime, a progressive reduction in stiffness with increasing displacement, and a final softening branch associated with material damage and loss of load-bearing capacity. Both L- and T-patterns displayed qualitatively similar behavior, with

discernible differences in ultimate strength, ductility, and crack evolution.

Notably, all wall models exhibited a local load peak at approximately 0.45–0.5 mm displacement, followed by a sharp drop. This first peak corresponds to the onset of localized cracking, predominantly at the outer wall regions adjacent to infill openings (Figs. 9 and 10).

After this initial damage, the models demonstrated a pronounced recovery in load-bearing capacity – evidenced by the renewed increase in the load-displacement curve – thanks to the redistribution of internal forces through undamaged regions and alternative load-bearing paths retained within the infill geometry. This is a direct result of the cellular infill layouts, where alternative load paths can be mobilized after local failure.

As loading continued, crack propagation and accumulated damage caused further stiffness degradation and post-peak softening, culminating in global failure when the primary load paths were fully fractured and the structure could no longer sustain increasing displacement.

Crack evolution differed significantly between patterns (Fig. 9 for L, Fig. 10 for T). Cracking in the L-pattern

typically initiates as short horizontal cracks at the wall base or at the interface between the infill and the outer wall. As loading progresses, three distinct diagonal damage bands emerge, each associated with a different panel region separated by the two vertical struts of the infill. The central diagonal band may eventually link to one of its neighbors, leaving only two main diagonal planes active. Because these bands do not combine into a single continuous failure plane, damage remains confined to separate regions. When stress tends to concentrate within the infill, local post-peak failure zones emerge – these trigger abrupt load drops and accelerate stiffness degradation. The overall failure mode is characterized by the formation of multiple, discontinuous diagonal cracks rather than a single dominant shear plane.

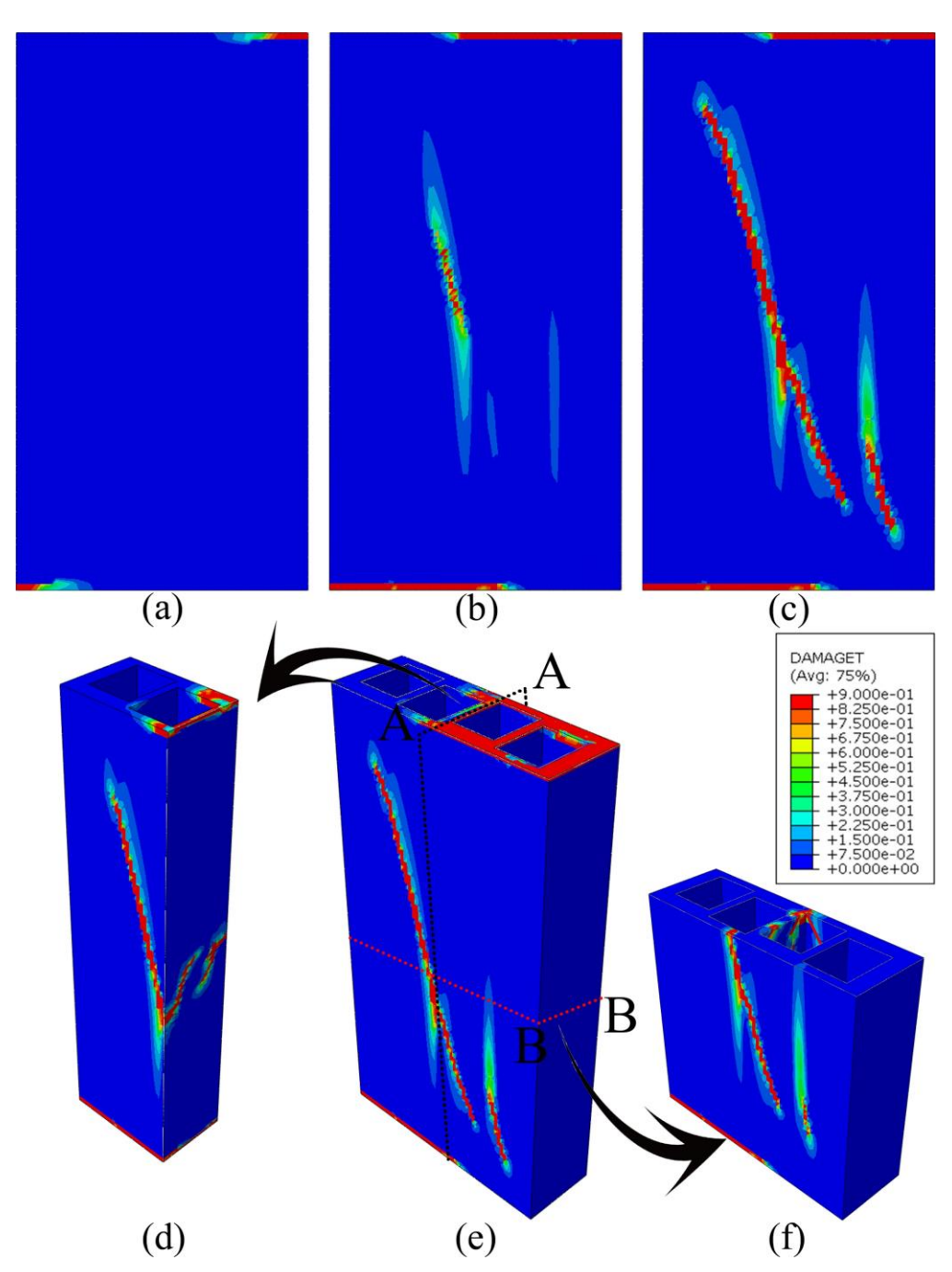


Fig. 9. L-pattern wall: (a–c) Front views of crack initiation and propagation; (d–f) 3D views showing discontinuous diagonal bands and local damage zones.

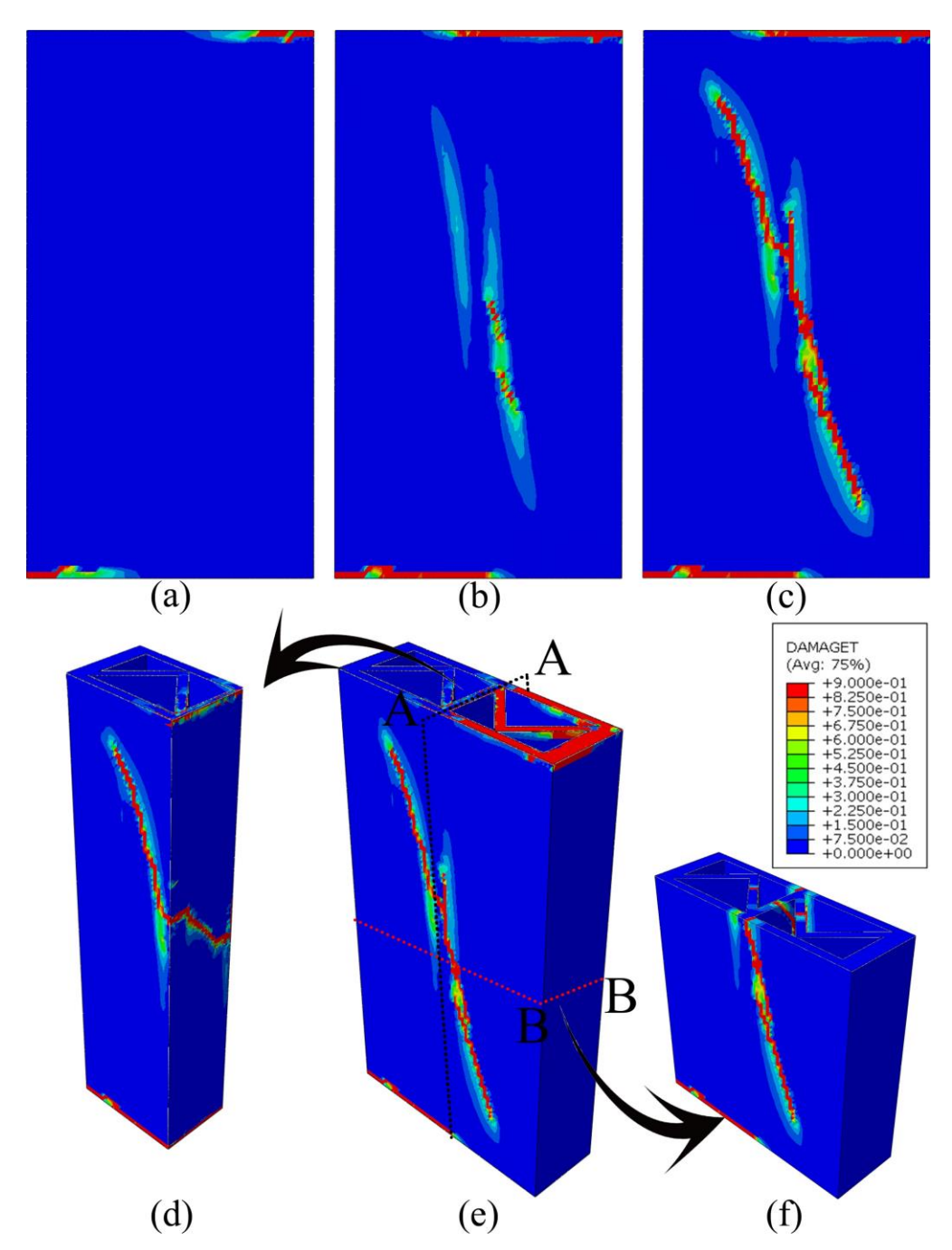


Fig. 10. T-pattern wall: (a–c) Front views of crack initiation and merging; (d–f) 3D views showing a continuous diagonal shear band linking infill and outer wall.

In the T-pattern, initial cracks develop as short horizontal fissures at the base and top of the wall. With further displacement, two separate diagonal cracks form, originating from the bottom corners and propagating upward and inward along the main diagonal load paths of the triangular infill. These cracks eventually merge into a single continuous diagonal damage band, often linking the infill and the outer wall.

For both mesh densities, the T-pattern walls achieved higher peak loads and exhibited modestly higher postpeak ductility compared to the L-pattern walls. Specifically, the T-pattern (medium mesh) reached a maximum load of $\sim\!346$ kN at a displacement of 3.08 mm, while the L-pattern (medium mesh) achieved a lower maximum of $\sim\!340$ kN at a displacement of 2.57 mm. For the fine mesh

models, the T-pattern again showed a higher peak load of \sim 331 kN, compared to the L-pattern at \sim 322 kN. This corresponds to a 1.7–2.7% higher peak load for T-patterns, depending on mesh size. First cracking consistently occurred at \sim 0.45–0.5 mm displacement, with initial crack loads ranging from 144.5 kN (L-fine) to 157.2 kN (T-medium).

Across all models, fine mesh solutions showed marginally earlier softening and slightly reduced post-peak load retention, due to their increased ability to localize damage and capture brittle post-peak behavior. These results confirm that the triangular infill, characterized by continuous diagonal load paths and efficient stress distribution, enhances both the load-bearing capacity and the energy dissipation after peak.

Mesh sensitivity was minimal; peak load deviation was less than 3%, with the fine mesh leading to marginally earlier softening and reduced post-peak load retention due to better localization of damage.

Although the formation of a single continuous diagonal crack in the T-pattern might intuitively seem to promote rapid structural failure, the simulation results demonstrate the opposite: the T-pattern achieves higher peak load and superior post-peak energy dissipation. This advantage is attributable to the geometric efficiency of having only one central strut, which creates two main load-bearing zones and focuses diagonal shear transfer through a direct, robust path. In contrast, the L-pattern's two interior struts divide the wall into three distinct regions, resulting in a broader area of damage and increased stress concentrations at multiple infill junctions. Consequently, the L-pattern exhibits more extensive diagonal cracking, greater localized damage. and slightly reduced capacity. This difference in internal force distribution explains why the T-pattern, despite exhibiting a continuous diagonal crack, outperforms the L-pattern in both strength and ductility. These findings align with the observed crack maps (Fig. 9 for L, Fig. 10 for T), which show multiple discontinuous diagonal cracks in the L-pattern but a more unified damage band in the T-pattern.

In conclusion, the internal geometry decisively influences both the strength and the nature of failure. While both patterns display mixed-mode (flexural and shear) cracking, the T-pattern demonstrates marginally better performance, which can inform infill strategy selection for digitally constructed walls.

4. Conclusions

This study investigated the nonlinear in-plane behavior of 3D-printed concrete walls with two distinct infill geometries-lattice (L) and triangular (T)-using finite element modeling informed by experimentally derived material properties. A printable cementitious mortar, characterized by high early-age strength and shape stability, was specifically developed, and its mechanical characteristics were incorporated into the simulations to ensure realistic representation of structural performance.

Key findings are as follows:

- Both infill types exhibited a distinct nonlinear response under monotonic lateral loading, characterized by an initial elastic regime, a localized load drop associated with crack initiation, a subsequent recovery phase due to internal force redistribution, and progressive post-peak softening as damage accumulated.
- T-pattern demonstrated superior performance, achieving 1.7–2.7% higher peak loads and improved ductility, attributed to its centralized diagonal force path and efficient stress redistribution, as opposed to the multiple discontinuous cracking bands observed in the L-pattern.
- Crack development in the T-walls followed a dominant diagonal shear band linking the outer wall and

- infill, while L-walls exhibited multiple damage zones with broader failure areas due to the division created by the two interior struts.
- Damage consistently initiated at ~0.45-0.50 mm displacement, highlighting critical stress concentrations near infill interfaces. Post-peak deterioration was governed by damage localization in both the outer wall and the infill regions.
- Incorporating fine mesh allowed improved resolution of damage localization and sharper post-peak degradation, though mesh sensitivity remained minimal for global response metrics.

However, interlayer interfaces were not explicitly modeled in the simulations. Although the developed mortar exhibited high cohesion and produced structurally robust printed elements, most printable mixtures may contain interfacial defects or exhibit weak layer bonding due to the nature of the layer-by-layer deposition process. These interfaces can significantly influence crack initiation and propagation. Therefore, future studies should incorporate interface effects (e.g. with cohesive contact definitions) or experimentally calibrated interface models to capture interface-driven damage mechanisms and better reflect the performance variability observed in real printed structures.

Moreover, while the effects of different infill geometries were assessed through two representative patterns, a more comprehensive understanding may be achieved by employing topology optimization algorithms that account for both in-plane and out-of-plane behavior. Such methods could reveal optimal hybrid infill forms tailored for multi-directional performance and material efficiency. In addition, experimental validation at full scale is needed to confirm the damage patterns observed numerically, particularly under cyclic or combined loadings representative of real-world conditions.

Acknowledgements

None declared.

Funding

The authors received no financial support for the research, authorship, and/or publication of this manuscript.

Conflict of Interest

The authors declared no potential conflicts of interest with respect to the research, authorship, and/or publication of this manuscript.

Author Contributions

All of the authors made substantial contributions to conception and design, or acquisition of data, or analysis and interpretation of data; were involved in drafting the manuscript or revising it critically for important intellectual content; and gave final approval of the version to be published.

Data Availability

The datasets created and/or analyzed during the current study are not publicly available, but are available from the corresponding author upon reasonable request.

REFERENCES

- Aghajani Delavar M, Chen H, Sideris P (2024). Analysis and design of 3D printed reinforced concrete walls under in-plane quasi-static loading. *Engineering Structures*, 303, 117535.
- AlZahrani AA, Alghamdi AA, Basalah AA (2022). Computational optimization of 3D-printed concrete walls for improved building thermal performance. *Buildings*, 12(12), 2267.
- Archdaily (2019). Dubai municipality to become the world's largest 3D-printed building. http://www.archdaily.com/930857/dubai-municipality-to-become-the-worlds-largest-3d-printed-building [accessed 27-08-2025].
- Architectsjournal (2014). Chinese firm prints ten houses in a day. http://www.architectsjournal.co.uk/news/chinese-firm-prints-ten-houses-in-a-day [accessed 27-08-2025].
- Bos F, Wolfs R, Ahmed Z, Salet T (2016). Additive manufacturing of concrete in construction: Potentials and challenges of 3D concrete printing. *Virtual and Physical Prototyping*, 11(3), 209-225.
- BS EN 12350-6 (2019). Testing fresh concrete Part 6: Density. British Standards Institution (BSI), London, UK.
- CEN ISO 17892-6 (2017). Geotechnical investigation and testing Laboratory testing of soil Part 6: Fall cone test. International Organization for Standardization (ISO), Geneva, Switzerland.
- Chamatete K, Yalçınkaya Ç (2024). Numerical evaluation on thermal performance of 3D printed concrete walls: The effects of lattice type, filament width and granular filling material. *Buildings*, 14(4), 926.
- Christ S, Schnabel M, Vorndran E, Groll J, Gbureck U (2015). Fiber reinforcement during 3D printing. *Materials Letters*, 139, 165-168.
- Delavar MA, Chen H, Sideris P (2022). Analytical and numerical investigation of out-of-plane behavior of 3D printed concrete walls. *Proceedings of the 12th National Conference on Earthquake Engineering*, Salt Lake City, Utah, USA.
- Dey D, Van VN, Xuan HN, Srinivas D, Panda B, Tran P (2023). Flexural performance of 3D printed concrete structure with lattice infills. *Developments in the Built Environment*, 16, 100297.
- Dziura P, Maroszek M, Góra M, Rudziewicz M, Pławecka K, Hebda M (2023). Influence of the in-fill pattern of the 3D printed building wall on its thermal insulation. *Materials*, 16(17), 5772.
- Hambach M, Rutzen M, Volkmer D (2019). Properties of 3D-printed fiber-reinforced portland cement paste. In: Sanjayan J, Nazari A, Nematollahi B, editors. 3D Concrete Printing Technology. Elsevier, Amsterdam, Netherlands, 73-113.
- Han X, Yan J, Liu M, Huo L, Li J (2022). Experimental study on largescale 3D printed concrete walls under axial compression. *Automa*tion in Construction, 133, 103993.
- Hanifa MF, Mendonça P, Figueiredo B, Mahdy D (2025). Experimental study on the thermal performance of 3D-printed earthen wall segment with optimized infill pattern. In: Cruz P, editor. *Structures and Architecture*. CRC Press, London, UK, 1692-1699.
- Hernández Vargas J, Sjölander A, Westerlind H, Silfwerbrand J (2024). Internal topology optimisation of 3D printed concrete structures: A method for enhanced performance and material efficiency. *Virtual and Physical Prototyping*, 19(1), e2346290.
- Hossain MA, Zhumabekova A, Paul SC, Kim JR (2020). A review of 3D printing in construction and its impact on the labor market. *Sustainability*, 12(20), 8492.
- Khanverdi M, Das S (2025). Performance of full-scale 3D-printed concrete walls: Effects of vertical reinforcements and window opening. Engineering Structures, 337, 120510.
- Kumar SS, Muthu N, Panda B (2025). Numerical investigation of structural behavior of 3D-printed concrete walls: From damage mechanics to cohesive zone approaches. *Progress in Additive Manufacturing*, In Press.
- Labonnote N, Rønnquist A, Manum B, Rüther P (2016). Additive construction: State-of-the-art, challenges and opportunities. *Automation in Construction*, 72, 347-366.
- Le TT, Austin SA, Lim S, Buswell RA, Law R, Gibb AGF, Thorpe T (2012). Hardened properties of high-performance printing concrete. *Cement and Concrete Research*, 42(3), 558-566.

- Lubliner J, Oliver J, Oller S, Oñate E (1989). A plastic-damage model for concrete. *International Journal of Solids and Structures*, 25, 299-326.
- Maskuriy R, Selamat A, Maresova P, Krejcar O, David OO (2019). Industry 4.0 for the construction industry: Review of management perspective. *Economies*, 7(3), 68.
- Mechtcherine V, Buswell R, Kloft H, Bos FP, Hack N, Wolfs R, Sanjayan J, Nematollahi B, Ivaniuk E, Neef T (2021). Integrating reinforcement in digital fabrication with concrete: A review and classification framework. *Cement and Concrete Composites*, 119, 103964.
- Mohamed RA, Mohamed AFA (2025). Exploring the environmental benefits of 3D printing technology in concrete construction: A review. *Progress in Additive Manufacturing*, 10(1), 279-289.
- Nan B, Qiao Y, Leng J, Bai Y (2025). Advancing structural reinforcement in 3D-printed concrete: Current methods, challenges, and innovations. *Materials*, 18(2), 252.
- Panda B, Unluer C, Tan MJ (2018). Investigation of the rheology and strength of geopolymer mixtures for extrusion-based 3D printing. *Cement and Concrete Composites*, 94, 307-314.
- Perrot A, Rangeard D, Pierre A (2016). Structural built-up of cement-based materials used for 3D-printing extrusion techniques. *Materials and Structures*, 49(4), 1213-1220.
- Rahman M, Rawat S, Yang R, Mahil A, Zhang YX (2024). A comprehensive review on fresh and rheological properties of 3D printable cementitious composites. *Journal of Building Engineering*, 91, 109719.
- Ramesh A, Rajeev P, Sanjayan J, Mechtcherine V (2024). In-process textile reinforcement method for 3D concrete printing and its structural performance. *Engineering Structures*, 314, 118337.
- Scheurer M, Dittel G, Gries T (2020). Potential for the integration of continuous fiber-based reinforcements in digital concrete production. In: Bos FP, Salet T, editors. *3D Printing in Concrete: Materials, Processes and Applications.* Springer, Berlin, Germany, 701-711.
- Suphunsaeng K, Prasittisopin L, Pethrung S, Pansuk W (2025). Fire performance evaluation of 3D-printed concrete walls: A combined fullscale and numerical modeling approach. *Journal of Building Engi*neering, 104, 112296.
- Tarhan Y, Tarhan İH, Şahin R (2024a). Comprehensive review of binder matrices in 3D printing construction: Rheological perspectives. *Buildings*, 15(1), 75.
- Tarhan Y, Tarhan İH, Jacquet Y, Perrot A (2024b). Mechanical behaviour of 3D printed and textile-reinforced eco-friendly composites. *Journal of Sustainable Cement-Based Materials*, 14(3), 477–495.
- Tarhan İH, Tarhan Y (2025). Cultural heritage conservation in digital era: A review of digital twin and 3D printing applications. *Uludağ University Journal of the Faculty of Engineering*, In Press.
- Tarhan Y, Tarhan İH, Perrot A (2025a). Improving bond performance of 3D-printable earth-based mortar reinforced with jute fibers. Challenge Journal of Structural Mechanics, 11(2), 99-105.
- Tarhan Y, Tarhan İH, Perrot A (2025b). Flexural performance of glass fibre textile reinforced 3D printed concrete. Proceedings of the 4th International Civil Engineering & Architecture Conference, Trabzon, Türkiye, 1509-1515.
- Tarhan İH (2025a). Nonlinear in-plane behavior of masonry walls strengthened with optimally distributed fiber reinforced polymer. *Engineering Failure Analysis*, 182(Part A), 110035.
- Tarhan İH (2025b). Stepwise FRP strengthening of historical masonry minarets: Nonlinear seismic assessment based on a minaret collapsed during the 2023 Kahramanmaraş earthquakes. *Engineering Failure Analysis*. 180. 109933.
- TS EN 12390-3 (2019). Testing hardened concrete Part 3: Compressive strength of test specimens. Turkish Standards Institute, Ankara, Türkiye.
- TS EN 12390-5 (2019). Testing hardened concrete Part 5: Flexural strength of test specimens. Turkish Standards Institute, Ankara, Türkiye.
- Wangler T, Lloret E, Reiter L, Hack N, Gramazio F, Kohler M, Bernhard M, Dillenburger B, Buchli J, Roussel N, Flatt R (2016). Digital concrete: Opportunities and challenges. RILEM Technical Letters, 1, 67-75.
- Warsi SBF, Panda B, Biswas P (2025a). Design of earthquake-resistant 3D printed concrete wall based on ACI 318–19: Analytical investigation and numerical modelling. *Structures*, 78, 109371.

- Warsi SBF, Panda B, Biswas P (2025b). Structural analysis of 3D-printed concrete walls under quasi-static cyclic loading using composite micro-model. *Progress in Additive Manufacturing*, 10(8), 4901-4921.
- Winsun3d (2015). 2015 global highest 3D printing building. http://www.winsun3d.com/En/Product/pro_inner_5/id/102 [accessed 27-08-2025].
- Sümer Y, Aktaş M (2015). Defining parameters for concrete damage plasticity model. *Challenge Journal of Structural Mechanics*, 1(3), 149-155.
- Zafar MS, Javadnejad F, Hojati M (2025). Optimizing rheological properties of 3D printed cementitious materials via ensemble machine learning. *Additive Manufacturing*, 109, 104889.
- Zhang B, Tao Y, Zhang Y, Shields Y, De Corte W, Wan-Wendner R (2025a). Mechanical properties of 3D printed concrete with 2D infill patterns including print path crossings. *Construction and Building Materials*, 483, 141764.
- Zhang B, Zhang Y, Ye Y, Hao L, Cui W, Yang H, Tao Y (2025b). Influence of contacts in 2D infill patterns on mechanical properties of 3D printed concrete structures. *Materials Letters*, 388, 138307.
- Zoey (2018). WinSun print into the future. https://digital.hbs.edu/platform-rctom/submission/winsun-print-into-the-future/ [accessed 27-08-2025].